# SURFACE SCIENCE EXPERIMENTS INVOLVING THE ATOMIC FORCE MICROSCOPE

by

SEAN P. MCBRIDE

B.S., Bloomsburg University, Bloomsburg, Pennsylvania, 2003
M.S., Miami University, Oxford, Ohio, 2005

AN ABSTRACT OF A DISSERTATION

submitted in partial fulfillment of the requirements for the degree

DOCTOR OF PHILOSOPHY

Department of Physics
College of Arts and Sciences

KANSAS STATE UNIVERSITY
Manhattan, Kansas

2012

# Abstract

Three diverse first author surfaces science experiments conducted by Sean P. McBride[1-3] will be discussed in detail and supplemented by secondary co-author projects by Sean P. McBride,[4-7] all of which rely heavily on the use of an atomic force microscope (AFM).

First, the slip length parameter, *b* of liquids is investigated using colloidal probe AFM. The slip length describes how easily a fluid flows over an interface. The slip length, with its exact origin unknown and dependencies not overwhelming decided upon by the scientific community, remains a controversial topic. Colloidal probe AFM uses a spherical probe attached to a standard AFM imaging tip driven through a liquid. With the force on this colloidal AFM probe known, and using the simplest homologous series of test liquids, many of the suspected causes and dependencies of the slip length demonstrated in the literature can be suppressed or eliminated. This leaves the measurable trends in the slip length attributed only to the systematically varying physical properties of the different liquids.

When conducting these experiments, it was realized that the spring constant, *k,* of the system depends upon the cantilever geometry of the experiment and therefore should be measured in-situ. This means that the *k* calibration needs to be performed in the same viscous liquid in which the slip experiments are performed. Current in-situ calibrations in viscous fluids are very limited, thus a new in-situ *k* calibration method was developed for use in viscous fluids. This new method is based upon the residuals, namely, the difference between experimental force-distance data and Vinogradova slip theory.

Next, the AFM's ability to acquire accurate sub nanometer height profiles of structures on interfaces was used to develop a novel experimental technique to measure the line tension parameter, $\tau$, of isolated nanoparticles at the three phase interface in a solid-liquid-vapor system. The $\tau$ parameter is a result of excess energy caused by the imbalance of the complex intermolecular forces experienced at the three phase contact line. Many differences in the sign and magnitude of the $\tau$ parameter exist in the current literature, resulting in $\tau$ being a controversial topic.

# SURFACE SCIENCE EXPERIMENTS INVOLVING THE ATOMIC FORCE MICROSCOPE

by

SEAN P. MCBRIDE

B.S., Bloomsburg University, Bloomsburg, Pennsylvania, 2003
M.S., Miami University, Oxford, Ohio, 2005

A DISSERTATION

submitted in partial fulfillment of the requirements for the degree

DOCTOR OF PHILOSOPHY

Department of Physics
College of Arts and Sciences

KANSAS STATE UNIVERSITY
Manhattan, Kansas

2012

Approved by:

Major Professor
Dr. Bruce M. Law

# Copyright

# Abstract

Three diverse first author surfaces science experiments conducted by Sean P. McBride[1-3] will be discussed in detail and supplemented by secondary co-author projects by Sean P. McBride,[4-7] all of which rely heavily on the use of an atomic force microscope (AFM).

First, the slip length parameter, *b* of liquids is investigated using colloidal probe AFM. The slip length describes how easily a fluid flows over an interface. The slip length, with its exact origin unknown and dependencies not overwhelming decided upon by the scientific community, remains a controversial topic. Colloidal probe AFM uses a spherical probe attached to a standard AFM imaging tip driven through a liquid. With the force on this colloidal AFM probe known, and using the simplest homologous series of test liquids, many of the suspected causes and dependencies of the slip length demonstrated in the literature can be suppressed or eliminated. This leaves the measurable trends in the slip length attributed only to the systematically varying physical properties of the different liquids.

When conducting these experiments, it was realized that the spring constant, *k,* of the system depends upon the cantilever geometry of the experiment and therefore should be measured in-situ. This means that the *k* calibration needs to be performed in the same viscous liquid in which the slip experiments are performed. Current in-situ calibrations in viscous fluids are very limited, thus a new in-situ *k* calibration method was developed for use in viscous fluids. This new method is based upon the residuals, namely, the difference between experimental force-distance data and Vinogradova slip theory.

Next, the AFM's ability to acquire accurate sub nanometer height profiles of structures on interfaces was used to develop a novel experimental technique to measure the line tension parameter, $\tau$, of isolated nanoparticles at the three phase interface in a solid-liquid-vapor system. The $\tau$ parameter is a result of excess energy caused by the imbalance of the complex intermolecular forces experienced at the three phase contact line. Many differences in the sign and magnitude of the $\tau$ parameter exist in the current literature, resulting in $\tau$ being a controversial topic.

# Table of Contents

# List of Figures

# List of Tables

# Acknowledgements

I would like to thank Dr. Bruce M. Law, my PhD advisor, for many beneficial discussions revolving around the surface science experiments presented throughout this dissertation. The freedom you have given me with the equipment in the laboratory and the freedom to explore potential solutions to the problems presented in this dissertation has undoubtedly contributed to my confidence as a scientist and prepared me greatly to take on any research project in the future.

I also thank the staff of the Physics Department, specifically Peggy Matthews, Jane Peterson, Lindsay J. Thompson, Deanna Selby, Lisa McNeil, Aubrey Carrara, and Cassie Hall for everything you have done. Your efforts to make sure I follow the correct academic policies and procedures, your efforts in maintaining my academic graduate/teaching assistantship, and for your efforts in keeping all financial affairs associated with my research in order have all been greatly appreciated. I am also grateful for the assistance from machinists Russ Reynolds and Bryan Merritt not only for the fabrication of research components, but for also ensuring that I always had access to the correct tools when machining research components personally. Additionally, thanks to Peter Nelson and Bob Krause for all the equipment and small components I have borrowed or used over the years to complete this research.

I would also like to thank all of my committee members along with Dr. Christian Madsen, Dr. Dyan L. Jones, Adrian Madsen, Varun 'Mac' Makhija, Mohammad Zohrabi, Nick Roseveare, and John Hirt for reviewing much of this dissertation and providing useful comments and suggestions, these have all been greatly appreciated. I also thank Betsy Edwards, ETDR lead consultant at Kansas State University, for reviewing the format of this document.

I owe a special thanks to my parents, Duy and Sheila, and my sister, Alison for their continued words of encouragement, love, and support throughout all my academic studies. To Christian and Adrian Madsen, Varun 'Mac' Makhija, Mohammad Zohrabi, and all my friends and family members, I am forever in your debt. Thank you for being there to help me cope with one of the most tragic losses in my personal life that has occurred during the writing of this dissertation. Your advice, words of encouragement, and support have all been beyond measure.

# Chapter 1 - Introduction to Surface Science Experiments

## 1.1 Overview and Organization of Dissertation

Chapter 1 provides an overview of the research related to this dissertation including, a fundamental conceptual introduction to each focused project with applications and uses of the conducted research, motivation for each project, and impact of the conducted experimental work on the scientific community. Chapter 2 discusses in detail the principles of the characterization techniques involving atomic force microscopy (AFM) imaging, AFM force measurements, contact angle measurements, and contact angle hysteresis measurements. Chapters 3-5 describe in detail the works involving the viscosity dependent slip length, the residuals spring constant calibration method, and the line tension parameter of singular isolated spherical nanoparticles at a liquid-air interface, respectively. Chapter 6 summarizes the work performed in this dissertation. The complete derivation of the Vinogradova theory used in the majority of this work is found in Appendix A. The step-by-step technical details of using the Igor Pro programs to determine accurate colloidal probe AFM force and the slip length measurements are described in Appendix B. This dissertation is expected to be read cover to cover by a future graduate student attempting to continue this work or similar surface science work using the AFM; technical sections not required by the general reader may be skipped as indicated in Fig. 1.1 without losing continuity of the dissertation.

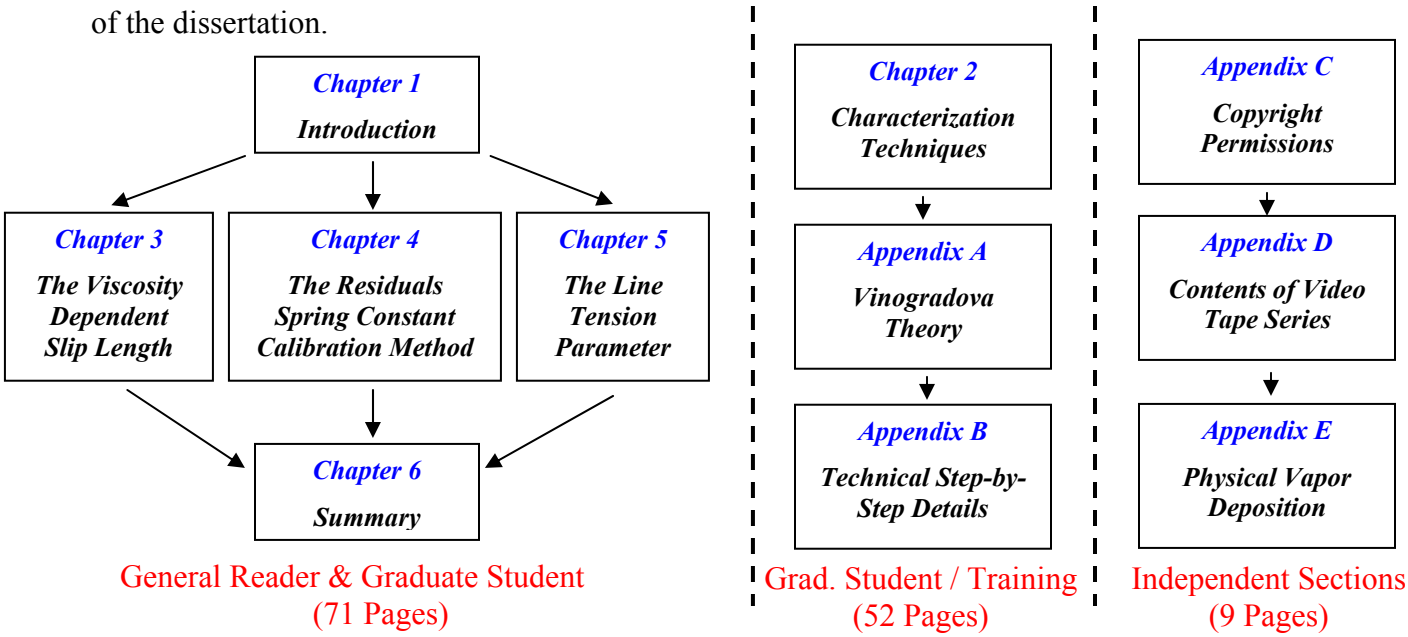


**Fig. 1.1: Dissertation reading schemes for various audiences.**

## 1.2 Introduction to the Slip Length Parameter and Applications

In the past two decades the world market for microfluidic technologies and applications of such devices has soared.[8-11] This accelerated interest in micro and nano-fluidic systems has also led to an extensive array of newly engineered surfaces.[12,13] As shown in Fig. 1.2, microfluidic devices are designed to drive small amounts of fluid through microscopic or nanoscopic geometries where numerous complex reactions can occur within a small volume.[14,15] Though these devices are only in their infancy, they have been used extensively in molecular and chemical biology;[16-20] with research efforts focused toward the promising application of point-of-care clinical diagnostics of human physiological fluids.[21,22] These point-of-care microfluidic devices are a potential solution to the global health diagnostics of civilizations in remote environments where access to health care facilities and supporting clinical laboratory infrastructure are non-existent or extremely limited.[23]

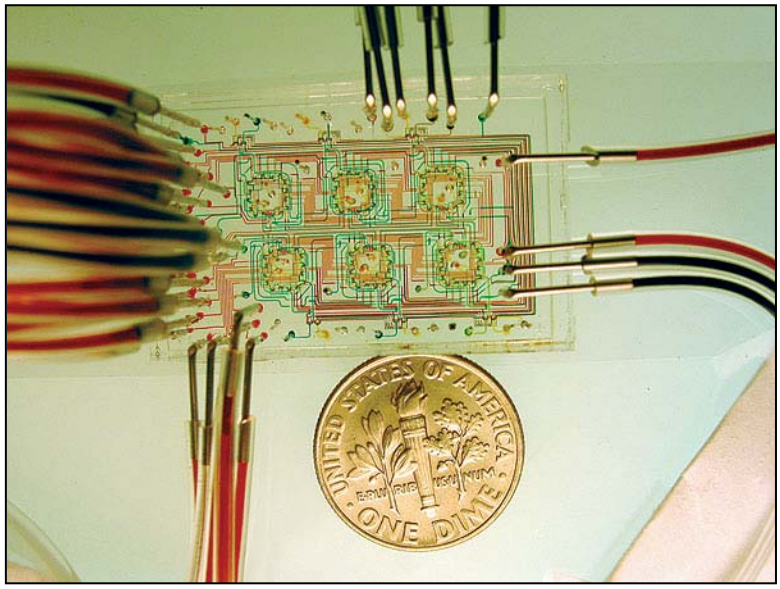


**Fig. 1.2: Microfluidic bioreactor developed by Balagddé *et al.* [15] (Fig. 1A from ref. [[15]]) This microfluidic device has six independent 16-nanoliter reactors allowing fluids to be monitored in situ by optical microscopy to provide automated, real-time, noninvasive measurement of cell density and morphology with single-cell resolution. (Image available at www.nature.com/.../fig_tab/nature05058_F1.html).**

A parameter present in these microfluidic devices, at the engineered liquid-surface interfaces, is referred to as the *slip length* parameter, *b*.[24-26] This parameter describes how easily a fluid flows over a solid surface and is characterized by the extrapolated distance into the solid

surface where the fluid velocity would theoretically be zero as shown in Fig. 1.3. A different way to think of this parameter is by imagining a rock in the middle of a flowing stream of water; if the layer of water directly above the surface of the rock sticks to the rock, then there is no slip length present, but if the water directly at the rock's surface is flowing with some velocity over the rock, then there is a slip length present. As microfluidic devices decrease in size, the slip length parameter will be an essential quantity for improving and describing the efficiency of such devices; a larger slip length would mean that less energy would be needed to drive the liquid through these systems. Understanding the source of the slip length and its dependencies on experimental variables in these devices will also allow for accurate calculations of fluid flow rate and velocity profiles needed to improved and vary their design characteristics.

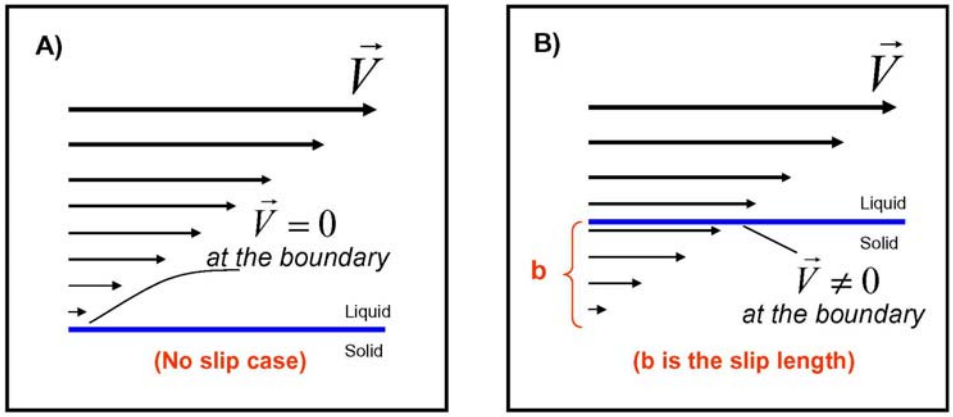


**Fig. 1.3: A) Case where the slip length at the solid-liquid interface is zero. B) Standard definition of the slip length parameter at the solid-liquid interface where the slip length is non-zero.**

In parallel with the increase in the research and development in the microfludics industry, many theories and experiments involving the study of a fluid flow over a solid substrate have been developed and performed.[27-32] These studies show that the slip length at a solid-liquid interface can have a wide range of values, from several nanometers to several microns, depending upon the system studied. Based upon the results in the literature, the slip length also depends on how well the substrates are prepared and the experimental techniques employed to measure it. Experiments demonstrate that the uncertainty for slip length can range from 5-100 nm depending upon the method used. Such large ranges in the accuracy and magnitude of slip length results have led to a vast amount of controversy in the field. Focused studies illustrate that

slip length may be governed by the wettability *(θ)* of the liquid for the solid,[33-42] the bulk viscosity *(η)* of the liquid (or liquid structuring at the surface leading to the presence of a lower viscosity liquid layer adjacent to the solid surface),[36-38,43-47] the surface roughness of the solid surfaces *(rms)*,[36,38-40,48-51] the shear rate *(γ)*,[33,36-38,52-57] the presence of a gaseous layer or nanobubbles at hydrophobic surfaces,[45,58-63] the liquid molecular shape,[55,64] and/or dipole moment of the liquid.[65] Fig. 1.4 shows schematic diagrams of the most notable dependencies of the slip length observed by leading scientists.

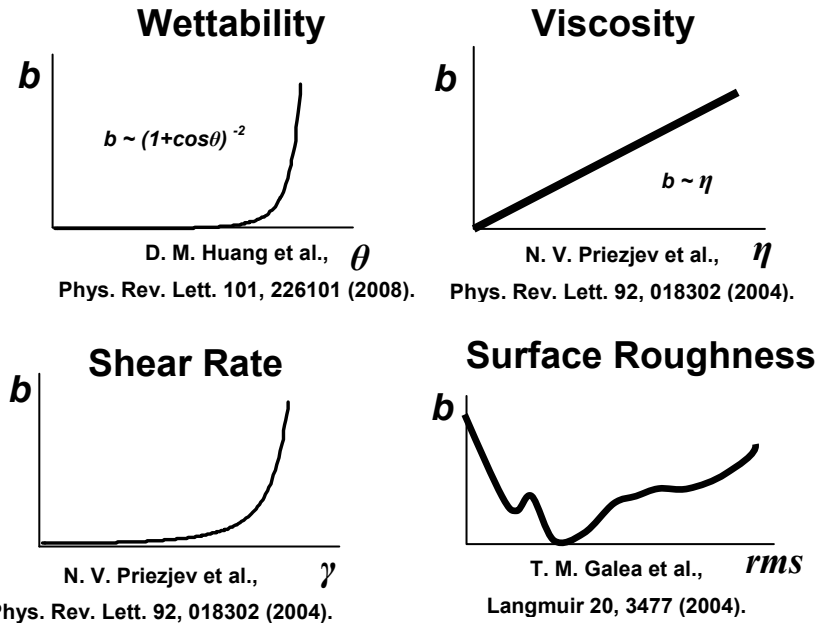


**Fig. 1.4: Schematics of general dependencies of slip length found from specific research groups. (top left) – slip length as a function of contact angle, (top right) – slip length as a function of viscosity, (bottom left) – slip length as a function of shear rate, and (bottom right) – slip length as a function of surface roughness.**

Recent research efforts by the scientific community have evolved from studying the slip length on normal planer hydrophilic/hydrophobic surfaces to the more recently developed super-hydrophobic and patterned interfaces.[66,67]

## 1.3 Motivation for Slip Length Experiments

The motivation for the research conducted in Chapter 3 was to determine which factors in Sec. 1.2 are responsible for the slip length behavior and what trends are observable when the experimental parameters are systematically changed using the simplest experimental system. An atomic force microscope (AFM) is an ideal instrument for this type of study. When used in

conjunction with a large colloidal probe, the AFM has the sensitivity to easily measure nano-Newton hydrodynamic forces. Colloidal probe AFM consists of attaching a micron sized glass sphere to a standard AFM imaging cantilever as shown in Fig 1.5.

**Fig. 1.5: A colloidal probe made from a standard Veeco NPS series imaging cantilever and a 55 µm borosilicate sphere from Mo-SCI.**

This colloidal probe can then be driven towards or away from a solid substrate, which is typically atomically smooth silicon, with a liquid placed between the colloidal probe and solid substrate as shown in Fig 1.6. If the sphere is sufficiently large, the drag force of the cantilever as it moves through the liquid can be neglected (as proven and discussed in detail in Chapter 4); this results in the AFM being able to measure the experimental force on the sphere approaching the solid surface via Hooke's Law, $F_h = k \cdot x$ (deflection of the colloidal probe, $x$ multiplied by the colloidal probe spring constant, $k$). For the cases studied, comparison between this experimental force to the theoretical force of a sphere approaching a planar surface in a liquid including a slip length,[68] using a non linear least square fit, provides excellent agreement for a non-zero slip length (the slip length is the only adjustable parameter in the fit). The AFM has the added benefit that (1) the test liquids can be easily changed between experiments, (2) the cantilevers and substrates can be efficiently cleaned between experiments, and (3) the test area, essential to keep clean, is on the order of several of microns for the AFM, as compared to the several centimeter diameter crossed cylinders of a standard surface forces apparatus (SFA).[69] The SFA theoretically has much greater hydrodynamic force sensitivity over the AFM due to the larger radius of the crossed cylinders ($F_h$ is directly proportional to $R^2$; see Chapter 3, 4, and Appendix B), but despite the greater force sensitivity, the SFA and the AFM provide the same order of magnitude of slip results for similar studied systems.[27] A detailed discussion on the procedure for acquiring hydrodynamic force measurements and colloidal probe AFM calibration is discussed in detail in Chapters 4 with the step-by-step details given in Appendix B.

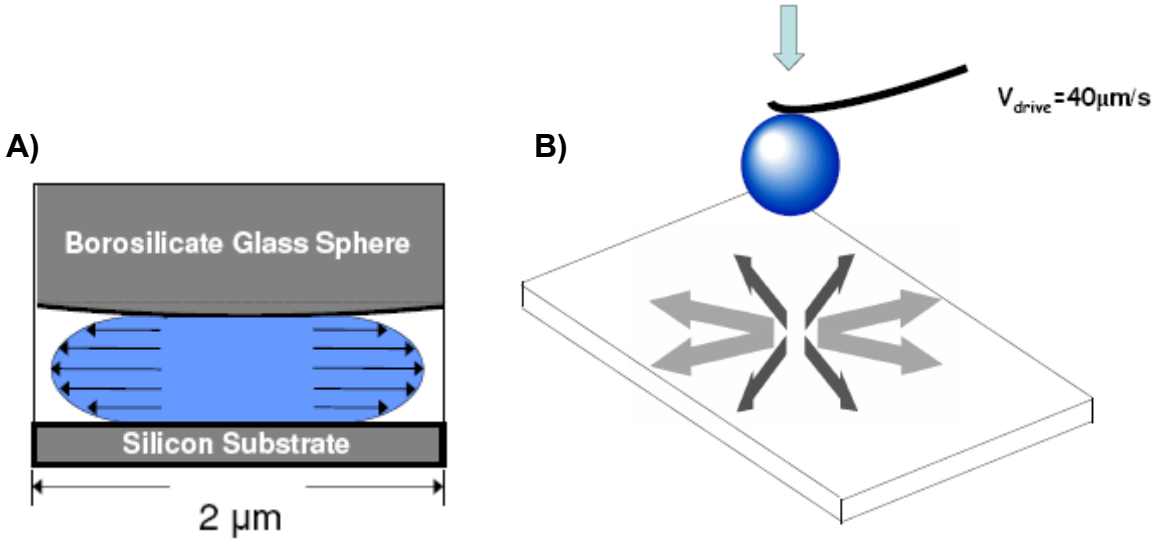


**Fig. 1.6: A) Fluid flow profile of a liquid between the colloidal probe and silicon substrate as the sphere approaches the silicon substrate. B) 3D schematic of fluid flow between the colloidal probe and substrate.**

With the simplest instrument for measurement of the slip length chosen, the next concern is what is the simplest liquid to test? As required by the theoretical force of a sphere with a constant slip length approaching a planar surface in a liquid (derived in Appendix A), the fluid tested must be Newtonian, meaning that it is incompressible. With this in mind, the n-alkanes and n-alcohols were chosen. A homologous series of each was chosen so that the characteristics of the test fluid could be systematically changed while still using a pure test liquid. In the homologous series, the additional carbon chain to each molecule causes the liquid vapor surface tension to systematically increase; similarly, the viscosity and the contact angle the drop makes with a substrate systematically increases. The n-alkanes and n-alcohols are all simple cigar shaped molecules, each having a small dipole moment (n-alcohols) or zero dipole moment (n-alkanes). The choice of these liquids eliminates the polar dependency of the liquid slip length since the dipole moment is either non-existent or roughly constant for each series. The molecular shape dependence of slip length is also eliminated considering all n-alkanes and n-alcohols are cigar shaped molecules as shown in Fig. 1.7. In most experiments found in the literature, the properties of wettability and viscosity of the test liquid are changed by adding additives or impurities to a pure liquid. This creates a solution that may lead to complicated preferential adsorption effects at the interface which in turn could influence the slip behavior.

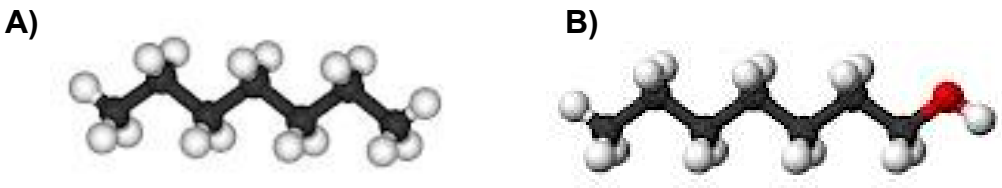


**Fig. 1.7 (A) Heptane molecule (image available at http://it.wikipedia.org/wiki/File:Heptane-3D-balls.png). (B) Heptanol molecule (image available at: http://bg.wikipedia.org/wiki/%D0%A4%D0%B0%D0%B9%D0%BB:1-Heptanol-3D-balls.png). The white spheres represent hydrogen atoms, the black spheres represent carbon atoms, and the red sphere represents oxygen.**

Other suggested factors such as shear rate and surface roughness can be eliminated by maintaining the same experimental set-up conditions and surfaces for each liquid. Any experimental set-up effects such as surface roughness and substrate preparation are kept constant since the surfaces remain the same for each different test liquid. If the same geometry and drive velocity of approaching sphere are the same, similar magnitude shear rates will occur. Also, environmental test conditions (i.e. humidity, type of atmosphere, etc.) for each experiment are maintained through the use of a custom designed and built environmental chamber surrounding the AFM head as shown in Fig. 1.8 (see Appendix B for operational details). This results in any detectable change in slip length being due to only the physical properties of the liquid. Therefore, if all other parameters remain unchanged, the effects of slip length on wettability (i.e. the contact angle) and viscosity can be tested by simply exchanging the pure test liquid between the colloidal probe and substrate in hydrodynamic drainage experiments.

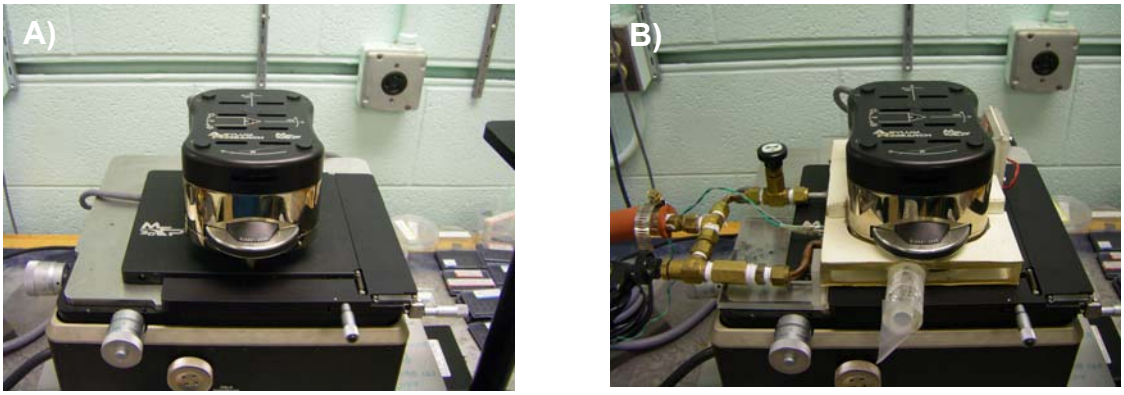


**Fig. 1.8: A) Standard Asylum Research MFP 3D AFM set-up. B) Custom designed and built environmental chamber surrounding the AFM head. Chamber used to maintain constant environmental conditions such as gas environment and humidity content.**

As discussed in detail in Chapter 4 and Appendix B, by using a slow approach of the colloidal probe to the substrate, no indication of nano-air bubbles forming a gaseous layer at the interface was ever detected in any experiment. If present, these nano-bubbles would easily be observed by unusual cantilever deflection measurements as the probe approaches the substrate. The experiments conducted in Chapter 3 are performed with colloidal probes of varying spring constant and all results indicate that the slip length is a function of viscosity and is independent of the spring constant of the colloidal probe used.

## 1.4 Impact of Experimental Slip Length Results on the Scientific Community

Chapter 3 presents the basic experimental procedure needed to obtain accurate and reliable slip length measurements using colloidal probe AFM. The work in Chapter 3 was initially of purely experimental interest, with theories predicting that the slip length should be dependent upon the viscosity of the test liquid not highly emphasized. Recent work by Ducker *et al.*,[70] the 'founding father' of colloidal probe AFM,[71] cites that the work presented in Chapter 3 has a positive correlation with the theoretical predictions of Ruckenstein and Rajora[72] for a viscosity dependent slip length. The significance of the slip lengths presented in Chapter 3, which measure less than 20nm, are also commented on in the recent work of Honig and Ducker.[73] Reference is made to the models and methods used in Chapter 3 in each part of a recent two part publication entitled *Reliable Measurements of Interfacial Slip by Colloid Probe Atomic Force Microscop*y by Zhu, Attard, and Neto.[74,75]

Recent simulation work by Asproulis and Drikakis[76] also examine the problem of hydrodynamic boundary slip at a solid interface. In their work they state that the parameter responsible for generating the slip at interfaces is still not explicitly known by the scientific community, but the work presented in Chapter 3 is cited to be among the main contributing factors. The results presented in Chapter 3 have also been cited in recent simulation work by Priezjev[77] as one of the main factors affecting slippage at the liquid-solid interface.

## 1.5 Introduction to AFM Spring Constants and Applications

The hydrodynamic drainage experiments conducted in Chapter 3 relied heavily on the deflection of the colloidal probe measured by the AFM. When using either colloidal or non-colloidal probes the force in AFM measurements is always defined as $F = k \cdot x$, where the vertical deflection of the colloidal/non-colloidal probe, $x$, is multiplied by the colloidal/non-colloidal

probe spring constant, *k;* therefore, in any force measurement with an AFM, the resulting accuracy of the measurement is only as accurate as the accuracy of the determined spring constant. This concern is documented in the earliest AFM measurements,[78,79] assessing that *k* is the primary limiting factor in determining the accuracy in magnitude of the force measurement. Soon after the development of the AFM, several popular *k* determination methods for V-shaped and beam cantilevers known as the Cleveland method,[80] thermal noise method,[81] and Sader methods[82-85] were developed. In Chapter 4, the chronological development and details of each of these methods, along with additional methods for other types of cantilevers, are given in Sec. 4.2.

## 1.6 Motivation to Determine a New AFM Spring Constant Calibration Specifically for Use with Colloidal Probes

While conducting the hydrodynamic drainage experiments presented in Chapter 3 it became evident that the AFM spring constant was dependent upon the positioning of the colloidal probe on the end of the standard imaging cantilever. These noticeable effects were later summarized in a publication by Edwards *et al*.[86] Their work emphasized that for colloidal probes, the spring constant calibration should be done in-situ, or in other words, in the same experimental setup and environment as the desired experiment to correctly take into account any tilt and torques present due to the addition of the colloidal probe in the experimental geometry. Simultaneously, their work confirmed the experimental observations seen when conducting the work in Chapter 3. Experimentally, conducting the spring constant calibration in the same set-up as the desired experiment is not difficult; however, conducting the spring constant calibration for a colloidal probe immersed in a viscous test liquid proves to be futile when using other existing calibration methods. This is because most spring constant calibration methods to some degree rely on the resonant frequency of the cantilever. They require that the quality factor, $Q$ of the resonant frequency peak be well defined such that $Q >> 1$. For large colloidal probes in viscous liquids, the system is drastically damped by the surrounding fluid $(Q << 1)$ and the resonance frequency peak becomes ill defined, thus the need for a new calibration technique arises.

The new calibration technique outlined in Chapter 4 is based on examining the residuals, namely, the difference between experimental data ($F = k \cdot x$) and the theoretical drainage force (including the slip length parameter) as a function of separation between the colloidal probe and the substrate, $h$. Perfect agreement between experimental data and the theoretical drainage force

would be indicated by residuals which are symmetrically displaced about zero. Therefore, in this procedure, an improved spring constant is determined by changing $k$ in increments of 0.01 N/m, between upper and lower experimental bounds, until the lowest sum of the squares of the residuals is found; this effective value for $k$ represents the optimal $k$ value for the system, possessing minimal systematic deviations in the residuals.

Two different spring constant methods were employed to provide the experimental upper and lower bounds for the adjustment of $k$. The upper experimental bound on $k$ was determined using the method developed specifically for colloidal probes by Craig and Neto.[87] This method correctly takes into account the system geometry, tilts, and torques described by Edwards *et al.*[86] The method however was developed for a system where the no slip boundary condition ($b = 0$) is valid; therefore, it is only intended as an approximation to the upper experimental bound on $k$. Our method has the added benefit that it only relies on the well known parameters of viscosity of the test liquid, radius of the colloidal probe, and velocity of the probe (Sec. 4.4). The lower experimental bound for $k$ was determined using the thermal noise method.[81] Since this method requires a well defined resonant frequency peak with ($Q >> 1$), this calibration was done in the desired experimental configuration, but with no test liquid inserted between the colloidal probe and substrate. With practice, this method becomes a quick and simple process to determine $k$ using the default thermal noise model via the user interface provided with the Asylum Research 3D MFP AFM software (see manual[88] and Appendix B).

To test the validity of this improved spring constant method, slip length tests were run in low viscosity liquids with the spring constant $k$ fixed from the improved residuals calibration performed in the most viscous test liquid. The residuals for these low viscosity liquids again exhibited no systematic deviations using the fixed $k$ from the improved residuals calibration, indicating that this value of $k$ was indeed the correct value.

## 1.7 Impact of Residual Spring Constant Calibration Results

Chapter 4 presents the basic experimental procedure needed to obtain accurate and reliable spring constant determinations and slip length measurements using colloidal probe AFM. The residuals spring constant calibration method developed in Chapter 4 is quite general and can be applied to any colloidal probe configuration as long as the forces on the colloidal probe and cantilever are known. This calibration method will be of immediate interest to all colloidal probe

AFM users, specifically those using spherical colloidal probes in hydrodynamic drainage experiments where the drag force on the spherical probe has been well established.[68,89] Ducker *et al.*[70] duplicated the improved residuals calibration method in their recent publication and found the method to be extremely accurate for determination of $k$. They also found similar size deviations between the thermal and residuals calibration methods for $k$. The work presented in Chapter 4 is also referenced in *Reliable Measurements of Interfacial Slip by Colloid Probe Atomic Force Microscop*y by Zhu, Attard, and Neto[74] and in *Lubrication Forces in Polydimethylsiloxane (PDMS) Melts* by Chatchaidech.[90] In addition, the slip lengths obtained using the residual spring constant calibration method in Chapter 4 further confirm the experimental results in Chapter 3, specifically the positive correlation between the slip length and viscosity. In Chapter 3, $k$ was determined by the method developed by Craig and Neto.[87] The work in Chapter 4 implies that these earlier slip length values in Chapter 3 are potentially lower than the reported values.

## 1.8 Introduction to the Line Tension Parameter and Applications

In Chapters 3 and 4 the AFM is used to measure forces in hydrodynamic drainage experiments. In Chapter 5, the capability of the AFM to record precise images on the nanometer length scale is used to indirectly measure the line tension parameter, $\tau$.[91-95] The line tension parameter arises where three different type of phases meet. For example, when a liquid droplet rests on a solid surface there are three phases present in the system. The *solid phase*, which the liquid drop rests on, the *liquid phase* of the droplet itself, and the air or immiscible fluid that surrounds the droplet known as the *vapor/fluid phase*. These three phases are also present when a solid particle is situated at a liquid-vapor interface. Here, the *solid phase* is the particle itself, the *liquid phase* is the liquid that the particle is in equilibrium with, and the air or immiscible fluid that surrounds the particle is still called the *vapor/fluid phase.* In each one of these cases there is a three phase solid-liquid-vapor contact line (TPCL) where all three phases meet as shown in Fig. 1.9. The concept of line tension, $\tau$ was first introduced by Gibbs[96] to explain the excess free energy caused by the imbalance of the complex intermolecular forces experienced at the three phase contact line. Since then, $\tau$ has become established as a fundamental thermodynamic property of surface science.[97,98]

An example of this three phase solid-liquid-vapor contact line and its associated line tension, $\tau$ in the macroscopic world can be derived from most reader's childhood memories. Remember when you played with soapy water either helping your mom or dad wash the family car; or just for the fun of making soap bubbles when you were younger? If so, do you remember poking your finger through a large bubble and not having it pop? This hypothetical scenario, if experienced, is a macroscopic example of the line tension parameter and the three phase solid-liquid-vapor contact line (TPCL). The bubble is exerting a small force that is closing in around your finger from all sides, which is an example of a positive line tension around your finger. Around this line where the force acts, your finger is in contact with the soapy water as well as the air outside the bubble, hence the three phase contact line. The line tension parameter $\tau$, or line energy per unit length associated with this three-phase solid-liquid-vapor contact line, plays a role in determining the contact angle of liquid droplets on solid interfaces and solid particles residing on liquid interfaces. As derived in Chapter 5, for nanoparticles at liquid interfaces, the line tension parameter is dependent upon the macroscopic wettability of the systems studied and the effects of line tension are greatest when the particle radius is extremely small (1 – 1000 nm in diameter).

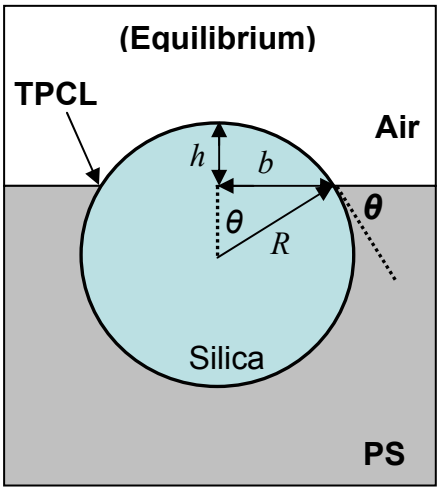


**Fig. 1.9: The height, *h* of a spherical cap protruding from the liquid-vapor interface, the lateral radius, *b* of the hemispherical cap protruding out of the liquid, and the radius, *R* of the spherical particle.**

As discussed in Sec. 5.2 many of our everyday experiences are unknowingly influenced by particles at liquid-vapor interfaces where the effects of the line tension parameter on solid particles are also present. To name only a few: the study of effects of lamellar liquid crystals in hydrophilic sunscreen,[99] fat crystals and starch granules in food emulsions,[100-102] and nanoparticle cancer treatments and targeted drug delivery mechanisims.[103-107] Understanding the line tension of these systems on the nanometer length scale is of extreme importance for further development in these fields and others mentioned in Sec. 5.2. For macroscopic experiments, the line tension $\tau$ is often neglected without repercussions due to the much larger dominant flotation and capillary forces present in these systems; however, for nanoparticle systems, where flotation and capillary forces are very small, the line tension parameter can have drastic effects on the particle wettability and equilibrium characteristics as proven in Chapter 5.

## 1.9 Motivation to Study the Line Tension Parameter of Sub-Micron Particles at a Liquid-Vapor Interface

The realization that the line tension of sub-micron sized spherical particles could be determined by examining the mechanical equilibrium of the spheres at a liquid-vapor interface occurred while Wi *et al.*[108] were comparing experimental work to a statistical mechanical theory to interpret the line tension of nanoparticles of a few nanometers in diameter at a liquid-vapor interface. In mechanical equilibrium, a sphere at this interface will be either (1) partially submerged in the liquid with only a small hemispherical cap protruding from the liquid-vapor interface, or (2) the majority of the sphere could remain in the vapor phase while only a small hemispherical portion is immersed in the liquid phase. This depends upon the wettability of the particle and line tension of the system. For the case where only a small hemispherical cap protrudes from the liquid-vapor interface, the AFM can be used to image the 3D topography of the system. 3D AFM images acquired in AC mode (see Chapter 2 for details and procedures) allows one to determine the height, $h$ that the spherical cap protrudes from the liquid-vapor interface and the lateral radius, $b$ of the hemispherical cap protruding out of the liquid with excellent resolution as shown in Fig. 1.9. The simple model developed in Chapter 5 illustrates that if $b$ and $h$ are known, in conjunction with a few experimentally measured properties of the system, the line tension parameter, $\tau$ can be accurately determined.

Obtaining *b* and *h* for spheres in equilibrium at a liquid interface has proved to be an extremely challenging task. It was first attempted by conducting experiments using hydrophobic 55 μm borosilicate spheres in hexadecane. It was determined that the combined effects of capillary waves induced by the AFM AC mode data acquisition process and the thermal motion of the spheres makes this task nearly impossible. Some success of imaging liquids on solid surfaces has been reported by Herminghaus *et al.*,[109,110] but to the best of the author's knowledge no successful reports of AFM imaging of single sub-micron solid particles at a pure liquid-vapor or liquid-liquid interface has been reported. In order to suppress the thermal motion of the particles and the capillary waves caused by AFM imaging, the spheres need to be immobilized. Previous experimental work conducted with Seemann and Herminghaus *et al.*[6] where non-crystalline polystyrene (PS) was used to study the slip length in triangular grooved substrates, led to the idea that the PS could also be used to suspend the particles in their liquid equilibrium state. Briefly, several weight percent of a solution containing dodecyltrichlorosilane coated silica particles and chloroform is added to solid PS at room temperature. The chloroform dissolves the PS and the solution can be well mixed and homogenous. This solution is then annealed at high temperature, well above the glass transition temperature of PS and the boiling point of chloroform (which evaporates off). This sample, which is now chloroform free, is then allowed to cool naturally below the glass transition temperature of PS, thus freezing the three phase equilibrium state of the spheres at the interface. With the spheres immobilized, frozen in their liquid equilibrium state, *b* and *h* can be accurately measured via AFM AC mode imaging.

## 1.10 Realistic Limitations between Experiments and the Simple Line Tension Model

Caution must be used when applying the simple model, derived in Sec. 5.3, to experiments. It is derived for the simplest and most ideal systems with non-interacting particles and does not include the effects of adsorbed contaminants on the solid spheres, surface roughness of spheres, chemical heterogeneity of the sphere coating, flotation forces and capillary forces responsible for inducing particle self assembly on the interface,[111-116] particle shape dependence,[117-124] Casmir-like interactions between particles due to thermal flucuations,[120,124-127] and irregularly shaped three phase contact lines responsible for inducing particle self

assembly.[128-130] The attributes of my experiment (listed below) demonstrate that our experimental system is sufficiently simple that use of this simple model (Fig. 1.9) is justified.

*Amplitude* and *Phase Trace* AFM imaging[131] for each tested sphere, as shown in Sec. 5.4, easily reveals if nanoscale contamination within the bulk PS is present and if the three phase contact line is pinned (see Chapter 2 for details on pinning and these types of imaging); all samples with such features are discarded. Table 5.1 shows the RMS roughness of the spheres used and also demonstrates the results are not a function of surface roughness.[132] The surface roughness of the pure solidified non-crystalline PS surface with no nanospheres present is (0.31 ± 0.02) nm over a 30 $\mu m^2$ area; thus, forming a smooth interface comparable to silicon as required by the simple model. Sec. 5.4 discusses the previously proven silanization process developed by the author and the results, based on contact angle hysteresis measurements on flat silicon substrates coated in the same manner, show that the sphere's surfaces are made of very homogeneous densely packed silane chains.[2] As shown in Fig. 5.5 the liquid surrounding the particle remains completely horizontal and free of deformations; this is a result of the insignificant weight and wetting properties of the nanospheres. With no overlap of perturbations in the shape of the liquid surface, the flotation and lateral capillary forces are non-existent. These forces can be neglected if the particle's size range is much smaller than the capillary length and the interface is non-deformed; both remain valid for this experiment (the capillary length for this system is 1.98 mm).[133] As shown by Fig. 5.8 all spheres have a uniform spherical shape and are thus perfect specimens for this simple model. The samples are uniformly heated and very slowly cooled in an enclosed environment shielded from air currents. The attenuation of the amplitude of a capillary wave traveling across the surface, or energy loss of the capillary wave, is directly proportional to viscosity;[134] thus, as the sample is slowly cooled, the viscosity drastically increases[135] and the effects of capillary waves and Casimir-like forces at the interface are drastically damped and expected to be non-existent as $T \rightarrow T_g$. Comparison of Fig. 5.6 with the valid *Height Trace* and *Amplitude Trace* imaging (see Chapter 2), shown in Fig. 5.5, illustrates the three phase contact line remains free of pinning[136] and stays horizontal and circular in a single plane around the spheres, thus eliminating any possible forces due to irregularly shaped three phase contact lines partially responsible for inducing particle self assembly on the interface. These attributes of our system make comparison to the simple model ideal.

## 1.11 Impact of Line Tension Results

Though the work conducted in Chapter 5 is being finalized for publication at the time of writing this document, its impact on the scientific community is expected to be large and well received. The work presents to the scientific community a novel experimental technique to measure the line tension of single particles on a pure liquid-vapor interface. The resolution of this method is only limited by the resolution of the AFM imaging. Bresme and Oettel[133] have specifically requested the development of experimental techniques to confirm the line tension and contact angle for particles of a few nanometers in diameter at interfaces, as existing techniques are limited. The experimental work in Chapter 5 is a step towards fulfilling this request.

Understanding, verifying, and applying new knowledge of how liquids, molecules, particles, and polymers interact at interfaces has proven to be the basis for advancement of colloidal science.[137-155] Hopefully, with future work in this area by our group and complimentary studies by other groups, recent publication sentences like the following will soon start fading from future articles: "Experimentally, line tension is typically small and hence much more difficult to measure than surface tension. This situation has caused the line tension, although a well defined thermodynamic property, to be viewed as an ill quantified property.[156]", "Line tension is a puzzling feature, a concept often referred to, but still poorly understood.[157]", "…the value of line tension is of doubtful reliability at the present, so that calculations involving the line tensions are very uncertain.[158]", and "….it is fair to say that there are no truly reliable measurements of the line tension of nanoparticles at interfaces.[133]"

# Chapter 2 - Characterization Techniques

## 2.1 Introduction to Characterization Techniques

In this Chapter the basic operational principles and characterization techniques involving atomic force microscopy (AFM) imaging, AFM force measurements, contact angle measurements, and contact hysteresis measurements are discussed. The benefits of AFM imaging compared to current state of the art electron microscopy imaging techniques are also discussed. The reader who is most interested in the results of the viscosity dependent slip length, the residuals spring constant calibration method, and the line tension parameter of single isolated spherical particles at a liquid-air interface may skip this Chapter without losing continuity of the dissertation.

This Chapter will be most beneficial for an incoming graduate student planning on continuing the AFM surface science experiments discussed within this dissertation and should serve as a starting point for AFM and contact angle hysteresis training; training for the student should be continued by following Appendix B. This Chapter is intended to be a basic introduction/quick reference to the experimental techniques used, and will highlight information not present or not easily extracted from existing conventional instructional manuals for the equipment. This Chapter is devised to only supplement the existing manuals for the AFM and contact angle measuring device, not to replace them. The manuals, though lacking explanation of the physical interpretation, do contain detailed explanations, instructions for set-up of standard operational procedures, and technical details.[*],[88,159] This Chapter is also supplemented by ~7 hours of high definition video (83.0 GB) created and directed by Sean P. McBride on basic proper laboratory procedures for an aid in duplication of this work.[†]

[*] Printed copies of these manuals are located in Cardwell Room 35 and 318.

[†] There exist numerous buck-up copies of this video tape series meant for instruction of future graduate students. Bruce M. Law retains 2 back-up copies on separate external hard drives and Sean P. McBride retains 1 back-up copy on a separate external hard drive. The table of contents of the video series can be found in Appendix D.

## 2.2 Fundamentals of AFM Imaging

The AFM is an excellent instrument for imaging interfaces with atomic resolution. Imaging with an AFM is dependent upon the AFM system possessing a cantilever with a very sharp tip, an x-y position controlled piezo scanner, a cantilever holder attached to z- position piezo crystal controlled by feedback circuitry, and a deflection detection mechanism. In this coordinate system, the x-y coordinates refers to the horizontal and back and forth motion of the stage or sample in a single plane. The z-coordinate refers the up and down vertical motion of the cantilever. Fig. 2.1 illustrates an oversimplified schematic of how these components come together to form a functioning imaging AFM system. Briefly, a laser beam is sent through a focusing lens so that it is centered on the backside of the imaging cantilever. The beam is then reflected off the cantilever to a mirror where it is reflected into the deflection detection mechanism known as a position sensitive detector (PSD); therefore, when the cantilever bends, the beam path reflected from the cantilever changes and the position of the beam changes on the PSD. The PSD typically has two photo diodes. The minute deflection of the cantilever can be obtained by examining the difference between the voltage outputs of the individual photo diodes from the PSD. A calibration of the PSD voltage and cantilever deflection can be made when the cantilever is deflected a known distance. After calibration when the cantilever is un-deflected this will correspond to zero volts on the PSD. After completing this calibration in the desired test environment (fluid or air) any sub-nanometer deflection of the AFM cantilever in the test environment can easily be determined via the PSD voltage changes; this optical beam calibration technique is known as InvOLS (Inverse Optical Lever Sensitivity).[160] This InvOLS calibration process is discussed in more detail in Chapter 4 and Appendix B.

The AFM uses the miniature cantilever with a very sharp point to trace over the topography of the interface in different imaging acquisition modes. When using an Asylum Research AFM, the interface, or sample to be imaged, moves back and forth under the tip on a set of linear voltage controlled x-y piezo crystals while the AFM cantilever tip stays stationary; this design eliminates the extreme curvature found in images acquired by Veeco AFM systems which use a singular tubular piezo crystal for all x-y-z movements. The topography of the sample is obtained by recording the interaction forces between the sample and cantilever tip and/or the signals of the z-piezo feedback as the sample is moved underneath the tip. Modern state of the art AFMs are now capable of acquiring images or forces via contact mode, AC mode, dual AC

mode, frictional force mode, piezo-response force microscopy (PFM), electric force microscopy (EFM), magnetic force microscopy (MFM), and from surface potentials with the applications of nanolithography, nano-manipulation, frequency modulation, with nearly all operations being safely conducted in fluid environments (see www.asylumresearch.com). In this dissertation the types of samples used are electrically neutral and non-magnetic; thus, AC mode imaging, also known as Tapping Mode imaging is used. Tapping mode is the most ideal form of imaging for these types of samples.

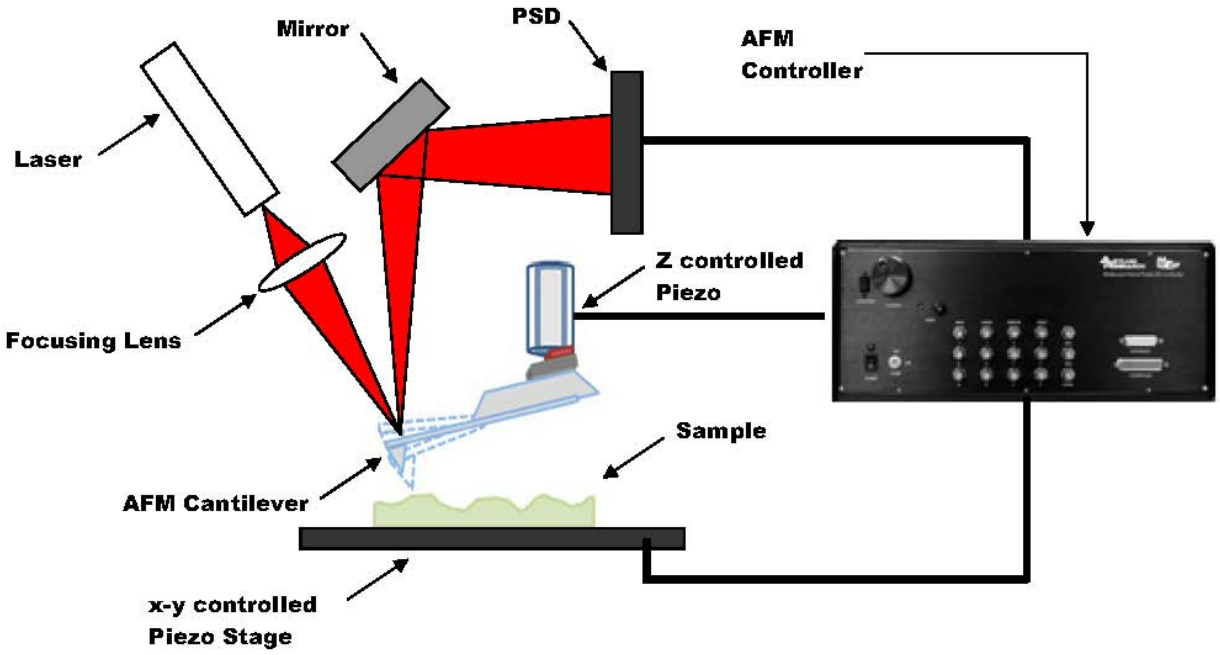


**Fig. 2.1: Oversimplified schematic of basic components present in a functioning imaging AFM.**

The naturally occurring forces between the tip and the samples determine the possible imaging modes. The following different types of imaging are possible depending upon the tip sample distance (TSD): contact mode (TSD < 0.5nm), AC mode (TSD 0.5 - 2nm), and non-contact mode (TSD 0.1 - 10nm).[161] Fig. 2.2 demonstrates the interaction forces between the AFM tip and the sample with corresponding possible imaging techniques as a function of tip-sample separation. Each will be discussed briefly.

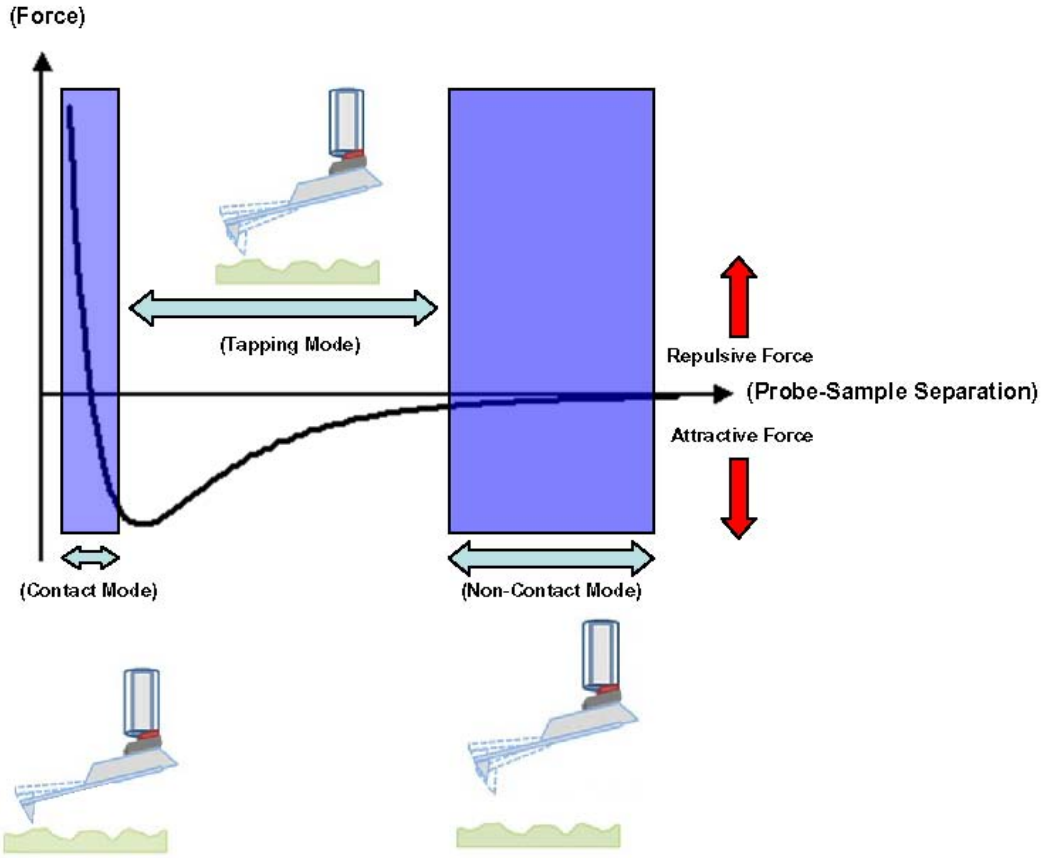


**Fig. 2.2: Interaction forces between the AFM tip with corresponding imaging techniques as a function of tip-sample separation.**

When the distance between the tip and the sample is zero, the probe is in 'contact' with the surface, hence the term contact mode imaging. The interaction between the tip and sample is however still repulsive due to the overlapping electron clouds of the sample and tip, which by the Pauli Exclusion Principle can not overlap.[162] This strong repulsion combined with the positive force applied by the cantilever leads to a deflection of the cantilever. In the most common form of contact mode imaging (constant force contact mode) the AFM feedback circuitry to the cantilever holder via the z-piezo, tries to maintain a constant cantilever deflection; thus, the force between the cantilever and sample remains constant. A topographical image is obtained by examining the displacement of the z-piezo, which moves up and down to try and maintain the constant deflection of the cantilever. A less common type of contact mode imaging is 'constant height' mode contact imaging with no feedback mechanism. In this mode, the z-position of the cantilever is held constant relative to the sample and the deflection of the cantilever is recorded as the sample moves underneath the tip. The image is then obtained directly from the deflection

of the AFM cantilever; however, the samples must be hard and flat or else the tip will crash into the sample. Constant force contact mode has the disadvantages that the sample and tip may become damaged due to the constant shear force applied to them as the sample moves back and forth below the tip. This method does not work well for soft samples in a 'dry' environment; however, performing this type of imaging under a liquid often reduces sample and tip damage. The image contrast is dependent upon how much force is applied to the sample. Atomic resolution in contact mode is possible due to the strong separation dependence of this repulsive interaction at close separation. In this mode only the last few atoms on the tip, closest to the sample, contribute to the interaction forces. This small cluster of atoms makes the cantilever have an effective tip radius on the atomic scale. This type of imaging mode is ideal for atomic resolution since the spatial resolution of an image is only as good as the sharpness of the imaging tip. Overall, contact mode imaging works well for semi-rough-hard samples, data acquisition is fast, and the best possible resolution out of all imaging types is achieved. In both types of contact mode imagining, the deflection of the cantilever is detected using the PSD, therefore, the PSD must be properly calibrated prior to imaging (see Appendix B). Contact mode imaging in both modes is best done with low stiffness spring constants (0.1 - 0.6 N/m or less).

As the tip moves away from the surface, the attractive forces due to the Van der Waals (VdW) potential dominate.[163] The origin of these attractive forces is due to the induced dipole moments of neutral atoms or molecules in the sample and AFM tip. The combination of the strong repulsive force at close contact and these attractive forces due to the induced dipole moments combine to form the Lennard-Jones potential as demonstrated in Fig. 2.2.[69] AC mode imaging (also known as intermittent mode or tapping mode imaging) in this attractive force regime is possible. In this mode of imaging, the cantilever is oscillated at or near its resonant frequency and the probe is very lightly brought into contact with the sample surface, hence the term tapping mode AFM imaging. As the sample is moved underneath the tip, the sample tip interaction forces cause the effective resonant frequency and amplitude of the oscillations of the cantilever to change. The image is obtained again by the z displacement of the piezo attached to the cantilever holder, which tries to maintain either the constant amplitude of cantilever oscillations (amplitude modulation mode) or the constant frequency of the cantilever oscillations (frequency modulation mode) as the sample is moved underneath the probe.[164] In this work, all AC mode images were collected using amplitude modulation mode; this type of imaging works

well for soft samples or samples that are fragile or loosely bound to the substrate. The disadvantages to this method are that it is more challenging in liquids, resolution is not quite as good as that of contact mode, and in terms of data acquisition this method is not as fast as contact mode imaging due to the slower scan speeds required.

Imaging in AC mode also allows for phase trace imaging. The phase trace signal corresponds to the phase lag between the cantilever drive oscillation amplitude and the actual amplitude of the cantilever. Phase trace imaging has proven to be very sensitive to variations in material properties such as adhesion, elasticity, and material components even on flat multi-component surfaces.[131] As demonstrated in Chapter 5, phase trace imaging allows for detection of contaminates in 2-component systems, which are not easily seen in the normal z-sensor or height trace imaging. In AC mode, the amplitude trace image (which is formed from the error in the Set Point amplitude of the cantilever as the sample moves back and forth below the tip) provides a very high contrast image of the sample. If collected properly, the combination of the phase trace, amplitude trace, and height trace images provides enormous amounts of information about the samples. The height trace signal is simply the voltage applied to the z-piezo to make it track the surface multiplied by the z-piezo sensitivity in unit of nm/Volts which is very carefully calibrated at Asylum Research (AR). The height trace signal provides an accurate representation of the sample height profile for samples with features less than several hundred nanometers. The height trace signal, specifically calibrated at AR for small height profiles, has less residual system noise riding on it than the z-piezo sensor signal for these length scales. When larger length scales are imaged the z-sensor signal is recommended to obtain accurate height profile information.

Another variation of AC mode imaging with the AFM is called non-contact mode imaging. This mode of imaging is the same as tapping mode imaging except that the probe never comes into contact with the sample. Rather, the probe oscillates just above the sample, residing on the absorbed fluid layer of water that exists on all samples that are not enclosed by a vacuum. In regular tapping mode imaging the probe pierces through this water layer to make intermittent contact with the sample. Non-contact mode imaging has the advantage that very small forces are exerted on the sample since no contact is made, but has the disadvantage that the image resolution is not as good. Olympus AC240TS AFM cantilevers, which are ideal for imaging 3D structures, were used for all AC mode imaging in this dissertation

## 2.3 Initial Parameters for Optimal AC Mode AFM Imaging

Following the conventional instruction manual and video tape series will yield proper set-up of the AFM to carry out these different types of AFM imaging; however, as you will soon learn, AFM imaging is almost as much of an art as it is a science. At the close tip sample distances required for imaging, the attractive forces can be quite strong causing the tip to 'snap' into contact with the sample surface due to residual static charge or capillary forces due to humidity; imaging under static charge and humidity contamination leads to poor quality/false images.

In the summer months, imaging becomes more difficult due to an increase in the humidity. The small confined space between the AFM cantilever holder and the surface to be imaged is the perfect place for induced condensation. The increased humidity causes a thick layer of water condensation on hydrophilic, even hydrophobic surfaces, and the imaging tip in this confined geometry. Once this water layer is thick enough, the two layers combine due to energy minimization of the water layers resulting in the tip crashing onto the surface. This condensation layer can easily be seen by the naked eye if a hydrophilic clean silicon substrate is used as a sample and the AFM head is allowed to sit over the substrate for 10 minutes in a high humidity environment. Once the head is removed, the water condensation layer on the hydrophilic substrate is easily seen and will dissipate in a few seconds. The increased humidity however does allow for easier static charge dissipation into more moist air. By using the environmental chamber prior to imaging, the effects of humidity can be reduced (see Appendix B for operational details). Long scan times (greater than 8-10 minutes) in the summer months are usually not recommended. The effects of condensation on the surfaces can only be eliminated when using an ultra-high vacuum AFM or imaging under a liquid.

In the winter months, though the air is drier and humidity problems are no longer an issue, the problems associated with static charge drastically increase due to the less dissipative effects of static charge in drier air. In actually, imaging in the winter months becomes much easier. This is because the static charge can be easily removed with a Staticmaster Brush from NRD L.L.C. (Model 3C500). This Staticmaster Brush contains a 500 microcurie source of the radioactive isotope polonium-210; this effectively neutralizes any static charges by emitting, for the most part, harmless alpha particles. The emitted alpha particles collide with the water molecules in the air and remove the water molecules electron's, leaving the water molecules with

either a partial positive or negative charge. The charge on the surfaces to be imaged is then removed by the interaction between the differently charged water molecules. This action only removes the charge and does not remove the actual particles/contamination causing the charge build up. It is recommended that the Staticmaster brush be used to first neutralize the charge binding the contaminants to the surface, then the samples should be rinsed with chloroform to remove the loosely bound particles, dried in vacuum, followed by a re-exposure of the samples to the polonium-210 source; this will remove both the charge as well as the contamination.

The brush was originally intended to remove static charge from photography film, optical lenses, transparencies, etc., but is essential in AFM imaging.[165] The half-life of polonium 210 is approximately 140 days and it decays directly to lead isotope 206.[166] Despite the fact that by mass, polonium-210 is around 250,000 times more toxic than hydrogen cyanide, it is only dangerous if ingested, inhaled, or absorbed through the skin.[166] Once under the skin or ingested, its high rate of alpha emission can easily damage sensitive internal organ tissue and there is no treatment currently available for this type of Polonium-210 poisoning.[165] If you accidentally ingest Polonium-210 in the lab or get it stuck deep under your skin you can call local emergency services, but it really will not make a difference in your now short and certain future; therefore be careful with these brushes, do not modify them, and certainly do not touch the polonium-210 chips!!

Prior to imaging, the AFM system and environmental chamber should be wiped down with ethanol and lens clothes and blown off with the UHP nitrogen to avoid contamination. With your samples now discharged using the Staticmaster brush and/or the humidity levels reduced using the environmental chamber you are now ready to image. The basic procedural steps are found in both the conventional manual, which should be read prior to imaging, and in the video tape series, which should also be watched prior to imaging. The steps are only briefly outlined and explained here: (1) make sure the AFM system has been cleaned/leveled, (2) put sample down on x-y stage of AFM base using the rare earth magnets, (3) re-use Staicmaster brush and/or re-purge the chamber with UHP N2 prior to imaging, (4) select the ‘Zsensor imaging’ icon on the desktop of the AFM lab computer, (5) in the ‘Master Panel’ on the far left, in the tab labeled ‘Main’, make sure that AC Mode is selected from the drop down menu, (6) now go to the ‘Sum and Deflection Meter’ on the far upper right and maximize the ‘Sum’ signal and minimize the ‘Deflection’ signal (see manual), (7) now go back to the ‘Master Panel’ and select the ‘Tune’ tab,

(8) for the AC240TS tips used, the resonant frequency is around 70kHz; therefore, select the 'Auto Tune Low' and 'Auto Tune High' options as 50 kHz and 90 kHz, respectively, (8) set the 'Target Amplitude' to 1.0V and the 'Target Percent' to -5%, (9) now click on the 'Auto Tune button', (10) now go back to the tab labeled 'Main' in the 'Master Panel' and make the following adjustments: 'Scan Size' 10μm, 'Scan Rate' 0.8Hz, 'Scan Angle' $90^{o}$, 'Scan Points' 512, 'Scan Lines' 512, 'Width:Height' to 1:1, 'Set Point '700mV, 'Integral Gain' 10, and click on 'Save Images' box (make a new file folder if necessary), (11) now go back to the 'Sum and Deflection Meter', minimize the deflection, and click the 'Engage' button to initiate a 'Hard Engage' (see manual or Appendix B for details on 'Hard Engage'), (12) then go back to the 'Main' tab in the 'Master Panel' and select 'Do Scan' button. Once the AFM starts to scan the surface, these initial imaging parameters can be optimized.

After completing thousands upon thousands of AFM scans, I had found the above general outline of steps and initial parameters will work for most samples. It is important that the AFM head remain level and maintain the same position during all AFM imaging and force measurements. If the AFM head is not kept level during AFM imaging, then the orientation of the cantilever is different from image to image, producing different quality and/or contrast images. Having the AFM head level for each image produces the least tip-sample artifacts in the images and serves to have a continuously known orientation of the cantilever and image quality. If the AFM head is not level in force measurements then the cantilever is not level with the sample, this leads to complicated variations in the AFM spring constant. The use of the magnets is required to make the sample immobile. Again, just before imaging, it is always best to use the environmental chamber and/or Staticmaster brush.

With the 'Sum' signal maximized and the 'Deflection' signal minimized, 'Auto Tuning' the cantilever with a 1.0V Target Amplitude means that there is 1.0V worth of sine wave on the PSD detector; choosing a 'Target Amplitude' of -5% means that the 'Drive Frequency' will be 5% off the maximum 'Drive Amplitude' of the cantilever at the resonant frequency. The minus indicates that the drive frequency will 5% less than the resonant frequency of the cantilever and you will be operating in the 'Repulsive Mode' when engaged on the sample. For softer samples which can only tolerate small forces a +5% V value can be used as the 'Target Amplitude' and the AFM will operate in 'Attractive Mode' imaging (see manual for differences in Attractive and Repulsive Modes). Here the 'Set Point' controls how much force is imparted to the sample. If a

900mV is used for a 'Set Point' value, this means that the free oscillation amplitude of the cantilever, which is now oscillating at 1.0V is only damped by 100mV from the surface interactions between the tip and the sample. This small applied force preserves the sharpness of the tip, but for surfaces with large features the tip may not track the surface well. The recommended 700mv works very well for most surfaces. If the surface is hard enough the 'Set Point' can be lowered to 500mV.

Using a 'Scan Size' of 10μm and a 'Scan Rate' of 0.8Hz produces a 'Scan Speed' of 19.93 μm/s. This combination of 'Scan Size' and 'Scan Rate' has been proven to provide the most efficient scanning rates with acceptable resolution for 10μm samples. The images you will want to collect will not all be 10μm so you will have to adjust the 'Scan Rate' accordingly. As a rule of thumb, when the 'Scan Size' decreases the 'Scan Rate' should increase. In general, the slower the 'Scan Speed' the better the AFM will track the surface; however, if the 'Scan Speed' is comparable to the thermal drift in the system, the image quality will be very poor. When this happens, the sample is moving nearly at the same speed as the thermal drift and the images you obtain are worthless. Depending upon the seasons and the laboratory conditions, the thermal drift of our AFM can be anywhere from 50-200nm over a 10 minute period. This is huge compared to modern AFMs which are stable in the several nm regimes over several hours or better. For small images on the 300x300 $nm^2$ area, image collection time should be no longer than 1-3 minutes to beat the thermal drift in our system. Making measurements below 300x300 $nm^2$ for this system takes great care in imaging and pushes the limits of reliability of the system. The drift can be reduced by having a thermally isolated acoustic chamber for the entire AFM system. For images with an area of only a few hundred nanometers squared, it is recommended that the scan rate be varied from 1.0 – 3.0 Hz, this will produce scan speeds from 0.6 -2.25 μm/s. The thermal drift of the system can also be reduced by leaving the laser shine on the cantilever for 30-60 minutes prior to imaging (the same goes for doing force measurements, but not as important). To reduce the thermal drift from the electronics, it is suggested that the controller to the AFM always remain on, only turning off the power to laser in-between experiments or imaging sessions.

The 'Scan Angle' should be at $90^o$, this means the direction at which the sample moves underneath the tip is not on the same axis as the longest part of the cantilever, but rotated so that the sample moves along the cantilever's shortest axis. If the cantilever's long axis is oriented in parallel with the direction motion of the substrate the cantilever is more susceptible to unwanted

deflection due to cantilever buckling; this is related to the different stiffness of the cantilevers in the *x* and *y* directions.[167] For high quality resolution in a short time frame, the 'Scan Points' and 'Scan Lines' should be set to 512 x 512 (any higher the needed scan time significantly increases). It is recommended that a quick lower quality scan of an area be performed first before a more detailed scan is acquired; this is accomplished by changing the 'Scan Lines' from 512 to 128. The quick scan is done to see the overall morphology quickly with less detail; one can get through 8 minutes of a high quality scan on a 10x10 $\mu m^2$ area and then realize that there is an abnormal dust spec in your image and it is now worthless; a quick one minute scan of the same 10x10 $\mu m^2$ area would have told you that before you did the high quality scan.

The last parameter that needs explaining is the 'Integral Gain'. The 'Integral Gain' describes how fast the z-piezo responds to surface structures on the samples. The higher the 'Integral Gain' the faster the z-piezo responds. Therefore, for surfaces that have large height features it will require a higher 'Integral Gain' than for surfaces that are flat, which will require the minimum 'Integral Gain'. The 'Integral Gain' should be high enough to track the surface, but not high enough to cause "ringing" in your images. This "ringing" is due the feedback circuitry not being able to respond to such a high 'Integral Gain'. The "ringing" on your image will show up as ripples following pronounced height features on the sample, like those on a pond after a rock is thrown in. If the image is flat with no height features the resulting image will look blurry if the 'Integral Gain' setting is too high. As a general rule, if the 'Set Point' needs to be lowered because there are more sharp asperities or deep narrow valleys on the surface, this also means the 'Integral Gain' should increase to respond faster to all the peaks and valleys. In general, if the 'Scan Size' is lowered the 'Integral Gain' should also be lowered.

As stated earlier, AFM imaging is almost as much an art as it is a science. These aforementioned parameters are not set in stone, they are meant to be a starting point. The ultimate objective of AFM imaging is to acquire the best possible resolution image in the most efficient manner by varying the feedback parameters so that the AFM tip tracks the sample best, this is the ultimate goal. If you tweak a parameter and the height profile shows that the height trace and height re-trace line up better, then this parameter is the better parameter to use. The height trace and height retrace are the height profiles of the sample in a single scan line as the sample moves back and forth under the tip. Each type of image signal (i.e. Height, Amplitude, Phase, Z-sensor, etc.) has a trace and a retrace component. If the image parameters are

optimized, the height trace and height retrace lines should be exactly overlapping each other with no “ringing”. A significant amount of time can be lost imaging if not conducted in an efficient manner. Retrieving, removing the image artifact of curvature, other artifacts of image acquisition, and imaging manipulating are all well described in the manual.

## 2.4 Tricks of the Trade for AC Mode AFM Imaging

One of the largest problems with AFM imaging on a budget is how to prolong the life of the imaging tips ($1000/35 tips). If they get contaminated they can usually be cleaned and reused many, many times before they become dull and unusable. The information below describes what signs to look for when determining if a tip needs cleaning or needs to be discarded. A ‘Hard Engage’ will need to be performed, see manual. Before performing the ‘Hard Engage’ the z-piezo is fully extend to its 150V maximum and the cantilever can oscillate freely at the 1.0V amplitude. To start the ‘Hard Engage’, the large thumbwheel is moved counter clockwise to lower the AFM head onto the sample. When a beep sound from the computer is heard that means the amplitude of the cantilever has reached the ‘Set Point’ value. The cantilever is now interacting with the surface and all the feedback circuitry is activated. The thumbwheel can then be lowered so that the z- piezo is in the approximate center of its range of mobility at 70V. Before the ‘Hard Engage’ one should take note of the ‘Phase’ value when the cantilever is oscillating with its free amplitude unaffected by the surface interactions, typically this is around 70-75$^{o}$ using the initial parameters mentioned. After the ‘Hard Engage’ is completed, the tip is interacting with the surface and the ‘Phase’ should change to about 65-70$^{o}$ and be very stable. If a lower ‘Set Point’ is used (i.e. 500 mV) the ‘Phase’ can go as low as 40$^{o}$, but it should still be very stable. If the ‘Phase’ signal starts jumping around wildly from positive to negative or is very unstable and drifting after the ‘Hard Engage’, this is a sure sign of contamination, static charge, a damaged tip, or humidity problems. Before starting over or switching to a new tip try manually increasing the ‘Drive Amplitude’ voltage slightly (this parameter was initially determined form the ‘Auto Tune’ procedure), if it still has erratic behavior on the ‘Hard Engage’ it is most likely due to the previous discussed problems. Increasing the ‘Drive Amplitude’ slightly gives the tip a little bit more energy so as to be removed from the surface of ‘sticky’ samples.

There exists a variety of ways to clean the cantilevers. The first simple cleaning method is to take the cantilever and place it in the custom delrin holder and rinse it well with chloroform and dry it with a heat gun. Alternately, this can also be done by leaving the cantilever in the AFM cantilever holder, rinsing it with chloroform, drying the front and backside of the holder with low pressure UHP nitrogen, and then vacuum drying the holder for 5 minutes. If imaging in a fluid, follow the cantilever cleaning instructions in Appendix B. *Vacuum drying is critical; if chloroform is not removed from the backside of the holder the AFM will short out the electric connections between the AFM head and AFM holder which contains the z-piezo.* The second method is preferred since it involves less handling of the cantilevers. This usually will remove the contamination and imaging can continue. If this still does not fix the problem, then first expose the cantilevers to the short range UV-Ozone cleaner for 5 minutes to 1 hour, then repeat the chloroform rinse and dry (with a heat gun or vacuum method), and then use the Staticmaster brush. If this does not fix the problem, thoroughly rinse the cantilever in chloroform, then plasma clean the cantilever for 10 minutes in the Chemistry department (see Dr. Takashi Ito for simple instruction and permission) followed by the Staticmaster brush. If this does not fix the problem there might be permanent tip damage or permanent contamination on the tip. Piranha solution (Chapter 4) can be used to remove this permanent contamination; however, the piranha solution will also strip off the reflective coating of aluminum of the backside of the cantilever making the 'Sum' signal much lower when it is reused. Even though the 'Sum' signal is lower, this does not affect the AFM imaging as long as the drive amplitude is sufficient, but not too high. The aluminum can be re-deposited via physical vapor deposition in the Chemistry department if desired (See Dr. Dan Higgins for permission and Appendix E for instruction). After the piranha cleaning the cantilever's life span is very short and will contaminate easily due to the highly clean hydrophilic surface it now possesses. Once these options have been attempted and if the phase behavior is still erratic the cantilever is no longer of any use and must be discarded.

## 2.5 Advantages of AFM Imaging Compared to Electron Microscopy Imaging Techniques

As stated in much of the current literature, accurate experimental determination of contact angles (or small height features) on collections of (or especially on single) particles or interfaces less than a micrometer on any interface is extremely challenging. [127,133,156,168-176]

Optical microscopy techniques on nanoparticles at interfaces are limited by the diffraction of light and can only provide qualitative information below 250 nm. To make accurate observations below the 250 nm barrier in colloidal science electron microscopy (EM) techniques have been employed. Past and present EM techniques will be discussed briefly.

Freeze-fracture/freeze-etch transmission electron microscopy (TEM) or freeze-fracture/freeze-etch scanning electron microscopy (SEM) techniques are currently being used, as they have for decades, [99,177-186] to study the internal structure of emulsions. Here the samples are frozen and then fractured to examine the internal make up of the samples. This technique has limited applications in studying interfaces in equilibrium. Low energy scanning transmission electron microscopy (STEM) was developed with the specific intent of studying biological interfaces that are beam sensitive with a resolution of 10-20 nm.[187-189] Binks and Kirkland have shown that low temperature field emission scanning electron microcopy (LTFESEM) can also be used to verify the presence of particles as small as 10-30 nm on emulsion interfaces.[190] Environmental scanning electron microscopy (ESEM) using low vacuum conditions has also been used to study interfaces of hydrated samples.[191-195] Brugnara *et al.*[193] used ESEM to measure contact angle measurements on micron sized water droplets on polymethylmethacylate and commercial grade wax. Matthews and Donald have determined the resolution of the ESEM to be a few tens of nanometers under optimum conditions.[196] Wet scanning transmission electron microscopy (wetSTEM) (a STEM detector inside an ESEM) can be used not only to examine the hydrated interfaces of the emulsions as ESEM does, but also allows one to probe several microns beneath the interface. Using wetSTEM on gold nanoparticle colloidal suspensions 5 nm resolution has been achieved by Bogner *et al.*[197] Barkay[198] used wetSTEM in an ESEM to obtain contact angle measurements of nano water droplets with a diameter of 100-400 nm. Recently, Dyab and Paunov[199] have revealed the structure of particle stabilized emulsions in situ by using wet scanning electron microscopy techniques (wetSEM). Like ESEM and wetSTEM, wetSEM requires no freezing or extensive sample preparation and uses low vacuum for hydrated samples. Imaging using wetSEM has resolutions of 20 nm in a fully wet state without dehydrating or coating with a conductive material and allows for observations below the sample interface to a depth of ~ 2 μm.[200] Bogner[201] gives a very detailed explanation of the operation of each of these EM techniques and an excellent account of the history behind their development.

These electron microscopy methods all have the same inherent disadvantage when compared to AFM; no direct/immediate information can be gained about the height profile of particles on the interface. For instance in Chapter 5, determining the height above the interface that a particle protrudes is essential for determining the microscopic contact angle and the line tension parameter, $\tau$ of a particular system. As shown by Barkay and Brugnara *et al*., quantifying the 2D STEM images into 3D shapes is non-trivial. In the EM techniques discussed, 3D images can be reconstructed via electron tomography[202-204] or by other non-trivial means.[205] Typically the spatial resolution of TEM tomography is on the range of 3-8 nm.[202] Recently, Sousa *et al*.[206] have shown it is possible to detect the 3D distributions of nanogold atom clusters consisting of 11-gold atom clusters and 1.4 nm diameter gold particles using STEM tomography.

The AFM has the distinctive advantage over these cryogenic and non-cryogenic forms of EM in that the height profile of the interface being studied is readily available with excellent precision (sub nanometer resolution) and with no additional sample preparation. The AFM has the added advantage that samples do not have the large scale (~ 50 nm) image artifacts such as ice crystal formation as does cryo-EM techniques[207-209] nor do AFM samples acquire damage (local heating due to beam irradiation) when high resolution/magnification is desired. Creating EM samples that form a vitrified, or glassy, ice state instead of the damaging crystalline ice state is possible; however, this still requires additional sample preparation.[210] Zhang and Ducker have recently taken advantage of the benefits of AFM and have successfully applied taping mode imaging to observe nano-oil drops of decane on a solid-liquid interface (height of droplets ranged from 2-500 nm).[211,212] As a result of these benefits, AFM has become one of the primary tools in studying phase separation in lipid membranes where height resolutions of 0.3 nm or better are needed to see the raft formation of lipid bilayers on interfaces.[213-220] The AFM has also been used for the visualization of the line tension parameter $\tau$ at work in 2D networks of gold nanoparticles obtained by the Bubble Deposition Method.[221] EM and AFM applications each have advantages and disadvantages depending upon the system that is being studied.[201] The primary disadvantages of the AFM are the longer times needed to acquire images and imaging on liquid-liquid interfaces is very difficult.

## 2.6 Surface Force Measurements with the AFM

As previously discussed, any measured force with the AFM, regardless if using colloidal or non-colloidal probes, is always defined as $F = k \cdot x$, where the vertical deflection of the colloidal/non-colloidal probe, $x$ is multiplied by the colloidal/non-colloidal probe spring constant, $k$. Thus, the fundamental parameter measured by the AFM is the vertical deflection of the cantilever which is caused by the interaction forces between it and the sample. Just as in contact mode imaging, the deflection of the cantilever is detected by the PSD, which needs to be properly calibrated (Chapter 4 and Appendix B). The measurement of the force is only as accurate as the accuracy of the determined spring constant. For non-colloidal cantilever the preferred method of spring constant calibration is the thermal method using the computer software interface provided with the AR MFP-3D (see manual and Appendix B). With practice, this becomes a quick and trivial procedure for rectangular/triangular non-colloidal probes giving excellent results. For colloidal probes in a viscous fluid the residual calibration method is essential for determining the correct spring constant. If the thermal method is used for colloidal probes the resulting spring constant may be 20-25% lower than the actual in situ value in the experiment, as determined by the residuals calibration method (Chapter 4).

The force curves acquired from the AFM will look very different depending upon the type of cantilever used and the environment being tested. Fig. 2.3 and 2.4 illustrates schematics of force curves taken in air, liquid at slow speed, and liquid at high speed. Each region of the force curves will be discussed briefly. For a non-colloidal probe in air (Fig. 2.3) region 1 represents where the cantilever remains un-deflected as it approaches the surface (zero Volts register on the calibrated PSD). This region should always remain horizontal and look like Fig. 2.3 (red line). If there is a long range bow to the data in region 1, as illustrated by the black dashed line, this is a result of static charge which has not yet been removed (use Po-210 source). If the data has a positive or negative slope to it in region 1 this is due to a phenomenon know as 'Virtual Deflection' which has not yet been removed (see manual and Appendix B). There will always be to some extent a very small region where the probe snaps into contact due to the minute surface and van der Waals forces; this snap to contact region is usually less than 10nm and not easily seen on micron scale force experiments using stiff cantilevers. Region 2 is where the cantilever tip first makes contact with the solid surface onto which it is pressing; as the z-piezo continues to extend the cantilever bends in a linear fashion. It should be noted that if a

deformable substrate is used the slope in region 2 may not be linear. If a hard substrate is used, and the cantilever is in contact with the substrate, the rate of deflection of the cantilever will be equal to the rate at which the cantilever is being lowered by the z-piezo (thus the slope should be unity). Therefore, the value of the slope in region 2 can give information about the hardness and elasticity of the sample. In region 3 the z-piezo is retracting (blue line) but the cantilever tip is still in contact with the surface so it simply retraces its original path from region 2. Notice that the path in region 3 now extends past zero volts (or zero deflection); this is because the tip has been stuck to the surface due to an excessive amount of force (i.e. indentation of the surface) and/or capillary and adhesion forces are present. As the z-piezo continues to retract there eventually comes a point when the attractive forces at the surface are overcome and the cantilever is released from the surface; this is region 4. Therefore region 4 gives us a direct measure of the adhesion forces between the cantilever tip and substrate. In region 5, the cantilever simply retraces its path back to its starting position, remaining un-deflected just as in region 1.

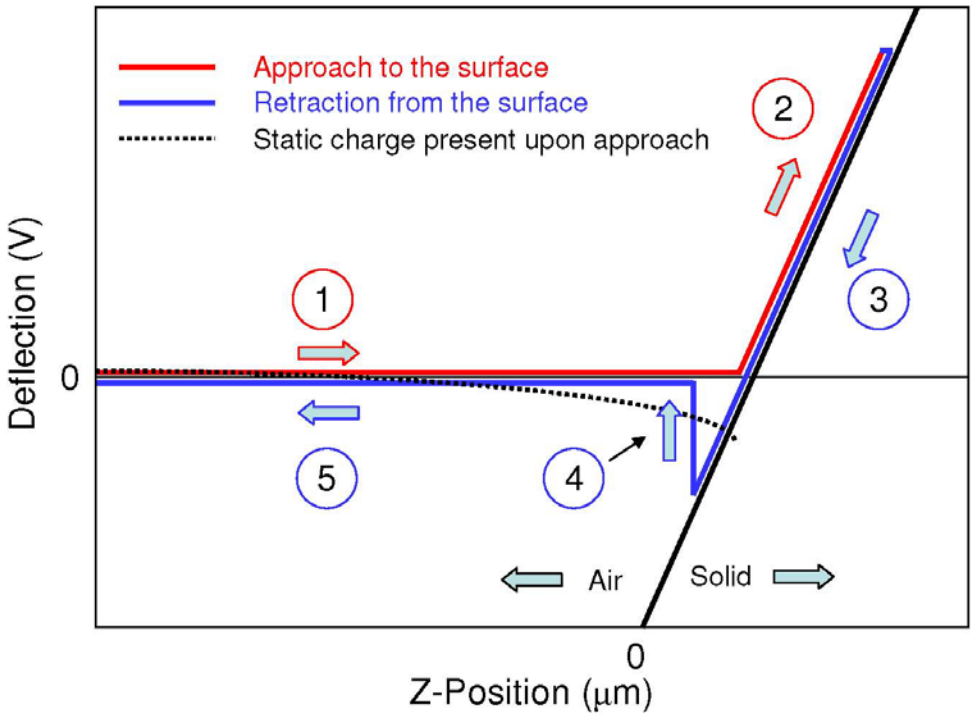


**Fig. 2.3: Approach and retraction force curves in air for a non-colloidal probe.**

The force curves for a colloidal probe in air will look nearly identical to the ones for a non-colloidal probe in air with the exception that the adhesion force is usually less because there is no sharp tip to indent into the substrate. If a non-colloidal probe with low drag is used in a fluid the force curves will also look similar to Fig. 2.3 with less of an adhesion force as the fluid in most cases acts as a solvent. If the velocity is high enough, the drag on the non-colloidal probe in liquid will introduce some non-linearity in regions 1 and 5. It should be noted that when plotting the deflection in nanometers (instead of Volts), Figs. 2.3 and 2.4 will look exactly the same; this is because the software simply uses the InvOLS calibration factor to produce the deflection (nm) vs. z-position (or LVDT) (nm) graph.

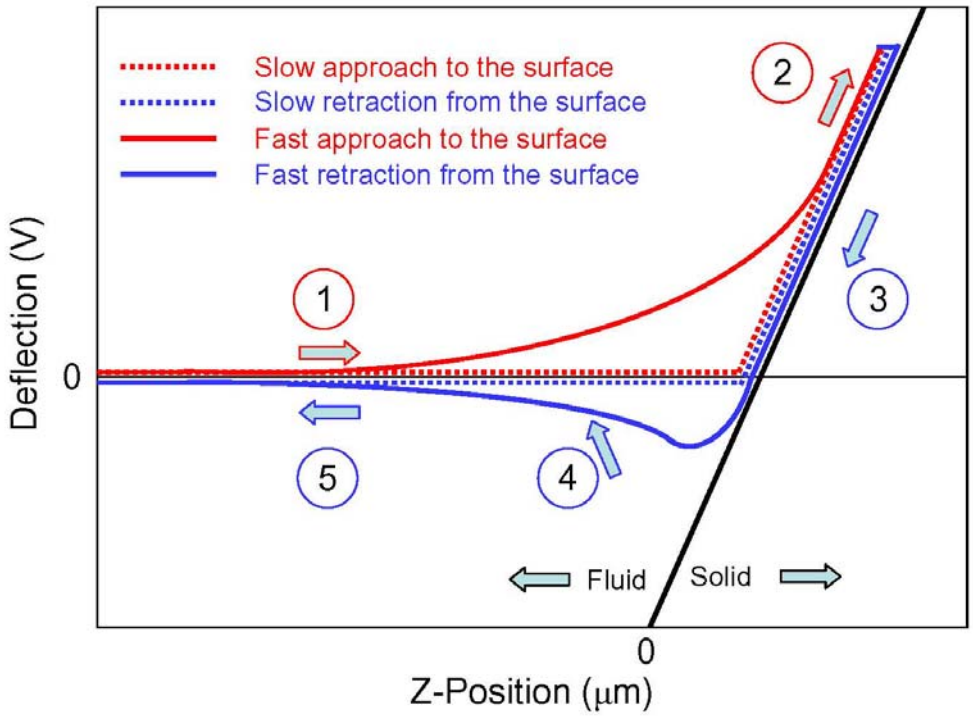


**Fig. 2.4: Approach and retraction force curves for a colloidal probe in liquid at different speeds.**

For a colloidal probe in a liquid, as in Fig. 2.4, the force curve looks very different depending upon the speed of approach and retraction. In region 1 the probe is being driven to the surface by the z-piezo. The force on the colloidal probe is dependent upon the velocity of the probe and is given by,

$$F_h = \frac{6\pi\eta r^2 v\psi}{h}. \qquad (2.1)$$

Therefore, the larger the approach or retraction velocity the larger the hydrodynamic force (see Chapter 3, 4, and Appendix A for details and derivation of Eq. (2.1)). This fact explains why the force curve at slow speeds in a liquid looks nearly the same as those for a non-colloidal probe with a small or nearly zero adhesion force.

Fig. 2.4 shows that as the separation distance between the apex of the colloidal probe and the substrate, *h* becomes smaller, the hydrodynamic force on the colloidal probe at constant velocity increases; this is consistent with Eq (2.1) and explains the shape of region 1. Region 2 shows when the sphere apex makes hard contact with the substrate. As the z-piezo further extends the slope of region 2 should again be unity, this confirms hard contact. In order to establish a zero point for slip length measurements it is important to confirm that hard contact between the sphere and substrate is made when doing hydrodynamic experiments (Chapter 3, Chapter 4, and Appendix B). In region 3, the z-piezo is retracting (blue line) but the cantilever tip is still in contact with the surface so it simply retraces its original path from region 2. Again, notice that the path in region 3 now extends past zero volts (or zero deflection); this is because the colloidal probe is attracted to the interface from capillary and adhesion forces. As the z-piezo continues to retract the attractive forces at the surface are overcome and the cantilever is gradually released from the surface; this is region 4. In region 5, the cantilever tries to retrace its path back to its starting position. Appendix B provides a more thorough step by step procedure with technical details using the Igor Pro software to obtain accurate colloidal probe force measurements and acquire accurate slip length measurements.

As suggested previously, the slope of region 2 can yield information on the elasticity or stiffness of a surface (or object). In a collaboration with Govind Paneru and Bret Flanders *et al.*[5], this characteristic of the AFM force curve was used to determine the spring constants of poly3,4-ethylene dioxythiophene (PEDOT) filaments used in cellular environments. Knowing the spring constant of these wires allowed for the determination of forces at individual pseudopod-filament adhesive contacts. The force on the wire by the cantilever and the force on the cantilever by the wire must be equal and opposite by Newton's third law. Using this knowledge and following the work of Gates and Reitsma[222] it can easily be shown that the spring constant of the nanowire filament must be,

$$k_{Filament} = k_{AFM}\left(\frac{1}{\cos^2\theta}\right)\left(\frac{L-\Delta L}{L}\right)^3\left(\frac{InvOLS_{AFM}}{InvOLS_{System}-InvOLS_{AFM}}\right). \qquad (2.2)$$

The term to the third power takes into account any off-end loading (overlap between filament and cantilever) and the geometric term takes into account the tilt of the AFM cantilever. In this equation, $k_{AFM}$ is the spring constant of the AFM and is determined by the thermal method,[81] $\theta = 11^{o}$ is the angle of the AFM cantilever, $L$ is the length of the wire and is measured by scanning electron microscopy (SEM), $\Delta L$ is the overlap between the AFM cantilever and filament measured using the internal 10x AFM microscope having resolution of 437 nm per pixels. $InvOLS_{AFM}$ is the sensitivity of the AFM cantilever when pushed against a hard surface as previously described, and $InvOLS_{System}$ is the sensitivity of the combined system of the AFM cantilever and nanowire when they are pushing against each other. A second paper is in preparation with Paneru and Flanders[7] demonstrating that this method is in excellent agreement with a nanowire vibrational analysis which leads to an independent method of spring constant determination of the PEDOT filaments.

## 2.7 Contact Angle and Contact Angle Hysteresis Measurements

Being able to measure the static contact angle and contact angle hysteresis of samples in the experiments conducted is a necessity for characterizing the wettability, chemical homogeneity, and chemical quality of a sample's surface. The information gained from the static contact angle shown in Fig. 2.5 describes how hydrophobic or hydrophilic it is while the contact angle hysteresis describes how chemically/physically smooth the surface or surface coating is.[223] A First Ten Angstroms 100 Series long range optical microscope has been used extensively throughout this work to make these types of measurements

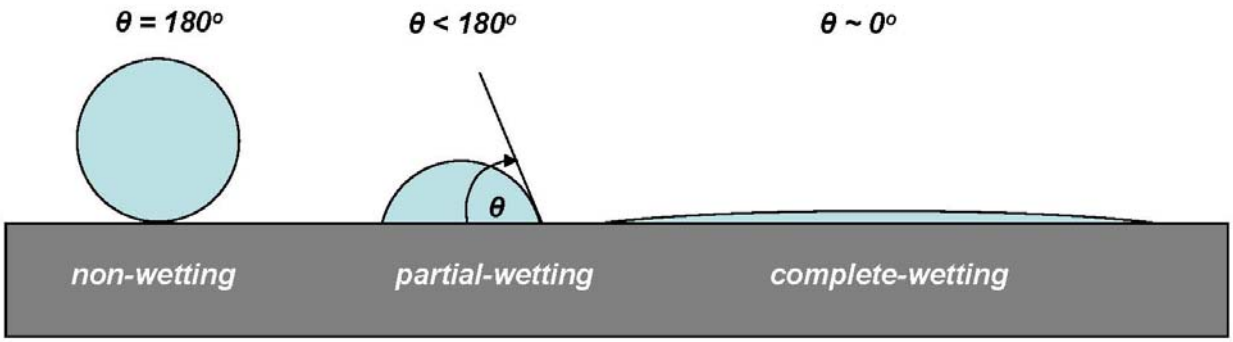


**Fig. 2.5: Different degrees of wettability.**

The contact angle is defined as the angle a liquid droplet makes with a solid surface as shown in Fig. 2.5. This angle is dependent upon the interfacial properties of the liquid-vapor, liquid-solid, and solid-vapor interfaces (Chapter 5). A liquid that completely wets a sample surface will spread over the surface into a thin film with a zero degree contact angle. If a liquid only partially wets the sample surface the drop will remain spherical and have a contact angle less than $180^{o}$. If a liquid does not wet the sample surface at all (i.e. non-wetting) then the liquid will remain in a spherical shape with a contact angle of $180^{o}$. At the three phase boundary line of the liquid droplet there exists three of surface energies, $\gamma$, which balance each other to leave the droplet in mechanical equilibrium on the surface as shown in Fig. 2.6. The contact angle defined by this balancing of the three interfacial surface energies, $\gamma$ is known as the Young equation

$$\cos\theta_{\infty} = (\gamma_{SV} - \gamma_{SL})/\gamma_{LV} . \qquad (2.3)$$

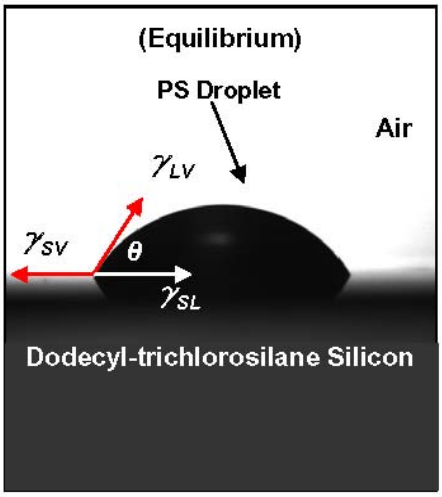


**Fig. 2.6: A molten drop of polystyrene solidified onto a chemically altered silicon substrate displays the interfacial forces balancing at the three phase contact line.**

When a surface possesses a physically varying surface (i.e. is rough) then the Young equation can become ill-defined at sharp points on this surface. At these ill-defined points, the three phase contact line becomes 'pinned' or immobilized.[136] Likewise, if the sample surface has a spatially varying chemical coating the liquid will want to maximize the contact area with the wettable areas while minimizing the contact area with the less wettable parts of the substrate. Therefore, when the liquid front moves across the surface, these sharp topographical points or differences in surface wettability act as anchors and barriers, and a visible change in the dynamic contact angles on macroscopic length scales occurs. These observations are impossible to observe with a simple static contact angle measurement. To make the liquid front move across

the sample surface a Kent Scientific Genie Plus syringe pump was used. To make the liquid front advance, the syringe tip is left in the droplet and the volume of the drop is increased as the plunger is systematically depressed by the pump. Likewise, to make the front regress across the surface, the liquid is retracting back into the syringe reducing the volume of the droplet. To determine the contact angle hysteresis a video of this expanding and contracting volume of the droplet is taken. Contact angle measurements are made during each frame of the video. The contact angle hysteresis is defined as the contact angle during expansion minus the contact angle during retraction. For the fictional perfectly smooth sample that has no physical or chemical surface roughness the contact angle hysteresis should be zero; however, in reality, there is always some degree of hysteresis. The lowest contact angle hysteresis value I have recorded is one degree and I have also seen samples (none of mine) that have been completely pinned[136] upon retraction of the fluid.

Fig. 2.7 illustrates an example of contact angle hysteresis $\Delta\theta = \theta_A - \theta_R$ as a function of droplet volume; $\theta_A$ represents the advancing contact angle during the drop's expansion and $\theta_R$ represents the receding contact angle during the drop's reduction in volume. The results presented in Fig. 2.6 are from a collaborative work with Baljinder Kaur and Warren T. Ford *et al.*[4] In this work, AFM images and contact angle hysteresis measurements of semifluorinated latex films of varying degree were needed to test the integrity of the films after exposure to compounds similar to organophosphate chemical warfare agents. Smaller contact angle hysteresis, $\Delta\theta$ of less than 3 degrees, is found for the surfaces where the slip length parameter and the residuals spring constant method were investigated using colloid probe AFM in Chapters 3 and 4.

If a sample is extremely rough, either chemically or physically, the advancing contact angles will also have an additional non-linearity as a function of volume. The same can be said for the receding contact angle. These effects make determining the contact angle hysteresis very difficult. Notice that no non-linearity is present in Fig. 2.7, the advancing contact angle remains constant as a function of volume. The same can be said for the receding contact angle after a certain point. In most cases where non-linearity has been seen in the samples of others, the surfaces were either visibly contaminated or not properly stored and the results most likely do not appropriately characterize the real underlying physical topography or chemical quality of the

surfaces. If the samples are clean, the non-linearity could be due to chemical activity at the three phase boundary line as it moves across the sample.[4]

Following the manual for the First Ten Angstroms 100 Series long range optical microscope should yield proper data collection. The most important steps for contact angle measurements and contact angle hysteresis measurements are: 1) to have the x-y-z- stage leveled, 2) calibrate the distance on the image screen using the tip width of a micrometer syringe needle measured with a set of Vernier calipers (do not trust the published value of the syringe tip width), 3) adjust the light so that best contrast is achieved (without over exposure producing false results), 4) have all needles free of air bubbles, and 5) thoroughly clean and flush all syringes with the desired test liquid prior to using. The results of these measurements are very sensitive to contamination and all syringe components must be extensively cleaned prior to flushing with the desired test liquid. Fresh liquids must be used for each test and the syringe components must be thoroughly cleaned ***after*** each experiment. When using the First Ten Angstroms 100 Series long range optical microscope for interfacial surface tension measurements it is crucial that it be properly calibrated as outlined in the manual. One must also keep in mind that when the temperature of the system is increased or decreased all calibrations including density of the test liquid must be changed as a function of temperature!

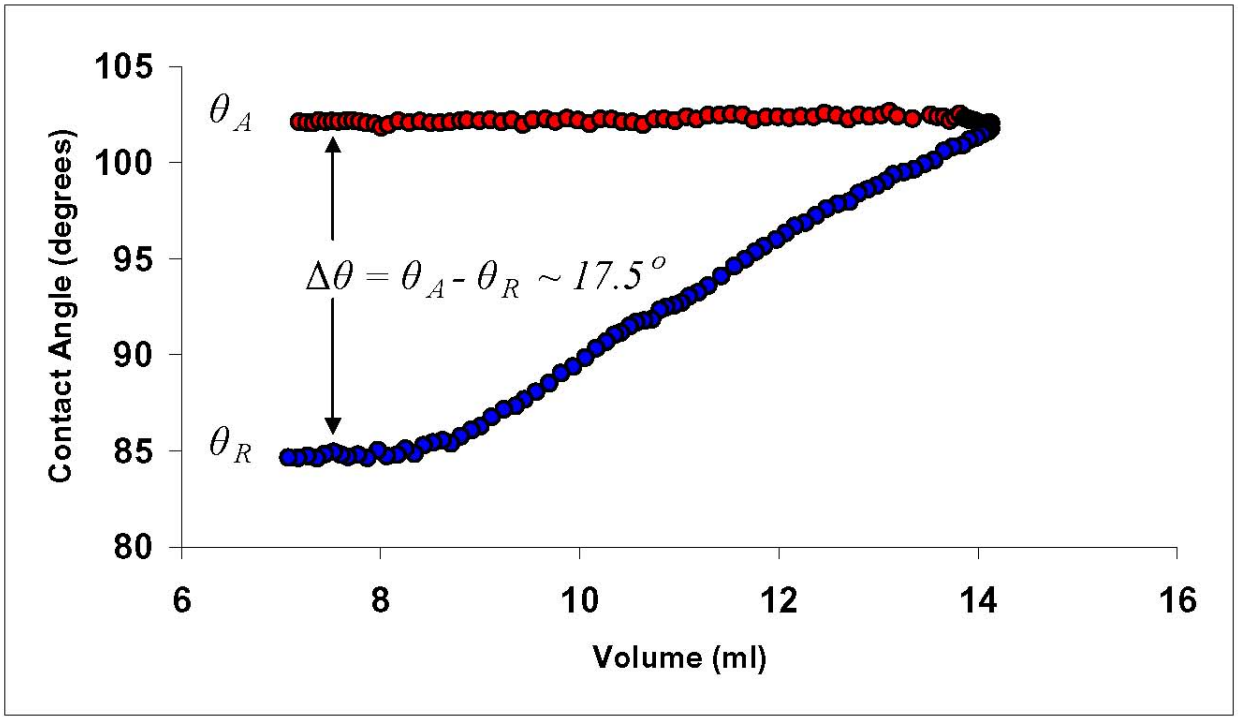


**Fig. 2.7: Definition of Contact angle hysteresis. Collected when dispensing at ~ 10 µL/min.**

# Chapter 3 - Viscosity-Dependent Liquid Slip at Molecularly Smooth Hydrophobic Surfaces[‡]

## 3.1 Overview of Viscosity-Dependent Slip

Colloidal probe Atomic Force Microscopy is used to study the slip behavior of eighteen Newtonian liquids from two homologous series, the n-alkanes and n-alcohols, at molecularly smooth hydrophobic n-hexadecyltrichlorosilane coated surfaces. We find that the slip behavior is governed by the bulk viscosity $\eta$ of the liquid, specifically, the slip length $b \sim \eta^x$ with $x \sim 0.33$. Additionally, the slip length was found to be shear rate independent, validating the use of Vinogradova slip theory in this work.

## 3.2 Introduction

When discussing fluid flow over a solid object, it is customary to apply the Navier-Stokes equations assuming no-slip Boundary Conditions (BCs) such that the fluid velocity relative to the solid is zero at the solid-liquid interface.[224] This no-slip BC has successfully described macroscopic experiments for many years. However, recent experiments on confined liquids have demonstrated that partial slip frequently occurs at the solid-liquid interface, leading to a non-zero fluid velocity adjacent to the solid surface. Slip behavior is described by the slip length *b*, which is defined as the extrapolation distance into the solid surface where the fluid velocity would be equal to zero. The study of slip BCs has become a subject of increasing importance with the advent of micro and nanofluidic devices.[225] Experimental slip lengths from nanometers to microns have been reported in the literature.[224] Unfortunately, reliable measurements of the slip length have proven to be difficult to obtain.[53,226] As such, there are ongoing discussions not only as to what physical phenomena cause slip, but also which of the numerous experiments constitute reliable slip measurements.

---

[‡] Reprinted with permission from Sean P. McBride and Bruce M. Law, Physical Review E, 80, 060601(R), (2009). © 2009 The American Physical Society. Viscosity-dependent liquid slip at molecularly smooth hydrophobic surfaces by Sean P. McBride and Bruce M. Law. Proof of permission granted found in Appendix C.

Direct evidence for slip has been determined by measuring the motion of fluorescent, nanometer-sized tracer particles in solution near a solid surface;[227] however, this technique has a limited slip length resolution of ~10nm. Colloidal probe Atomic Force Microscopy (AFM) and the Surface Forces Apparatus (SFA) can provide a better slip length resolution of ~1nm, but care must be taken to eliminate artifacts that may mask slip behavior. [53,226] In colloidal probe AFM,[71] the AFM cantilever is driven at a constant speed, $v_d$, towards the solid surface. The colloidal sphere at the end of the AFM cantilever approaches at a slower speed, $v$, which depends upon how rapidly the liquid can be squeezed out from between the two surfaces. This changing velocity is dependent upon the solid/liquid BCs through the slip length $b$. The hydrodynamic force experienced by the colloidal sphere is given by

$$F_h = \frac{6\pi\eta r^2 v\psi}{h} \tag{3.1}$$

where $\eta$ is the bulk viscosity, $r$ is the radius of the colloidal probe, $h$ is the separation distance between the colloidal probe and the solid surface, and $v = dh/dt$ is the measured approach velocity of the colloidal probe. For the no-slip BC, the parameter $\psi = 1$. From continuum hydrodynamics, Vinogradova[68] determined a relationship between $\psi$ and the slip length $b$ (V-theory) which is valid for $h << r$, assuming a constant slip length $b$ independent of shear rate. For hydrophobic surfaces

$$\psi = \frac{h}{3b}\left[\left(1+\frac{h}{6b}\right)\ln\left(1+\frac{6b}{h}\right)-1\right]. \tag{3.2}$$

The experimental hydrodynamic force is measured from the bending of the AFM cantilever via Hooke's law, $F_e = kx$, where $k$ is the cantilever spring constant. As illustrated by Cottin-Bizonne *et al.*,[36] eqs. (3.1) and (3.2) can be expanded in the limit of large separations $X = 6b/h << 1$

$$\frac{6\pi\eta r^2 v}{F_h} = h + 2b\,. \tag{3.3}$$

The key feature of this expansion is that the extrapolated experimental data should intercept the h-axis at $h = -2b$ in the absence of any experimental artifacts.

Theory[54,55] and recent experiments[53,226] indicate that for experimentally accessible shear rates ($\dot{\gamma} \sim 10^2 - 10^5\, s^{-1}$), the slip length should be constant and independent of shear rate, as assumed in V-theory; the slip length is expected to only become shear rate dependent[55] at very

high shear rates near the critical shear rate $\dot{\gamma}_c \approx 10^{11} s^{-1}$ (accessible in computer simulations).[28] Experimental measurements[39,52] which exhibit shear rate dependent slip may indicate the presence of either nanobubbles[228,229] or nanoparticles[230] on the surface or may be a result of an incorrect determination of the zero of separation ($h = 0$).[53]

In this work we use colloidal probe AFM[71] to determine the slip length against a molecularly smooth Si wafer for eighteen different liquids from two homologous series; nine n-alkanes and nine n-alcohols. An advantage of this study is that the same colloidal probe and Si surface is used for all liquids. As such, relative changes in slip can be readily compared between liquids and any slip length trends can be attributed to liquid properties (because the solid surfaces remain unchanged).

## 3.3 Experimental Section

In order to study low viscosity liquids, we use large silica colloidal spheres with diameters $2r \sim 55\mu m$ from Mo-Sci. Such large colloidal spheres possess additional advantages: the viscous drag on the cantilever itself[231] is negligible (<1%) compared with the hydrodynamic force and larger separations ($h(max) = 2\mu m$) can be used while still remaining in the regime $h << r$, required by Eq. (3.2). The spheres were UV glued to triangular AFM cantilevers (Veeco NP-S series) with spring constants in the range $k \sim 0.6\text{-}1.3\ N/m$. Both the Si wafer from Silicon Materials Inc. (which possessed a ~2 nm thick amorphous native oxide layer) and attached silica colloidal particle were silanated with a n-hexadecyltrichlorosilane (HTS, Fluka) self-assembled monolayer (SAM) using a cold deposition (10°C) wet chemistry coating procedure[232] performed in a dry box. After coating, the Si wafer and silica sphere had rms surface roughnesses of *0.3 nm* and less than *1 nm,* respectively, as measured over a $1\mu m^2$ area using tapping mode AFM. The Si surface had a uniform hydrophobic silane coating, as indicated by a water contact angle of $107 +/- 0.7^o$, n-dodecane contact angle hysteresis of less than $4^o$, and a critical surface tension of *20.3 +/- 0.02 mN/m* determined from the n-alkane homologous series.[232] The n-alkanes (from n-heptane to n-hexadecane, excluding n-undecane) and n-alcohols (from n-ethanol to n-decanol), a total of eighteen liquids, had a stated purity of 99+% and were used as received from Sigma Aldrich. In order to minimize adsorption of any atmospheric contaminants onto either the colloidal probe or Si wafer substrate, an atmospheric chamber was built between the Asylum 3D MFP head and base. This allows an in-situ purging of both surfaces with 99.999+% purity $N_2$ gas

for 1 minute. With the nitrogen gas turned off, the liquid to be studied was then immediately filled in-situ under this inert gas atmosphere. After each experiment, the AFM colloidal probe/holder and Si wafer were rinsed well and/or sonicated in chloroform, blown dry with $N_2$ gas, and then vacuum dried before the next liquid was studied. The same Si wafer was used in all experiments; each homologous series was studied with two different colloidal probes, to test reproducibility.

The spring constant $k$ is determined in-situ using our most viscous liquid (n-decanol), which has the largest hydrodynamic response and therefore provides the most accurate determination of $k$. More specifically, $k$ is determined from the hydrodynamic bending of the cantilever at large separations ($h \sim 1\text{-}2\mu m$)[87] for n-decanol assuming no slip BCs ($b = 0$) . For our system with small slip lengths $b \sim 10\text{-}30nm$, a no slip BC ($b = 0$) is an excellent approximation at large $h$. With $k$ then fixed, the slip length $b$, which primarily plays a role at small separations, can be determined for any liquid by comparing the experimental hydrodynamic force $F_e \equiv F_e(h)$ with theory ($F_h$, eqs. (3.1) and (3.2)) over an extended separation range ($50nm < h < 2\mu m$). A slow approach (300-500nm/s) was performed prior to each hydrodynamic measurement to calibrate the voltage response of the AFM photodetector and to ensure that no nanobubbles or anomalous charges were present; only a weak van der Waals interaction was observed immediately before hard contact between the two solid surfaces.

## 3.4 Results

Fig. 3.1.A demonstrates the excellent agreement between experimental data (circles) and V-theory with $b = 23.4\ nm$ (solid line) for n-heptanol at a cantilever drive speed $v_d = 40\mu m/s$. The theory is slightly noisy because experimental values for the speed $v$ are used in Eq. (3.1). As the colloidal probe approaches the solid surface, the hydrodynamic force $F_h$ increases from *1.5 nN* to *40 nN* as the separation $h$ decreases from $2\mu m$ to *50 nm*. The effective shear rate $\dot{\gamma}_e = v/h$ (Fig. 3.1.A, dashed line) increases from $20s^{-1}$ at $h = 2\mu m$ to $1000\ s^{-1}$ at $h = 50\ nm$. The absence of systematic deviations in the residuals, $R = F_e - F_h$ (Fig. 3.1.A inset) for separations $50nm < h < 2\mu m$ implies that V-theory is in good agreement with our experimental data for constant $b$ for this separation range. Deviations at small separations ($h < 25nm$) may be due to either a decreasing viscosity (shear thinning) or increasing slip length with decreasing separation, however, further work is required to ascertain the cause for these deviations. Our excellent

agreement with V-theory as well as the fact that the slip length $b$ is independent of $v_d$ to within experimental error (Fig. 3.1.B, inset), provides evidence that $b$ is shear rate independent (at least for $h > 50nm$).

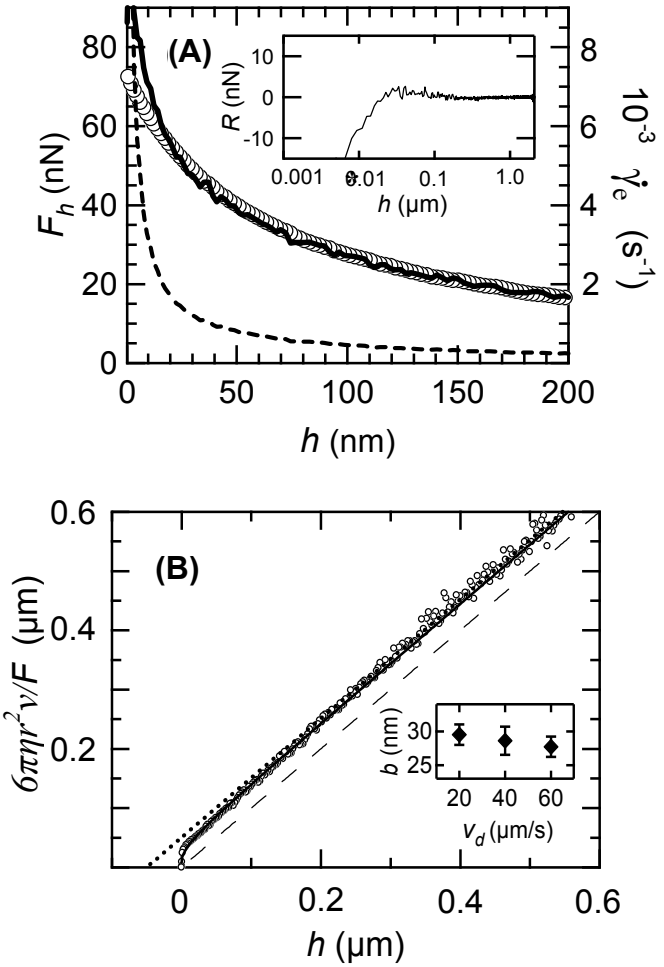


**Fig. 3.1: Experimental hydrodynamic force data and V-theory for n-heptanol.**
**(A) Hydrodynamic force $F_h$ versus separation $h$ for n-heptanol at $v_d = 40\ \mu m/s$; experiment (circles), V-theory for $b = 23.4\ nm$ (solid line), and effective shear rate $\dot{\gamma}_e$ (dashed line). Inset: Hydrodynamic force residuals $R = F_e - F_h$ for n-heptanol. (B) Expansion representation (Eq. (3.3)) of n-heptanol data from (B); experiment (circles), V-theory for $b = 23.4\ nm$ (thin solid line), experimental no-slip BC (dashed line), and extrapolation of experimental data for $h >> b$ (dotted line). Inset: $b$ as a function of $v_d$ for n-heptanol.**

Fig. 3.1.B replots the data in Fig. 3.1.A using the representation in Eq. (3.3). The slope of the dotted line is $1.005 \pm 0.005$, which implies that $\eta$ and $r$ are accurately determined. As determined from the intercept, the slip length is $b = 25.1nm$, which agrees well with the value of $b = 23.4nm$ determined in Fig. 3.1.A. The viscosity $\eta$, was determined for the actual

experimental temperature.[233] Our preference is to use Eqs. (3.1) and (3.2) to determine *b,* as Eq. (3.3) is more susceptible to errors originating from extrapolating data over large distances. In the remainder of this publication, we discuss the slip length results obtained for the n-alkanes and n-alcohols at large separations ($h > 50nm$) where V-theory provides an excellent description of experimental data.

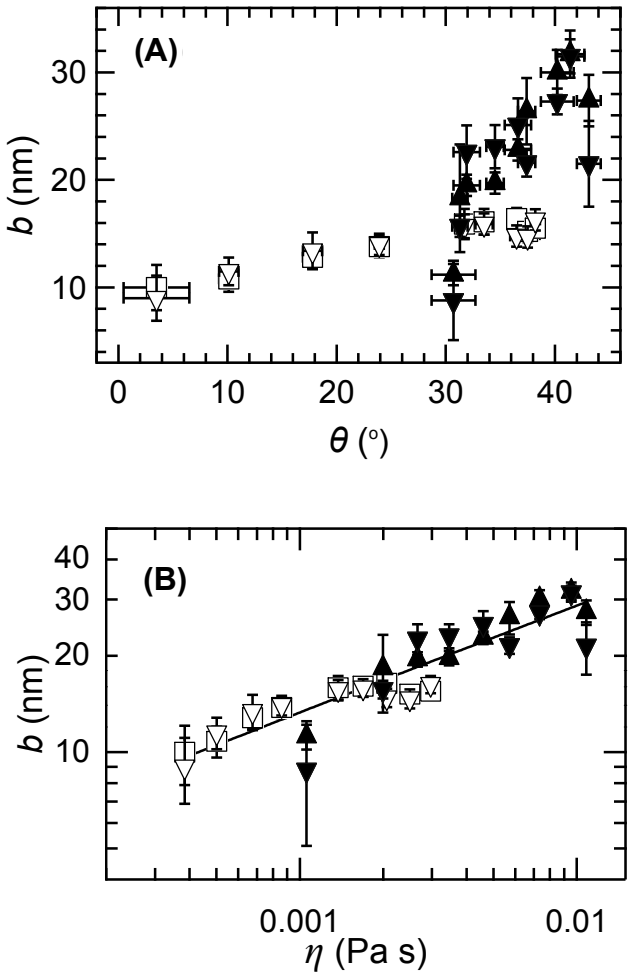


**Fig. 3.2: Slip length *b* vs. contact angle $\theta$ and bulk viscosity $\eta$ for the alkanes & alcohols. (A) Slip length *b* versus contact angle $\theta$ for the n-alkanes (open symbols) and n-alcohols (solid symbols). (B) Slip length *b* versus bulk viscosity $\eta$ on a log-log plot for the n-alkanes (open symbols) and n-alcohols (solid symbols). The solid line is a fit to the data, as described in the text. Spring constants for the 3 AFM cantilevers: inverted triangles (open and solid), *k = 1.26 N/m*; triangles, *k = 1.31 N/m*; squares, *k = 0.63 N/m*.**

## 3.5 Discussion

Both theory and computer simulations have suggested a number of causes for slip on molecularly smooth solid surfaces. If one cause dominates the others, then it should show up as a correlation in the experimental data. Three potential slip mechanisms are discussed below. (i) If the commensurability/incommensurability of the liquid for the solid surface structure[46,234] principally determined the slip behavior, this would imply that similarly sized molecules (eg. n-octane and n-octanol) should exhibit similar slip lengths. Fig. 3.2 indicates that these two liquids do not exhibit similar slip lengths. (ii) Theory suggests that the slip length $b$ should monotonically increase with increasing contact angle $\theta$.[34,35] In our work, no correlation is found between the n-alkane and n-alcohol slip length data sets when plotted as a function of contact angle (Fig. 3.2.A). Hence, the slip length is not predominantly determined by the wettability of the liquid for the solid substrate for these liquids. The slip length $b$ error bars in Fig. 3.2 represent either the experimental uncertainty from a minimum of 6 experiments or an uncertainty of 1 nm originating from our estimated zero in separation error,[235] which ever is larger. (iii) Theory suggests that $b$ should increase linearly with viscosity $\eta$ for homologous series of liquids against a structureless atomically smooth solid surface.[54,55,236] In contrast to this prediction, we find an excellent correlation between data sets (Fig. 3.2.B) for $b = A\eta^x$ with amplitude $A = 130 \pm 60$ nm/(Pa s)$^x$ and exponent $x = 0.33 \pm 0.17$. An element that is missing from most theories and computer simulations is the influence of the n-alkylsilane brush on the slip behavior. The presence of this brush on both the Si surface and colloidal probe will alter how momentum is transferred from the liquid to the solid, which in turn will influence the slip behavior.[54]

Theory suggests that similar slip behavior should be observed for both polymeric and non-polymeric liquid.[55] Fetzer *et al.*[237] observed very large shear independent slip lengths while studying the dewetting dynamics of polystyrene (PS) films on n-alkylsilane coated Si wafers. In their study short polymer chain lengths, below the entanglement length,[238]were used; hence, these polymers are expected to behave like simple Newtonian liquids in these dewetting studies. Our measurements are qualitatively consistent with the very large shear independent slip lengths observed by Fetzer *et al*. The viscosities ($\eta \sim 10^4 - 10^7$ Pa s) and slip lengths ($b \sim 100$-$10{,}000$nm) were many orders of magnitude larger than the corresponding quantities studied here.

For an n-dodecyltrichlorosilane (C12) coating, they found $b \sim \eta^x$ with $x \sim 0.5$; for an n-octadecyltrichlorosilane (C18) coating, the exponent showed almost zero slope ($x \sim 0$) at small viscosities which increased to a larger slope ($x \sim 0.33$) at large viscosities. Our measured exponent $x \sim 0.33$ for a n-hexadecyltrichlorosilane (C16) coating is approximately consistent with their polymer results, however, the amplitude $A$ observed here is a factor of ~10 larger than in the polymer experiments.

Cottin-Bizonne *et al.*[226] and Honig and Ducker[53] have recently reported shear independent slip lengths. The experimental results[53,226] and those reported here are inconsistent with each other. The shear rate independence of $b$ and the agreement with V-theory are indicative that each of these experiments provide a valid measure of the slip. We postulate that the differences in the slip behavior could be due to differences either in the sample surfaces or sample environment.

Honig and Ducker[53] use a colloidal probe AFM incorporating a novel evanescent wave detector to determine the zero of separation. They study slip in sucrose solutions and polydisperse poly-dimethylsiloxane (PDMS) against various hydrophilic ($\theta < 5^o, 20^o$) and hydrophobic ($\theta \sim 40, 90^o$) surfaces.[239] In all cases, their results were described by a no slip BC ($b = 0$). For binary liquid mixtures and polydisperse systems preferential adsorption may alter the slip behavior. Honig and Ducker report a relatively large contact angle hysteresis of $\Delta\theta \sim 15\text{-}20^o$.[239] Contact angle hysteresis is generally associated with physical or chemical roughness,[240] hence, their surfaces may be more chemically heterogeneous than our surfaces. These differences might explain their no slip observations.

Cottin-Bizonne *et al.* use an accurate custom-designed dynamic SFA to determine slip behavior.[36,226] They examine water-glycerol mixtures against Pyrex and octadecyltrichlorosilane (OTS) coated Pyrex.[36] They do not find the systematic variation with viscosity that we report here; preferential adsorption effects in the binary mixture may be responsible for these differences. For dodecane and water against various solid surfaces, they report a strong divergence in the slip length for $\theta > 90^o$ where all reported slip lengths have $b < 20\ nm$.[36] In particular, for dodecane against OTS-Pyrex ($\theta = 28^o$), they report a slip length $b \sim 2\ nm$, which is smaller than the value reported here ($b \sim 15nm$). All of our measurements are for liquids with contact angle $\theta < 45^o$, therefore our experiments are not necessarily inconsistent with a wettability driven slip length at higher contact angles of $\theta \sim 90^o$. The difference in slip

magnitude for dodecane may be due to one of the following: differences in silane chain length, differences in silane preparation, and/or our use of an environmental chamber where filling is done under $N_2$ gas. It has been shown in the past that differences in the silane deposition temperature can significantly alter the surface properties of n-alkylsilane coatings.[232] Also, our use of an environmental chamber minimizes contamination of the solid surfaces by atmospheric vapors.

## 3.6 Summary and Conclusions

In summary, we have used colloidal probe AFM to determine the slip behavior for the n-alkane and n-alcohol homologous series against a hydrophobic n-hexadecyltrichlorosilane coated Si wafer. The slip lengths for these liquids, obtained for separations $h > 50nm$, were shear rate independent where the hydrodynamic force quantitatively agreed with a theory by Vinogradova.[68] As the same colloidal probe and same Si wafer surface were used in studying all of these liquids trends in the slip length can be attributed to changes in liquid properties. We find that the slip length $b$ is predominantly a function of the bulk viscosity $\eta$ where $b = A\eta^x$ with $A \sim 130nm/(Pa\ s)^x$ and $x \sim 0.33$. These results are similar to recent dewetting experiments[237] of polystyrene films on an n-alkylsilane coated Si wafer where the exponent $x$ is a function of the grafted n-alkylsilane SAM chain length. A SAM chain length dependence of the micro-scale friction coefficient has been observed using friction force microscopy[241] and dynamic contact angle measurements.[242] A theoretical understanding of the interconnection between grafted layers, friction and slip[243,244] will be required before these disparate experimental observations can be interconnected. Future work with pure liquids on varying n-alkylsilane coated surfaces is needed to further understand the dependence of slip on viscosity.

## 3.7 Acknowledgments

The authors thank Dr J.–H. Cho for assistance with the Igor Pro programming and Drs. N. V. Priezjev and J.-L. Barrat for discussions. This research was supported by the National Science Foundation under grant DMR-0603144.

# Chapter 4 - Improved In-Situ Spring Constant Calibration for Colloidal Probe Atomic Force Microscopy[§]

## 4.1 Overview of Colloidal Probe AFM and Cantilever Spring Constant

In colloidal probe atomic force microscopy (AFM) surface forces cannot be measured without an accurate determination of the cantilever spring constant. The effective spring constant $k$ depends upon the cantilever geometry and therefore should be measured in-situ; additionally, $k$ may be coupled to other measurement parameters. For example, colloidal probe AFM is frequently used to measure the slip length $b$ at solid/liquid boundaries by comparing the measured hydrodynamic force with Vinogradova slip theory (V-theory). However, in this measurement $k$ and $b$ are coupled, hence, $b$ cannot be accurately determined without knowing $k$ to high precision. In this Chapter, a new in-situ spring constant calibration method based upon the residuals, namely, the difference between experimental force-distance data and V-theory is presented and contrasted with two other popular spring constant determination methods. In this residuals calibration method, V-theory is fitted to the experimental force-distance data for a range of systematically varied spring constants where the only adjustable parameter in V-theory is the slip length $b$. The optimal spring constant $k$ is that value where the residuals are symmetrically displaced about zero for all colloidal probe separations. This residual spring constant calibration method is demonstrated by studying three different liquids (n-decanol, n-hexadecane, and n-octane) and two different silane coated colloidal probe-silicon wafer systems (n-hexadecyltrichlorosilane and n-dodecyltrichlorosilane).

## 4.2 Introduction

Since its first application by Ducker *et al*.[71,245] and Butt *et al*.[246] to measure colloidal, electrostatic, van der Waals, and hydration forces in electrolyte solutions, colloidal probe atomic force microscopy (AFM) has become an extremely popular technique for measuring forces. Colloidal probe AFM is capable of measuring small interaction forces, such as those associated

---

[§] Reprinted with permission from Sean P. McBride and Bruce M. Law, Review of Scientific Instruments, 81, 113703, (2010). © 2010 American Institute of Physics. Improved In-Situ Spring Constant Calibration for Colloidal Probe Atomic Force Microscopy by Sean P. McBride and Bruce M. Law. Proof of permission granted found in Appendix C.

with ion pairing,[247] molecular recognition of DNA–protein and enzyme–substrate reactions,[248] the Casimir effect,[249,250] adhesion,[251-254] and hydrodynamic drainage forces at solid-fluid interfaces.[1,47,48,51-53,56,65,87,239,255-259] Extensive reviews on AFM force measurements[260-262] highlight additional details and experiments performed with colloidal probe AFM.

In colloidal probe and non-colloidal probe AFM measurements,[78,79] assessing the spring constant $k$ is the primary limiting factor in determining the accuracy of the force measurement. Early force experiments[71,245,246] relied on either using the often incorrect spring constants provided by the manufacturer, the parallel beam approximation for V-shaped cantilevers,[263,264] and/or spring constant equations containing only a single elastic modulus,[263,264] whereas most AFM cantilevers are composites of many different materials (e.g. base material, chromium, and gold) of differing thicknesses. Early work by Butt *et al*.[265] demonstrated a unique experimental method for determining $k$ for V-shaped cantilevers which showed that $k$ differed from the parallel beam approximation used for V-shaped cantilevers; this technique demonstrated that $k$ for V-shaped non-colloidal cantilevers needed to be determined experimentally. Simultaneous independent efforts for V-shaped and beam cantilevers have lead to the popular Cleveland method,[80] thermal noise method,[81] and Sader methods.[82-85] Lévy and Maaloum[266] demonstrated excellent agreement between the thermal noise and Sader methods for non-colloidal rectangular cantilevers in air and highlighted some disagreements found in other non-colloidal V-shaped cantilever calibration methods.[167] Cook *et al*.[267] found that the thermal noise and Sader methods for non-colloidal rectangular cantilevers in air agreed to within ~ 4% over a wide range of cantilevers.

The cantilevers in most commercial AFMs are mounted at an angle,[267-269] and this tilt angle can result in an increase in the effective $k$ by 10-20%.[252,253] Edwards *et al*.[86] recently demonstrated that in addition to the tilt angle, the position of a colloidal probe placed at the end of the cantilever plays an important role in the inverse optical lever sensitivity (InvOLS)[160] and spring constant calibrations. In most AFMs the deflection of the cantilever is sensed by measuring the voltage sum signal reflected from the end of the cantilever on a position sensitive detector (PSD); this InvOLS process calibrates the PSD and encodes this voltage to deflection conversion (Appendix 4.A). The work of Edwards *et al*. suggests that both the spring constant $k$ and InvOLS calibrations should be conducted in the actual experimental configuration in order to correctly account for any tilts and induced torques associated with the colloidal probe. Craig and

Neto[87] have developed a method that enables *k* to be calibrated in-situ for colloidal probes; this method effectively accounts for these tilts and torques due to the placement of the colloidal probe. This method requires using a viscous liquid possessing a zero slip length as a calibration fluid; however, it is often difficult to determine a priori if a particular liquid/solid combination possesses zero slip length. A very similar in-situ calibration for colloidal probes was hypothesized earlier by Senden and Ducker.[270]

Following the work of Edwards *et al*.,[86] in-situ *k* calibration of large colloidal probes for hydrodynamic force measurements implies that the probes must be immersed in viscous liquids where the viscosity can easily exceed that of water by a factor of ten or greater. Current non-colloidal probe *k* calibration methods all have the same inherent problem when applied to colloidal probes conducted in this type of environment; they rely on the quality factor Q of the cantilever, which describes the sharpness of the resonant frequency peak of the cantilever, $f_R$. As has been previously shown even for non-colloidal probes, water drastically damps the oscillating cantilever, effectively lowering Q to the order of unity[271] and making the shape of the resonance peak less well defined.[272] For large colloidal probes in viscous liquids, the system is further damped ($Q << 1$) and the resonance peak becomes ill defined. Walters *et al*.[272] found that the thermal method in air and water for non-colloidal rectangular cantilevers agreed to within ±11% and ±20% for the Cleveland method. Later, Burnham *et al*.[269] compared the Cleveland, thermal noise, and Sader methods in both air and water environments for rectangular and V-shaped non-colloidal probes. Burnham *et al*. found the use of the Cleveland method inappropriate in a water environment, the Sader method determination of *k* ranged from 15-40% lower in air than in water, and that the thermal method displayed differences as high as 60% depending upon the surrounding environment and shape of the cantilever.

In summary, different methods for determining the spring constant *k* of the AFM cantilever will depend upon the sample environment (e.g. air or liquid) and the cantilever geometry (e.g. rectangular versus V-shaped cantilevers, cantilever tilt, colloidal probe positioning). These factors can lead to differences in the spring constant *k* of up to 60%; thus, directly influencing how accurately a particular quantity can be measured using AFM. It is therefore clear that the spring constant *k* should be determined in-situ in precisely the geometry that will be used for the actual AFM experiments. Any variations in the experimental geometry will require a recalibration of the spring constant *k*.

In this Chapter, an experimental in-situ calibration of the spring constant for large colloidal probes is demonstrated by adjusting *k* between experimental estimates until the residuals, exhibit minimal systematic deviation as a function of separation *h*. The residuals are defined as the difference between the experimental force-distance data and Vinogradova's[68] slip theory (V-theory). The experimental lower and upper estimates of *k* for the colloidal probes used in this study were determined by (i) the standard thermal noise method performed in air using the default InvOLS correction factor of $\chi = 1.09$,[272-275] (see Appendix 4.B for details on this correction factor and improvements to the thermal noise method) and (ii) a method similar to the Craig and Neto in-situ method[87] but conducted in a liquid of finite slip length. The residuals calibration is performed with decanol and two different silane coated surfaces to test reproducibility. Perfect agreement between experiment and V-theory would be indicated by the residuals being symmetrically displaced about zero as a function of separation. A plot of the residuals as a function of separation provides both a graphical and a numerical indicator ($\chi^2$, the sum of the squares of the residuals) from which the correct *k* value representing the system can be determined. With this *k* value fixed, the slip length for any liquid can then be determined, provided that the cantilever geometry remains unaltered.

In an effort to remain focused on the residuals calibration method, the reader is referred to comprehensive review articles[27-30] that describe the many models, mechanisms, and measurements relating to slip and no-slip boundary conditions. This article is organized as follows. Characteristics of the surfaces used in the experiment are first given. This is followed by a brief description of the experimental set-up and basic principles of colloidal probe atomic force microscopy. The foundation and results of the residuals spring constant calibration method are established in the main body of the Chapter. Important technical details, such as colloidal probe calibration, thermal noise method improvements, surface preparation, and cantilever drag analysis (required for a reader to reproduce the results) can be found in the appendices.

## 4.3 Experimental Section

V-shaped silicon nitride AFM cantilevers (NP-S series), with a quoted spring constant range of 0.06-0.58 N/m, were purchased from Veeco.[276] n-Hexadecyltrichlorosilane (HTS) from Fluka and n-dodecyltrichlorosilane (DTS) from Gelest were used as received with no further purification. n-Hexadecane (anhydrous, 99+%) and n-octane (98%) were purchased from Sigma

Aldrich and used as received with no further purification. The silicon substrates with 1-10 Ω-cm resistivity and <100> orientation were purchased from Silicon Materials Inc. The ~55μm diameter borosilicate glass spheres, used as colloidal probes, were purchased from MO-SCI Specialty Products, L.L.C. All water used in this experiment was first purified by a custom reverse osmosis de-ionization system built by Siemens and then by a Millipore Academic A10 water purification system, which provided 18.2 MΩ cm resistivity at 25°C. Unless otherwise specified, all other liquids in the experiment had a purity ≥ 99.5% and were used as received from the respective manufacturers. All nitrogen drying, in the preparation steps as well as in experiments, was performed with ultra high purity dry nitrogen (99.999+%).

The attachment process of the colloidal probe to the AFM cantilever as well as the silanization process of both the colloidal probe and silicon wafer are described in Appendix 4.C. Table 4.1 summarizes the surface characteristics of both the HTS and DTS silanized systems.

**Table 4.1: Silicon wafer and colloidal probe surface characteristics.**

| | RMS | p-p max. | Area | Octane | | Hexadecane | | Decanol | | $H_2O$ | |
|---|---|---|---|---|---|---|---|---|---|---|---|
| | (nm) | (nm) | ($\mu m^2$) | $\theta_{adv}$ | $\theta_{rec}$ | $\theta_{adv}$ | $\theta_{rec}$ | $\theta_{adv}$ | $\theta_{rec}$ | $\theta_{adv}$ | $\theta_{rec}$ |
| **HTS silicon** | 0.22 | 3.2 | 5x5 | 12 | 10 | 40 | 37 | 45 | 40 | 110 | 104 |
| **DTS silicon** | 0.16 | 2.5 | 5x5 | 11 | 8 | 40 | 37 | 47 | 42 | 111 | 104 |
| **HTS probe** | 0.86 | 10.1 | 2x2 | - | - | - | - | - | - | - | - |
| **DTS probe** | 0.98 | 31.4 | 2x2 | - | - | - | - | - | - | - | - |

The root mean squared surface roughness value (RMS) and peak-peak (p-p) asperity values are given on all surfaces; (5x5)$\mu m^2$ and (2x2)$\mu m^2$ AC mode images were used to acquire RMS measurements for the silane coated silicon substrates and colloidal probes, respectively. RMS and asperities measurements for silicon substrates are averaged over three random spots on each silicon substrate. The RMS measurement for the colloidal probes, at the point of contact (±0.5μm), was determined by mounting the cantilever on a custom holder that compensated for the 11° cantilever holder tilt. Fig. 4.1 shows an AC mode image of the HTS colloidal probe at the point of contact with the silicon substrate. Advancing and receding contact angle measurements (Table 4.1) were made by increasing and decreasing the volume of water (octane, hexadecane, and decanol) on the silane coated silicon wafer using a Kent Scientific Genie Plus syringe pump. A long range microscope (First Ten Angstroms 100 Series) was used to record the images and determine the contact angles with an estimated accuracy of ± 1°. Contact angle measurements

were made by averaging three dynamic sessile drop experiments in similar droplet volume regimes. The difference between advancing and receding contact angles provides a measure of the chemical and physical homogeneity of the samples.[223] Contact angles on the colloidal probes were assumed to be similar to the flat silicon wafer values, however, they could be systematically lower by as much as ~10°.[277] Table 4.1 demonstrates that the HTS probe is far superior to the DTS probe, based upon the height of the asperities. The diameters of the colloidal probes used in the experiments were measured with estimated error of ~2% using a Lecia inverted optical microscope (DM IRM) with a 63X water immersion lens (resolution: 0.14μm per pixel). For comparison, the local radius of curvature[278] of the colloidal probes was determined from the (2x2)$\mu m^2$ AFM scan and differed from the optical determination by less than 5% for both the DTS and HTS colloidal probes.

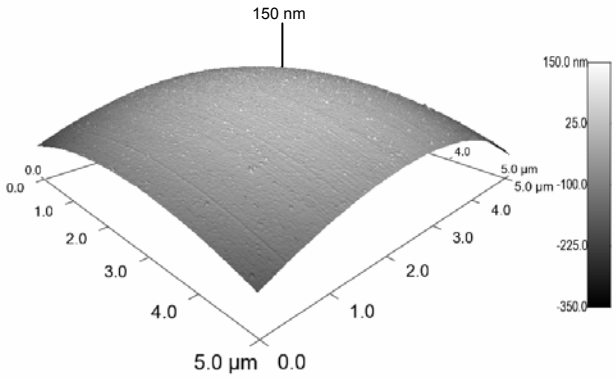


**Fig. 4.1: AC mode image of the HTS colloidal probe at the point of contact.**

An atmospheric chamber has been integrated into the base of the Asylum Research MFP-3D AFM to minimize adsorption of any atmospheric contaminates/moisture onto the sample surfaces immediately prior to an experiment. The chamber has a built in humidity sensor (La Crosse Technology model WS-7220U-IT) and temperature probe (Yellow Springs Instruments 44034 precision thermistor) which accurately measures the temperature to within ±0.1°C (which is important because the liquid viscosities are sensitive to temperature[233]). Operation of the atmospheric chamber for each experiment is described in previous work.[1] Prior to purging the atmospheric chamber with nitrogen, both surfaces in all experiments are exposed to a 500 microcurie polonium 210 source (NRD L.L.C. Model 3C500) which effectively neutralizes any

static charges. n-Decanol (~11.2 mPa s at 25°C) was chosen as the calibration liquid because it produces a large deflection of the cantilever. As described in detail in Appendix 4.A, before each hydrodynamic force measurement, a slow approach at a drive velocity of 500nm/s was performed in order to calibrate the inverse optical lever sensitivity (InvOLS),[160] eliminate any *virtual deflection*,[239,258] and ensure that no residual charges were present on either surface. The combined 15 slow InvOLS approach runs prior to the fast runs for each colloidal probe showed very little deviation with average InvOLS values of (48.5±0.4)nm/V and (31.4±0.1)nm/V for HTS and DTS probes respectively (each slow approach was performed on different spots on the silicon substrate). Unless otherwise specified, all hydrodynamic force measurements were performed in an open loop configuration at a drive velocity of ~ 40μm/s with zero dwell time on the surface.

As the colloidal probe approaches the silicon wafer surface during an experiment, the linear variable displacement transducer (LVDT) of the AFM provides information about the piezoelectric displacement $z$ of the base cantilever at each time interval. At each time interval the AFM also measures the total colloidal probe deflection $x$ determined from the output voltage of the position sensitive detector (Appendix 4.A). The separation $h$ between the colloidal probe apex and the silicon substrate is given by the sum of the LVDT signal and deflection $x$ ($h = z + x$). The velocity of the colloidal probe ($dh/dt$), which differs from the drive velocity of the cantilever ($dz/dt$),[279] is obtained by differentiating the probe separation $h$ with respect to time.

## 4.4 Analysis Section

A variety of forces contribute to the total force that acts on the colloidal probe; these forces include the hydrodynamic drag on the sphere ($F_h$), the hydrodynamic drag on the cantilever ($F_{cant}$), and surface forces between the sphere and substrate ($F_{surf}$), i.e. electrostatic interactions etc. For surface separations $h \geq 10nm$, provided that both the colloidal probe and the surface are uncharged, $F_{surf}$ is negligible compared with $F_h$ and will be neglected for the remainder of this discussion. The total experimental force on the colloidal probe is given as

$$F_e = kx = k\left(x_h + x_{cant}\right), \tag{4.1}$$

where $x$ is the total cantilever deflection measured by the AFM. The deflection due to the hydrodynamic drag on the sphere (cantilever) is given by $x_h$ ($x_{cant}$). The cantilever contribution, $F_{cant} = kx_{cant}$ which is included in Eq. (4.1) only makes a small constant contribution to the total

force as determined experimentally in Appendix 4.D ($F_{cant}$ ~1nN for decanol). The experimental hydrodynamic force due to the sphere, $F_e - F_{cant}$, can be compared with theory where

$$F_h = \frac{6\pi\eta r^2 v\psi}{h}, \tag{4.2}$$

$\eta$ is the bulk viscosity, $r$ is the radius of the sphere, $h$ is the separation distance between the sphere and the solid surface, and $v = dh/dt$ is the approach/withdraw velocity of the sphere. From continuum hydrodynamics, Vinogradova[68] (V-theory) determined a relationship between $\psi$ and the slip length $b$, which is valid for $h<<r$, assuming the slip length $b$ is independent of shear rate. For $b \neq 0$,

$$\psi = \frac{h}{3b}\left[\left(1+\frac{h}{6b}\right)\ln\left(1+\frac{6b}{h}\right)-1\right]. \tag{4.3}$$

As $b$ approaches the no-slip boundary condition ($b \rightarrow 0$), the parameter $\psi \rightarrow 1$. According to Eqs. (4.1) and (4.2), the residuals are defined as

$$R = kx_h - \frac{6\pi\eta r^2 v\psi}{h}, \tag{4.4}$$

which provides a measure of how well V-theory describes the experimental hydrodynamic force data. For perfect agreement between theory and experiment, the residuals $R$ would be symmetrically displaced around zero when plotted as a function of separation $h$. Any systematic deviations of $R$ from zero would imply that the two fitting parameters $k$ and $b$ that appear in Eqs. (4.3) and (4.4) are in error, or, the assumptions behind V-theory are incorrect. The residuals $R$ therefore allow for a quantitative comparison of different spring constant determination methods. A popular method for determining the spring constant of cantilevers is the thermal noise method.[81] This method is typically performed with non-colloidal cantilevers in air with the default InvOLS correction factor of $\chi = 1.09$[272-275] (see Appendix 4.B for details). This method allows for the determination of the spring constant $k_{therm}$ by fitting the power spectrum of the cantilever thermal noise to a simple harmonic oscillator response with added white noise. It is a quick and simple process to determine $k_{therm}$ using the default thermal noise model via the user interface provided with the Asylum Research 3D MFP AFM. If this value of $k = k_{therm}$ (calibrated in air) is used in Eq. (4.4) then the only free parameter with which to improve the agreement between experimental data and V-theory is the slip length $b$. Table 4.2 lists $k_{therm}$ and the best fit values of the slip length $b$ from six trials for the two different types of silane coatings

(HTS and DTS) on the colloidal probe and Si wafer surface. Fig. 4.2.A (lower curve) shows a plot of the residuals *R* as a function of separation *h* for this thermal noise determination of the spring constant. *R* exhibits systematic deviations below zero, implying that the actual value for *k* representing our system is greater than $k_{therm}$. There are corrections to $k_{therm}$ which account for the cantilever tilt and torque (Appendix 4.B) however these corrections only marginally improve the residuals.

**Table 4.2: Summary of spring constants and slip lengths at ~ 40 μm/s cantilever velocity.**

| | | $k_{Thermal}$ Decanol | $k_{In\text{-}situ}$ Decanol | $k_{Residuals}$ Decanol | $k_{Residuals}$ Hexadecane | $k_{Residuals}$ Octane |
|---|---|---|---|---|---|---|
| **HTS** | ***k*** (N/m) | 0.95 ± 0.08 | 1.38 ± 0.03 | 1.23 ± 0.01 | 1.23 | 1.23 |
| | **Slip** (nm) | 29.3 ± 1.7 | 11.7 ± 0.9 | 15.7 ± 1.1 | 20.4 ± 0.3 | 17.4 ± 0.5 |
| **DTS** | ***k*** (N/m) | 0.88 ± 0.10 | 1.31 ± 0.01 | 1.20 ± 0.01 | 1.20 | 1.20 |
| | **Slip** (nm) | 30.8 ± 0.7 | 11.4 ± 0.5 | 14.3 ± 0.5 | 14.3 ± 0.2 | 9.8 ± 1.8 |

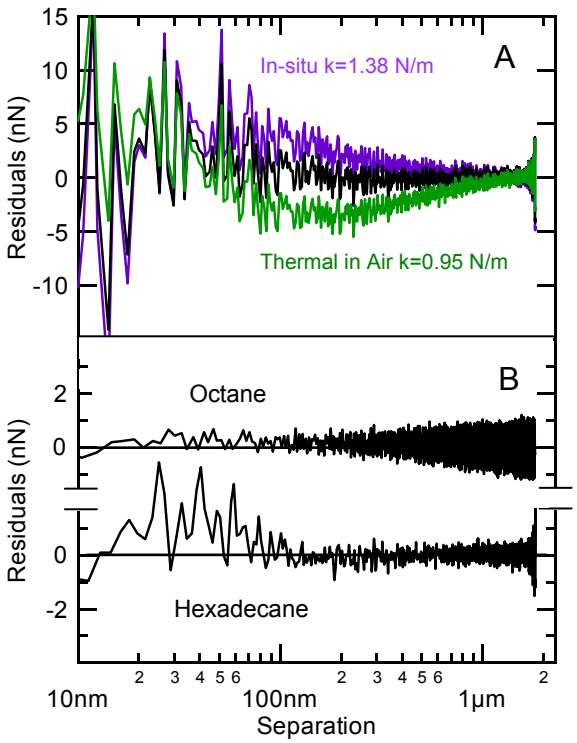


**Fig. 4.2: Residuals as a function of separation for decanol, octane, and hexadecane. (A) Residuals from fitting V-theory to run 5 in decanol using the HTS system; in-situ (upper line), residuals kres =1.23 N/m (middle), and thermal (k calibrated in air) (lower). (B) Residuals for octane (b = 17.1nm) and hexadecane (b = 20.3nm) using fixed kres =1.23 N/m for HTS system.**

An alternative method for estimating the spring constant $k$ is the in-situ method developed by Craig and Neto.[87] This method assumes no slip boundary conditions (i.e. $b = 0$ nm and $\psi = 1$) are valid at the solid-liquid interface. Therefore, according to Eqs. (4.1) and (4.2) if the viscosity and radius of the sphere are known, the "in-situ spring constant," $k_{in\text{-}situ}$, can be determined from the slope of a plot of the normalized deflection $x_{norm}$ (= $x/v$) versus the inverse separation $h^{-1}$

$$\frac{x}{v} = \frac{6\pi\eta r^2}{k_{in-situ}}\left(\frac{1}{h}\right). \tag{4.5}$$

For our system, this $k_{in\text{-}situ}$ method is only used as an approximation since it was originally intended to be performed in a liquid with no slip. As such, the protocol developed by Craig and Neto was followed with the exception that we only use the data far from the surface where the slip length contributes little to the reduction of the hydrodynamic force and the plot of $x_{norm}$ versus $h^{-1}$ remains linear. If this value of $k = k_{in\text{-}situ}$ (conducted in decanol) is used in Eq. (4.4) then the only free parameter with which to improve the agreement between experimental data and V-theory is the slip length $b$. Table 4.2 lists $k_{in\text{-}situ}$ and the best fit values of the slip length $b$ from six trials for the two different types of silane coatings (HTS and DTS) on the colloidal probe and Si wafer surface. Fig. 4.2.A (upper curve) shows a plot of the residuals $R$ as a function of separation $h$ for this in-situ determination of the spring constant. $R$ exhibits systematic deviations above zero which implies that the actual value for $k$ representing our system is less than $k_{in\text{-}situ}$.

As is evident from Fig. 4.2.A the actual spring constant representing our system must lie between $k_{therm}$ and $k_{in\text{-}situ}$. In the "residual method" for determining the optimal spring constant $k_{res,}$ the chi-squared given by the sum of the squares of the residuals at each separation $h$, or

$$\chi^2 = \sum_i \left[R_i(h)\right]^2 \tag{4.6}$$

is used. $k_{res}$ will possess the lowest $\chi^2$ where graphically $R$ is distributed symmetrically about zero as a function of separation $h$. In practice, the spring constant is systematically adjusted between the experimental estimates $k_{therm}$ and $k_{in\text{-}situ}$ in 0.01 N/m increments. At each $k$ value, the hydrodynamic drag from the cantilever is determined (Appendix 4.D), the best fit slip length $b$ is determined for all separations $h \geq 10$nm, and $\chi^2$ is calculated for separations $h \geq 100$nm. This

optimal $k_{res}$ value is listed in Table 4.2 along with its best fit slip length; $k_{res}$ possesses the lowest $\chi^2$ value and exhibits minimal systematic deviations in the residuals as a function of separation (Fig. 4.2.A, horizontal curve). The same deflection data used to determine $k_{in\text{-}situ}$ in decanol is used to determine $k_{res}$. In order to confirm that $k_{res}$ is the actual spring constant representative of our system, slip measurements for two other liquids, n-hexadecane and n-octane were conducted with $k_{res}$ fixed at 1.23 N/m (HTS system); these liquids possess viscosities of 3.0 mPa s and 0.5 mPa s at 25°C, respectively, (whereas $\eta = 11.2$ mPa s for n-decanol). In these experiments it is important that the geometry of the cantilever remain unchanged. For these liquids the only adjustable parameter is the slip length *b*; indeed the residuals are symmetrically displaced around zero for both liquids (Fig. 4.2.B) which is further evidence that the residual method determines the actual cantilever spring constant.

V-theory assumes that the slip length is constant and independent of the shear rate. This assumption is expected to be valid below a critical shear rate of $\dot{\gamma}_c \sim 10^{10} s^{-1}$ as determined from Molecular Dynamics simulations.[27] While our experimental shear rates $\dot{\gamma} \sim v/h < 10^4 s^{-1}$ are well below $\dot{\gamma}_c$, nevertheless it is important to check this assumption experimentally. Multiple experiments were conducted at cantilever drive velocities of 10, 20, and 30μm/s and no shear rate dependence of the slip length was observed in either the HTS or DTS systems. The average slip length *b* for n-decanol (with $k_{res}$ fixed) was (16 ± 1)nm and (14 ± 1)nm for HTS and DTS, respectively (measurements averaged over 15 different runs).

Honig and Ducker[53,239,258] use an alternative method to verify the shear rate independence of the slip length. As demonstrated by Cottin-Bizonne *et al.*[36,226] Eqs. (4.1-4.3) can be expanded in the limit of large separations for $6b/h << 1$

$$\frac{6\pi\eta r^2 v}{k x_h} = h + 2b \,. \tag{4.7}$$

A plot of the left hand side of Eq. (4.7) versus separation *h,* using $k = k_{res}$, should be linear (for large $h >> 6b$) with a slope of 1 and an h-intercept at $h = -2b$, provided (i) the slip length is shear rate independent, (ii) the cantilever drag is correctly determined, and (iii) the radius and viscosity are accurately known. Fig. 4.3 shows an analysis of n-decanol run 5 for the HTS system using this approach. Fig. 4.3.A shows the approach/withdrawal force data where the inset (for approach) demonstrates that hard contact was made between the sphere and the surface at zero

separation. The approach/withdrawal velocities (Fig. 4.3.B), calculated from Fig. 4.3.A ($v = dh/dt$), are quite different and are not constant. Despite this large variation in velocity, a plot based upon Eq. (4.7) is linear for both approach and withdrawal where both data sets collapse onto a single line with no oscillations as shown in Fig. 4.3.C.

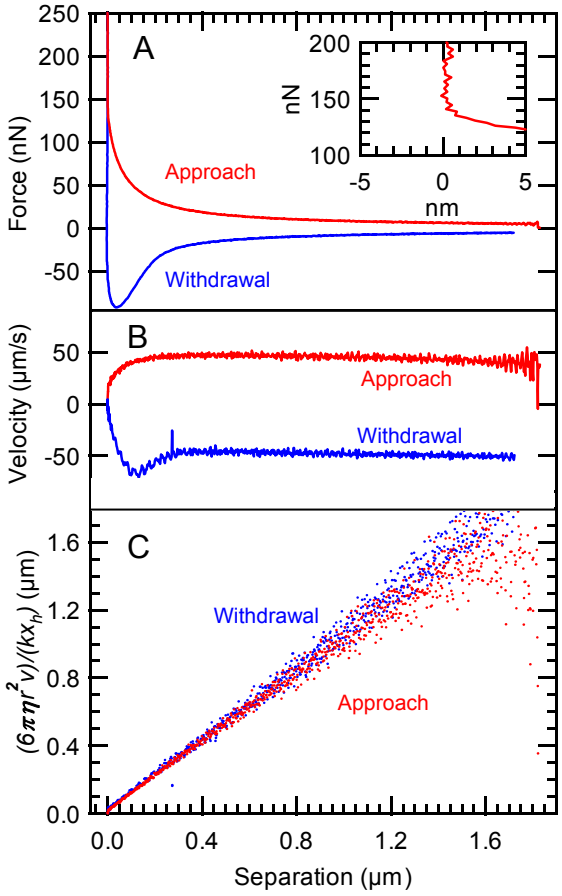


**Fig. 4.3: Force (A), velocity (B), and expansion representation (C, Eq. (4.7)) for decanol run 5 HTS system. Inset A demonstrates that hard contact was made on approach at zero separation.**

By fitting the separation data in Fig. 4.3.C between 200nm and 1μm for the HTS system, slopes of 0.99 and 1.04 were obtained for approach and withdrawal (similar slopes were obtained for the DTS system). All of the slopes are very close to unity; the approach data is in slightly better agreement with Eq. (4.7) than the withdrawal data, most likely due to the fact that only the approach InvOLS was used to calibrate the system. The slip length can also be extracted from Eq. (4.7) by extrapolating the approach data, in the separation range from 200nm-1μm, to the h-intercept. For run 5 of the HTS decanol system (run 1 of the DTS decanol system) a slip length

of 19.0nm (16.0nm) was obtained, which is in close agreement with the residual method results in Table 4.2. Our preference is to use the residual method to determine the slip length, which avoids extrapolations over large distances associated with Eq. (4.7).

## 4.5 Summary and Discussion

This Chapter presents a new in-situ colloidal probe spring constant $k$ calibration method that is applicable to all users of colloidal probe AFM. This new technique is based upon examining the residuals Eq. (4.7). The residuals used specifically in this study are the differences between experimental colloidal probe force-distance data and Vinogradova slip theory. The $k$ value is adjusted between $k_{therm}$ and $k_{in\text{-}situ}$ in 0.01 N/m increments and V-theory is fitted to the force-distance data where the only adjustable parameter in V-theory is the slip length $b$. The optimal $k$ value is where the residuals are symmetrically displaced about zero for all separations $h$. The calibration allows for an in-situ determination of the AFM cantilever spring constant that is representative of the system. The residual spring constant calibration for n-decanol $k_{res}$ indeed exhibits minimal deviations symmetrically displaced about zero as a function of separation as shown in Fig. 4.2.A (middle line).

In order to determine the most accurate value for $k$ using this residual calibration method, very large borosilicate spheres of diameter $2r \sim 55\mu m$ attached to V-shaped cantilevers were used. n-Decanol was chosen as the calibration liquid as it possesses a large viscosity, $\eta \sim 11.2$ mPa s at 25$^{o}$C. The combination of large $r$ and $\eta$ provides a large hydrodynamic force $F_h$ (Eq. (4.2)) for our colloidal probes, hence, making our measurements very sensitive to the precise value of $k$. Use of such large colloidal probes possesses other advantages: (i) the cantilever drag force (Appendix 4.D) is relatively small and (ii) large separations ($h \sim 2\mu m$) can be used while still remaining in the regime where $h << r$, as required by V-theory. Additional constraints, important in this work, are that the silicon wafer surface and colloidal probe possess low RMS surface roughness and few, if any, large asperities. The n-alkyl silane coating (Appendix 4.C) is of high quality, as demonstrated by the low contact angle hysteresis given in Table 4.1.
This residuals spring constant method is reproducible to within 1% over 6 runs for each of the two silane coated systems that were examined (Table 4.2). The expansion representation[36,226] (Eq. (4.7), Fig. 4.3.C) and varying cantilever drive velocity tests all indicate that the slip length $b$ is shear rate independent as assumed in V-theory. To check that $k_{res}$ is indeed the actual

cantilever spring constant for our system, the residuals of two other liquids (n-hexadecane and n-octane) were examined where $k_{res}$ is fixed and the only adjustable parameter is the slip length $b$. The residuals for both of these liquids exhibit no systematic deviations as a function of separation (Fig. 4.2.B). In these experiments it's important that the geometry of the cantilever remains unchanged in order that the tilt contribution to the cantilever spring constant remains unaltered.

Two other popular spring constant calibration methods have also been evaluated using the residuals in this Chapter. The thermal noise spring constant $k_{therm}$, without the additional corrections described in Appendix 4.B, is approximately 25% below the value determined via the residual calibration method which results in a slip length which is over-estimated by a factor of 2 (Table 4.2). The residuals from this thermal method consistently deviate below zero (Fig. 4.2.A, lower curve). Although there are corrections to the thermal noise method which can account for the tilt and torque (Appendix 4.B), these corrections are insufficient to account for the difference between $k_{therm}$ and $k_{res}$. The in-situ method of Craig and Neto provides a more reliable estimate of the spring constant compared with the thermal noise method because it intrinsically includes contributions from the tilt and torque due to the geometry of the cantilever and attached colloidal probe. However, this latter method assumes that the slip length is zero at the solid-liquid interface. For the n-decanol calibration liquid that was examined, the in-situ method overestimates the cantilever spring constant $k_{in\text{-}situ}$ relative to the residual calibration method by approximately 10%; consequently, the residuals for the in-situ method consistently deviate above zero (Fig. 4.2.A, upper curve). This overestimate for the spring constant leads to a lower slip length, relative to the residuals calibration method, by approximately 20-25% (Table 4.2).
The residuals spring constant calibration method developed in this study can be applied to any colloidal probe configuration with any cantilever shape as long as the total drag force of the colloidal probe and cantilever is known. This calibration method will be of immediate interest to spherical colloidal probe users in hydrodynamic drainage experiments where the drag force on the spherical probe has been well established.[68,89] Apart from accurately knowing the sphere radius and liquid viscosity, the only additional stipulations for using this residuals calibration are that the colloidal probe and surface are sufficiently smooth and the system must be immersed in a viscous Newtonian fluid.

Finally, we note that use of the residuals is quite general. They can be used to determine the spring constant in the presence of other surface forces $F_{surf}$ provided that an accurate theoretical functional form for these other surface forces is known. If both the hydrodynamic force $F_h$ as well as $F_{surf}$ are present then these two contributions to the total force should be separable provide that $F_h$ and $F_{surf}$ exhibit differing functional forms as a function of the separation $h$.

## 4.6 Acknowledgements

S. P. M would like to thank Dr. C. D. F. Honig for useful discussions. The authors would also like to extend their thanks and gratitude to the support staff at Asylum Research for technical discussions regarding the MFP 3D AFM and associated software and also thank numerous delegates at the inaugural Faraday Discussion Graduate Research Seminar and 146th Faraday Discussion meeting for useful comments and feedback. This research was conducted with the support from the National Science Foundation under grant DMR-0603144.

## 4.7 Appendices

In order to make it easier to replicate this work a number of technical issues are discussed in these Appendices.

## 4.A: Colloidal Probe Calibration

In the Asylum Research MFP-3D AFM, the cantilever is attached to a linear variable displacement transducer (LVDT) which provides the $z$ position of the cantilever. A laser beam reflects off the end of the cantilever onto a position sensitive detector (PSD). The PSD signal, once calibrated, provides information about the deflection $x$ of the cantilever. Following standard practice, this distance to voltage calibration or inverse optical lever sensitivity (InvOLS) is deduced from the region of constant compliance where the colloidal probe is in hard contact with the silicon wafer.[160] With the liquid of interest in thermal equilibrium, the AFM head is leveled, and the InvOLS calibration is performed using a slow drive velocity of 500nm/s where the colloidal probe is pushed against the Si wafer substrate. During the InvOLS calibration, when in the constant compliance region, the rate of change of the cantilever deflection is equal to the rate of change of the LVDT signal. Thus, the known LVDT signal is used to calibrate the PSD output voltage. Ideally, if the cantilever behaves as a simple spring, the PSD voltage will increase

linearly with the LVDT signal. If non-linearities in the constant compliance region are present they are most likely due to some non-linear mechanical behavior of the cantilever as the properties of the PSD have less than a 0.5% non-linearity throughout the full range of the PSD.[280] The InvOLS calibration and all hydrodynamic measurements are conducted only in the linear constant compliance region between ~ 0-5V on the PSD. In practice, a slow (500nm/s) InvOLS calibration is completed before each individual fast (~ 40μm/s) hydrodynamic force measurement; corrections are also made to remove any *virtual deflection*.[239,258] The separation between the colloidal probe and the silicon surface, required in the analysis, is given by $h = x + z$. During a fast hydrodynamic force measurement, the zero of separation (when the surfaces are in hard contact) is determined by the presence of a vertical force when plotted as a function of separation (Fig. 4.3.A inset). The presence of a vertical force can only be obtained if and only if hard contact between the sphere and Si substrate is made and the InvOLS calibration is valid at the point of contact. The zeros of approach and withdrawal are chosen for each individual run based upon this vertical force, thus avoiding the hysteresis inherent in the LVDT signal, as described in similar experiments.[239,258,268]

Sader[281] suggests the universal use of beam shaped AFM cantilevers based upon theoretical calculations that illustrate that V-shaped cantilevers are more susceptible to lateral forces. For the V-shaped colloidal probe cantilevers used in this study, the relevant parameters that determine the (non-contact) lateral forces are the ratios of the colloidal probe position to the cantilever length, $\Delta L/L$ (= 0.14) and the cantilever width to V-cross section, d/b (= 0.25). Fig. 4 in Sader[281] implies that beam shaped cantilevers with these dimensions will be only marginally more stable to lateral forces compared with V-shaped cantilevers of the same spring constant. In this work, V-shaped cantilevers were used because of our extensive past experience at successfully attaching colloidal spheres centered and directly behind the pyramidal imaging tip (Appendix 4.C). The V-shaped cantilevers also allow for reproducible placement of the maximized sum signal, which occurs in only one location.

## 4.B: Improvements to the Thermal Noise Method

In Sec. 4.4 $k_{therm}$ calibrated in air was used as a lower estimate of the colloidal probe spring constant. For convenience the default settings on the Asylum Research MFP 3D AFM were used in evaluating $k_{therm}$ of the assembled colloidal probes. In reality, there are several

corrections that could be applied to provide a better estimate of the *effective* thermal noise spring constant.

$k_{therm}$ is determined by fitting the power spectrum of the colloidal probe thermal noise to a simple harmonic oscillator (SHO) response with added white noise; the adjustable parameters of the SHO fit are: $W_N$ the white noise, $A$ the amplitude at DC,[282] $f$ the resonant frequency, and $Q$ the quality factor of the resonant frequency peak of the cantilever. The fit values of $A$, $f$, and $Q$ are then used in the default thermal spring constant model in the Asylum Research MFP 3D,

$$k_{therm} = \frac{2k_B T}{\pi A^2 f Q} \tag{4.8}$$

where $k_B$ is Boltzmann's constant, $T$ is the temperature (pre-programmed to be a constant at 16.6°C). In the thermal noise method, the end of the cantilever is free to oscillate at its natural resonant frequency far from the surface. In this situation the $InvOLS_{free}$ value describes how the cantilever bends when freely oscillating. The InvOLS determined from the region of constant compliance used to calibrate the PSD is only applicable for an end loaded cantilever ($InvOLS_{end}$) where the cantilever is not allowed to oscillate. Despite recent efforts to determine $InvOLS_{free}$,[283] typically $InvOLS_{free}$ is calculated from $InvOLS_{end}$ by assuming a default correction factor[272-275] $\chi = InvOLS_{free} / InvOLS_{end} = 1.09$. This default InvOLS correction factor is expected to depend upon the focused laser spot size and position on the cantilever.[274] V-shaped cantilevers are expected to have different thermal fluctuation responses when compared to beam shaped cantilevers;[262,284] these differences in thermal fluctuations due to cantilever shape can be taken into account by experimentally determining the $InvOLS_{free}$ value.

$InvOLS_{free}$ can be determined experimentally using an AC force approach.[285] Fig. 4.4 for a non-colloidal V-shaped cantilever shows the damping of the free amplitude oscillation as the surface is approached. $InvOLS_{free}$ is calibrated from the linear variation in PSD signal as a function of LVDT signal immediately before hard contact. For this specific V-shaped cantilever the average InvOLS correction factor is $\chi = 1.07 \pm 0.04$ (which is close to the default value derived for beam shaped cantilevers, despite the fact that we are using a V-shaped cantilever). Difficulties arise in determining $InvOLS_{free}$ when the large 55μm diameter colloidal probe is attached to the AFM cantilever. The accuracy of the thermal method for use with these large colloidal probes could be improved by being able to experimentally determining the $InvOLS_{free}$ value and not relying on the default correction value of $\chi = 1.09$. For both colloidal and non-

colloidal probes having a non-fixed temperature would also improve the accuracy of the default thermal model. Note that $InvOLS_{free}$ ($InvOLS_{end}$) is called Amp InvOLS (Def InvOLS) in the Asylum Research MFP 3D AFM software.

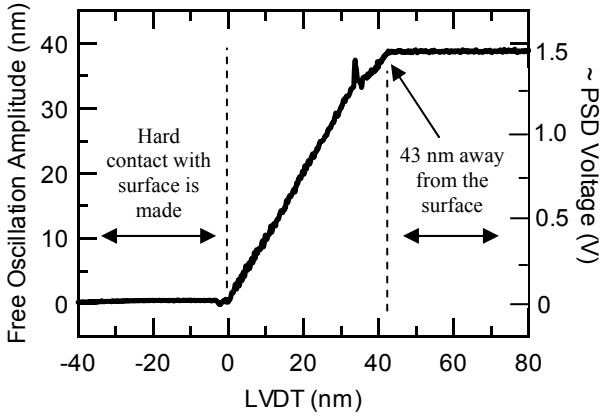


**Fig. 4.4: Free oscillation amplitude/PSD voltage signal in air as a function of the LVDT signal for a non-colloidal NP-S series probe from Veeco.**

The tilt of the cantilever and attachment of the colloidal probe can markedly change the effective cantilever spring constant $k_{eff}$ compared with the intrinsic cantilever spring constant $k_z$.[86] More specifically, in the notation used by Edwards *et al.* [86]

$$k_{eff} = k_z\left(\frac{T_z}{\cos^2\theta}\right), \tag{4.9}$$

where the term in parenthesis is the correction to the spring constant due to cantilever tilt $\theta = 11^o$ and colloidal probe attachment with "torque correction" $T_z$. From the measured dimensions of our V-shaped silicon nitride cantilever with attached silica colloidal probe[281,286] $k_{eff}$ = 1.08N/m (1.00 N/m) for the HTS (DTS) probe assuming that $k_{therm} = k_z$. Although $k_{eff}$ is 14% larger than $k_{therm}$ these corrections still do not fully account for the ~25% difference between $k_{therm}$ and $k_{res}$.

## 4.C: Silicon Wafer and Colloidal Probe Preparation

In order to produce n-alkyl silane coated Si wafers possessing low contact angle hysteresis (Table 4.1), the following procedure was followed: (i) new Si wafers were sonicated in acetone, (ii) plasma cleaned (Harrick PDC-3G) followed by $CO_2$ snow-jet cleaning at ~300$^o$C, (iii) step ii was repeated, (iv) sonication in ethanol, and then (v) a final sonication in toluene. After each sonication step the Si wafer was dried with $N_2$ gas. The Si wafers were then immediately piranha cleaned for 2 hours (equal volumes of 97.3% concentrated $H_2SO_4$ and

31.5% concentrated $H_2O_2$), rinsed well in 90-100$^oC$ Millipore water, and then quickly dried with a heat gun. A wet chemical silanization technique[232] was modified and used as a guide for the silanization process. The Si samples were immediately transferred to room temperature toluene (50ml). The Si/toluene temperature was then lowered to 0$^oC$ (10$^oC$) if the silanization involved DTS (HTS) in a dry box (relative humidity < 12%) and allowed to reach thermal equilibrium over the course of one hour. The desired silane (0.02ml) was added with the syringe tip submerged under the cold toluene liquid-vapor interface to avoid silane polymerization. The solution was stirred and left undisturbed for five hours. Upon removal, the Si wafers were rinsed twice with fresh chloroform, and then $CO_2$ snow-jet cleaned prior to any measurements.

To prepare similarly well-coated colloidal probes having low surface roughness and few asperities, the following protocol was devised: the MO-SCI silica spheres were first etched in a continuously stirred basic solution of $C_2H_6O$: KOH: $H_2O$ in a ratio 50ml: 6g: 6ml for 2 hours, repeatedly rinsed in continuously stirred 90-100$^oC$ Millipore water, followed by two continuously stirred fresh ethanol rinses. The spheres were then carefully dried with a heat gun. A clean microscope slide was then coated with a vapor deposited trichloro(3,3,3-trifluoro-propyl)silane layer. The excess silane was wiped off with chloroform and a lens cloth and then $CO_2$ snow-jet cleaned. A light dusting of the dried spheres was spread over the glass microscope slide and mounted on the x-y scanner of the AFM. AC mode AFM imaging was used to identify useable spheres of low surface roughness with few asperities. The useable spheres were attached to the desired AFM cantilevers (Veeco NP-S 0.58 N/m nominal spring constants) using the AFM head as follows. Excess cantilevers were first removed from the cantilever chip. The desired cantilever was then pre-cleaned by rinsing in chloroform and carbon tetrachloride and then exposed to short wave UV ozone. A small amount of UV curable epoxy (Norland 61) was placed at the end of the cantilever using a separate optical microscope set-up. The NP-S cantilever with UV glue then replaces the standard imaging tip in the AFM head. With the position of the x-y scanner remaining unchanged, the colloidal sphere possessing low surface roughness and few asperities remains directly under the NP-S cantilever. Using the three leveling legs of the AFM and the two x-y adjustment knobs for the x-y scanner, the colloidal sphere was precisely attached, centered immediately behind the pyramidal tip of the AFM cantilever as the AFM head is lowered. Once the sphere is attached to the cantilever, the apex is then re-imaged to characterize the RMS, it is then exposed to long wave UV for 2 hours to set the glue, and then

heated at 50°C for 12 hours to fully cure the glue. Once cured, Norland 61 is highly chemically resistant to many organic solvents. The colloidal probes were then plasma cleaned, de-charged with a 500 microcurie polonium-210 source, and then silane coated as described above. Upon removal from the silane, chloroform rinses were used to remove excess silane.

In studying different liquids using the same colloidal probe and Si wafer, the AFM colloidal probe holder and Si wafer were rinsed well and/or sonicated in chloroform, blown dry, and then vacuum dried before the next experiment. The cantilever chip was left in the cantilever holder during all the above cleaning steps and the AFM leveling legs were not coarsely adjusted between experiments, thus keeping the geometry of the colloidal probe the same when studying different liquids.

## 4.D: Cantilever drag $F_{cant}$

In colloidal probe AFM, a number of different groups[51,231,258] have attempted to model the cantilever drag $F_{cant}$ in order to subtract this contribution from the total experimental force, thus just leaving the colloidal probe contribution $F_h$. The drag force on the cantilever is not very easy to model accurately; therefore, $F_{cant}$ has been experimentally measured for a non-colloidal cantilever similar to the ones used in this study. For the large colloidal probes of diameter ~55μm, $F_{cant}$ is expected to be a small constant force which is independent of the separation $h$. $F_{cant}$ was measured in n-decanol at ~ 40μm/s over a distance of 2μm at a height of ~55μm above the surface using a *non-colloidal* Veeco NP-S series cantilever with a measured spring constant $k_{therm}$ = 0.40 N/m. The non colloidal cantilever $k$ has been determined using the thermal noise calibration method in air where $\text{InvOLS}_{\text{free}}$ calibration was experimentally determined using an AC force approach (Appendix 4.B).

$F_{cant}$ has been accounted for as follows. The total experimental force is given by $F_e = F_h + F_{cant}$ where $F_{cant}$ is a constant as shown by Fig. 4.5, while $F_h$ is well represented by the Brenner[89] no-slip result (or equivalently V-theory with $b \rightarrow 0$) at least at large separations where slip effects are negligible. For each run, $F_{cant}$ is determined at large separations ($h$ ~ 1.5-2μm) by finding the difference between $F_e$ and V-theory with $b$ = 0.1nm; this difference is then subtracted from $F_e$. $F_{cant}$ ranged from 0.9-1.2nN for HTS and DTS, in close agreement with the results in Fig. 4.5.

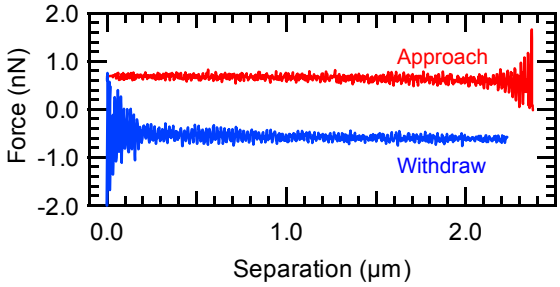


**Fig. 4.5**: **Cantilever drag force $F_{cant}$ in decanol determined for a non-colloidal NP-S series probe at a height of ~ 55.0 to 57.5μm from the surface.**

# Chapter 5 - Determination of the Line Tension of Isolated Spherical Particles at a Liquid-Vapor Interface Using Atomic Force Microscopy[**]

## 5.1 Overview of the Line Tension of Isolated Spherical Particles at a Liquid-Vapor Interface

This study demonstrates a new experimental technique to measure the line tension parameter, via contact angle measurements, of numerous isolated hydrophobic nanoparticles at the three phase interface in a solid-liquid-vapor system using atomic force microscopy (AFM). Spherical silica nanoparticles, having a radius of ~ (66 - 518) nm, are coated with dodecyltrichlorosilane and dispersed in liquid polystyrene (PS) at thermal equilibrium. The PS system is then cooled naturally below the glass transition temperature, thus "freezing" the thermal equilibrium state of the liquid PS and hydrophobized nanoparticles at the interface. An AFM is then used to image the topography of the solid-polymer-vapor interface and extract the microscopic contact angle of single isolated spheres that protrude as spherical caps. The dependence of microscopic contact angle on radius from 147 single isolated nanoparticles is compared to the modified Young equation for different radii spheres allowing accurate determination of the line tension yielding (0.93 ± 0.01) nN. This study provides experimental verification that the line tension presented in the modified Young equation can be accurately determined for collections of singular isolated solid particles on the submicron length scale not previously accessible by other experimental techniques.

## 5.2 Introduction

The contact angle $\theta_\infty$ of a sub-millimeter sized droplet on a solid surface, whose size is much less than the capillary length ($\kappa^{-1}$, Sec. 5.3), so that gravity can be ignored, is determined solely by the surface energies (surface tensions) $\gamma_{ij}$ of the adjacent phases $i$ and $j$. According to the Young equation,[287]

[**] S. P. McBride and B. M. Law, in preparation, portions of this text will soon be submitted to Phys. Rev. Lett. or alternately Langmuir (2012).

$$\cos\theta_\infty = (\gamma_{SV} - \gamma_{SL})/\gamma_{LV} \tag{5.1}$$

where subscript $S$ = solid, $L$ = liquid, and $V$ = vapor. The surface energies, or energies per unit area, are equivalent to a force per unit length. Eq. (5.1) arises from the balance of the forces in the horizontal direction where the "length" is perpendicular to the plane of the page for the droplet shown in Fig. 5.1.A. If the droplet is sufficiently small, then the line tension $\tau$, [91-95] or line energy per unit length associated with the three-phase solid-liquid-vapor contact line of circumference $2\pi b$, also plays a role in determining the contact angle ($b$ is the lateral radius shown in Fig. 5.1.A). The concept of line tension, $\tau$ was first introduced by Gibbs[96] to explain the excess free energy caused by the imbalance of the complex intermolecular forces experienced at the three phase contact line. For a small droplet on a solid surface the microscopic contact angle $\theta$ is given by the modified Young equation,

$$\cos\theta = \cos\theta_\infty - \frac{\tau}{b\gamma_{LV}}. \tag{5.2}$$

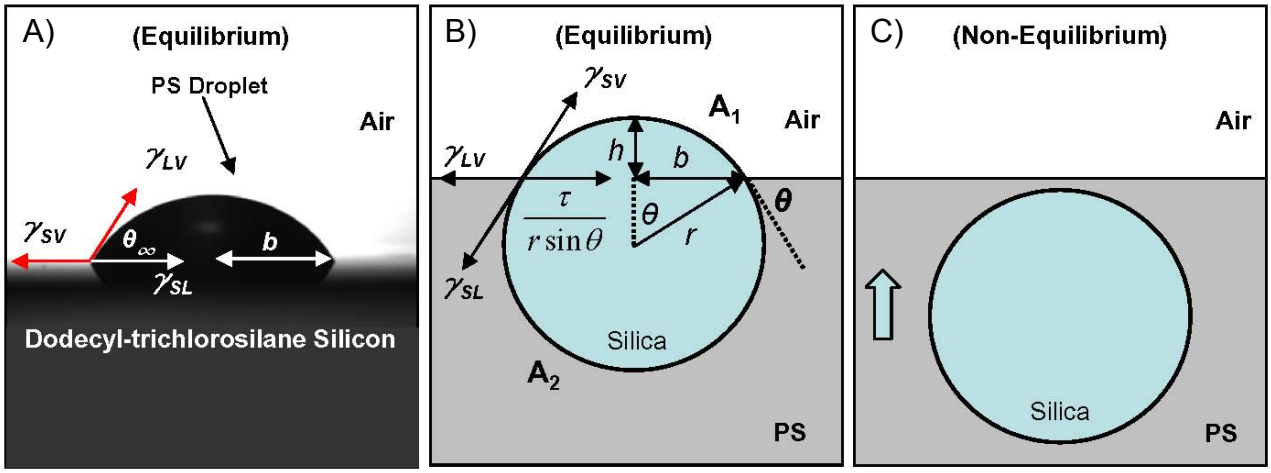


**Fig. 5.1: (A) Liquid droplet of lateral radius *b* and contact angle $\theta_\infty$ on a solid surface. (B) Spherical particle at the liquid-vapor interface. (C) Corresponding spherical particle immersed below the liquid-vapor interface.**

Unlike the surface tension $\gamma_{LV}$, which is always positive, the line tension $\tau$ can be either positive or negative and both signs have been observed experimentally and discussed theoretically. [97,133,156,288] The sign of $\tau$ controls whether the contact angle θ decreases or increases with decreasing droplet size. Experimental estimates for $\tau$ have been obtained for liquid droplets on molecularly smooth solid surfaces, liquid droplets on liquid surfaces, as well as, solid spherical particles at liquid interfaces with the experimental range of negative $10^{-6}$ N to positive

$10^{-6}$ N.[133,156,288] The majority of theoretical line tension studies suggests a magnitude of $\tau \sim 10^{-11}$ N, with $\tau$ either being positive or negative depending upon the system studied.[149,156] Theoretical estimates for $\tau$ are based upon an integration over the dispersion, or van der Waals interaction; with few changes in theoretical models having profound effects on the magnitude and sign of $\tau$.[156] In this Chapter, the primary interest is determining $\tau$ for solid spherical particles at a liquid interface the remainder of this Chapter is restricted to this topic.

Numerous advances in the scientific and industrial applications of *solid particles at the liquid-liquid and liquid-vapor interfaces* have occurred over last decade.[133,157,172,289-307] The concept of adding particles of varying type, size, concentration, and wettability to emulsions, foams, and films to alter and control their physical properties has been well known and well documented for over a century.[308-311] Table 1in Binks and Lumsdon[312] provides experimental findings of numerous systems studied from years 1907-1999 where a wide variety of materials were chosen as particle stabilizers in emulsions. Applications of particles at interfaces ranges from the study of effects of lamellar liquid crystals in hydrophilic sunscreen,[99] fat crystals and starch granules in food emulsions,[100-102] particles in emulsion processes to make clean liquid fuels,[313] nanoparticle catalysts improving efficiency of biofuel production,[314] particle foaming processes resulting in the immobilization of radionuclides from radioactive waste,[315] to nanoparticle cancer treatments and targeted drug delivery mechanisims.[103-107] Iyer *et al.*[316] have recently demonstrated that nanoparticles at interfaces can be made responsive to external stimuli, supporting ongoing work toward the development of numerous device applications including biochemical sensors.[317] The knowledge of how nanoparticles and bio-molecules behave at biological interfaces is of significant importance to the developing field of nanotoxicology.[318-322] In summary, solid particles at liquid interfaces play an important role as surfactants, possessing a tunable ligand coating, and have been self-assembled at liquid interfaces into particle membranes possessing novel mechanical, electronic and optical properties.

One of the most prolific occurrences of solid particles at interfaces in the 20$^{th}$ century was, and still is, froth flotation used extensively in the mineral industry.[158,323-327] In this process, mineral-rich ore particulates are captured at the liquid-vapor interface of rising air bubbles and separated via flotation from non-mineral containing particulates. The success of processes like this is dependent on the contact angle the mineral makes with the air bubble and hence line

tension $\tau$ of the system. The modified Young equation[98] for a spherical particle of radius $R$ situated at a liquid interface, as characterized by the lateral radius $b$ (Fig. 5.1.B), is given by

$$\cos\theta = \frac{\cos\theta_{\infty}}{1 - \frac{\tau}{b\gamma_{LV}}}. \tag{5.3}$$

This equation for a *spherical particle at a liquid interface* differs in form from the corresponding equation for a *liquid droplet on a solid surface* (Eq. (5.2)). As derived in detail in Sec. 5.3, Eq. (5.3) represents the microscopic contact angle for a *single isolated spherical particle* at a *molecularly smooth* liquid interface and arises from considerations of the mechanical equilibrium of the particle at the interface. Eq. (5.3) fully dictates $\theta$ at the interface. For a positive $\tau$ value combined with $\theta < 90^o$, the particle will be pushed into the lower phase, resulting in a smaller $\theta$, meaning the overall length of the three phase contact line must decrease. Similarly, if $\theta > 90^o$ and $\tau$ remains positive, then the particle will be pushed into the upper phase, resulting in a larger $\theta$ and the overall length of the three phase contact line still must decrease. The opposite occurs for a negative $\tau$ value; for $\theta < 90^o$, the particle is pushed into the upper phase, resulting in a larger $\theta$ with the three phase contact line length increasing, while for $\theta > 90^o$, the particle is pushed into the lower phase, resulting in a smaller θ and three phase contact line length must still increase. For macroscopic experiments, the line tension $\tau$ is often neglected without repercussions due to the much larger flotation and capillary forces present in these systems; however, recent theoretical work by Mi *et al.*[174] demonstrates that as the particles get smaller, $\tau$ plays a much more significant role in determining the wetting properties. A recent review by Aveyard *et al.*[292] emphasizes the extreme importance of including $\tau$ and its effect on the stability of micro-emulsions, foams, and films. Similarly, recent experimental work by García-Sáez *et al.*[328] illustrates the strong influence that $\tau$ has on the lateral organization and physical properties of raft-like domains of lipids on liquid interfaces.

Past experimental determinations of the line tension $\tau$ for particles at liquid interfaces have relied on diverse measurement techniques covering a wide range of solid-liquid wettability, $\theta \sim (2^o - 140^o)$. For nanoparticles, of a few nanometers in diameter at liquid interfaces, Aveyard and Clint[169,329,330] estimated $\tau$ from (i) the *collapse pressure for a monolayer of nanoparticles* on a Langmuir trough while Wi *et al.*[108] estimated $\tau$ by applying a statistical mechanical theory to interpret (ii) *nanoparticle adsorption surface tension measurements* at liquid-vapor interfaces. In

general these techniques find small $\tau$ values with magnitude ~ ($10^{-11}$ - $10^{-12}$) N. A disadvantage of both techniques is that they apply formulations applicable for *single* nanoparticles at liquid interfaces to situations where clusters of particles may well exist; it is not yet known how particle clustering at interfaces changes these methods. Using (iii) *Electron microscopy images of ~ (1-10) nm nanocrystals of metallic particles at solid surfaces*, Kasatkin *et al.*[331] found $\tau$ to be negative on the order of $10^{-9}$ N and Siveramakrishnan *et al.*[332] found $\tau$ to be of the order $10^{-10}$ N. An accurate determination of $\tau$ for solid particles on solid surfaces is very dependent upon accurate determinations of the surface energies for the various solid crystallographic axes. Arnaudov *et al.*[333] have developed a unique (iv) *Gel Trapping Technique (GTT)* where a replica cast of Polydimethylsiloxane (PDMS) is made to represent the profiles of particles at gelled liquid interfaces. Particles of radii ~ (40 – 120) nm were studied at these gelled liquid interfaces where Atomic Force Microscopy (AFM) is used to characterize the contact angle $\theta$ of *large collections* of isolated particles at this interface. By using the *average* values of the experimental parameters of the *large collections* of data, line tensions $\tau \sim (10^{-11} - 10^{-12})$ N were found. Recently Maestro *et al*.[334] have found that the contact angles, and consequently the line tensions, that are measured in this gel-trapping technique are very dependent upon the type of solvent that is used to spread the particles at the liquid interface. Line tensions of negative order $10^{-10}$ N to positive order $10^{-9}$ N were found for $R \sim (0.5 – 2.35)$ μm particles depending upon which solvent and interface was used. A number of groups[277,335,336] have used (v) *colloidal probe AFM at a liquid-air or liquid-liquid interface* to determine the line tension from force versus separation curves as the colloidal probe penetrates the liquid interface. In these measurements the radius of the colloidal probe was $R \sim (2 – 5)$ μm. The line tension overall was found to vary widely in these measurements from negative $10^{-6}$ N to positive $10^{-7}$ N. A disadvantage of colloidal probe AFM in measuring $\tau$ is that this technique is restricted to micron size values of $R$ and it is difficult to vary $R$ over a wide range. Scheludko *et al.*[98,168] used a (vi) *particle attachment technique to liquid interfaces* to estimate $\tau$. The particle radii was (1 - 15) μm and $\tau \sim (10^{-9} - 10^{-11})$ N. Similarly, Drelich[337] used the contact angle data collected by Vinke *et. al.*[338] to determine the $\tau$ value to be in the range of ($10^{-9}$ to $10^{-12}$) N for particles with $R \sim (8 – 39)$ μm. Aveyard *et al.*[94] has used optical microscopy to determine the (vii) *contact angle of droplets on large glass beads* with $R \sim (15 – 17.5)$ μm. This technique placed restrictions on the magnitude of $\tau$ ($< 10^{-6}$N) but was insufficiently sensitive for a more definitive determination of $\tau$. This puts the overall

experimental range of $\tau$ for particles at any type of interface from negative $10^{-6}$ N to positive $10^{-7}$ N. This leaves the majority of the range from $R \sim (10 - 500)$ nm experimentally unexplored for *singular* particle contact angle measurements, hence $\tau$.

Accurate experimental determination of the contact angle, hence $\tau$ via the modified Young equation, on collections of/or especially on single particles less than a micrometer on any interface is extremely challenging. [127,133,156,168-176] This fact has lead to the extensive use of simulations. Molecular dynamics (MD) simulations performed by Bresme and Quirke[339,340] predict the value of $\tau$ to be negative and on the order of $10^{-12}$ N for nanometers size particles at the liquid-vapor interface. Bresme and Quirke[341] extended their earlier work to a liquid-liquid interface and found that $\tau$ acting on the particle switched from negative to positive as the size of the particle became larger. The largest of the particles studied exhibited $\tau$ on the order of $10^{-11}$ N. In their work they have also demonstrated that $\tau$ increases linearly with the fluid-fluid surface tension used. The work of Powel *et al*.[342] demonstrates that the modified Young equation is valid down to 1 nm using a Lennard-Jones solid at a Lennard-Jones liquid-vapor interface. Recently Bresme *et al*.[220] have also performed MD simulations for a nanoparticle pair having $\theta \sim 90^{o}$ at the liquid-vapor interface demonstrating that $\tau$ can be negative and on the order of $10^{-12}$ N. These MD simulations have all illustrated that the modified Young equation is very accurate in predicting the contact angle of particles on the nanometer length scale (smallest particle studied by Bresme *et al*.[341] was 15 Å). Recent theoretical work by Zeng *et al*.[176] used density functional theory to study nanoparticles adsorbed at the liquid vapor interface. This work demonstrates that $\tau$ is negative for the fluid-particle interaction strengths examined and that the effects of $\tau$ are greatest for $120^{o} < \theta < 60^{o}$.

As previously shown, the current experimental range of $\tau$ in the literature is between negative $10^{-6}$ N to positive $10^{-7}$ N. These forces are small and are not noticeable in the macroscopic experiences of everyday life; however, with the advent of nanofluidic devices with channels on the order of several nanometers,[343] $\tau$ can become very relevant. A characteristic length scale of the system is to take $\tau$ divided by $\gamma_{LV}$. For example, if the liquid-vapor surface tension is 40 mN/m and $\tau$ is on the order $10^{-9}$ N, the characteristic length scale is on the order of 25 nm; well on the order of current nanofluidic channels. If instead, $\tau$ is on the order of $10^{-11}$ N, then the characteristic length scale, 0.25 nm, dictates this value of $\tau$ will be important on the molecular length scale.

To have the greatest sensitivity to small values of $\tau$, one should study particles with radii distribution of $R \sim (10 - 100)$nm. Additionally, in quantitatively testing the modified Young equation (Eq. (5.3)) one should vary the particle radius over as large a range in $R$ as possible. With these considerations in mind we have therefore developed a new experimental technique for measuring the line tension of solid spherical particles at liquid interfaces. Briefly, several weight percent solution of dodecyltrichlorosilane coated silica particles in polystyrene (PS) is prepared and annealed at high temperature, well above the glass transition temperature of PS. This sample is then allowed to cool below the glass transition temperature of PS. Imaging of protruding single isolated silica spheres at this solidified PS interface, via AFM, enables an accurate test of the modified Young equation (Eq. (5.3)), where the silica particle radius has been varied from ~56 nm to ~ 518 nm. From these experimental results an accurate determination of the line tension $\tau$ for this system can be obtained at the glass transition temperature of PS.

This Chapter is organized as follows: Sec. 5.3 describes the theory for single spherical particles at a liquid-vapor interface, experimental methods and details are provided in Sec. 5.4, experimental results and discussion are given in Sec. 5.5. This Chapter concludes with a summary of our results in Sec. 5.6.

## 5.3 Theory for Singular Spherical Particles at a Liquid-Vapor Interface

A particle of radius $R$ at a liquid-vapor interface can be characterized by the height $h$ of the particle protruding above the interface, the spherical cap lateral radius $b$, and the contact angle $\theta$ (Fig. 5.1.B). A particle at the liquid-vapor interface has energy,

$$E_s = \gamma_{SV} A_1 + \gamma_{SL} A_2 + 2\pi b \tau \tag{5.4}$$

where $\gamma_{ij}$ is the surface energy between phases $i$ and $j$, while $\tau$ is the line tension or energy per unit length associated with the three phase solid-liquid-vapor contact line of length $2\pi b$. This energy, $E_s$ where the three phase contact line is present, must be compared with the energy state $E_b$, where the particle is completely submerged under the interface and the three phase contact line is not present,

$$E_b = \gamma_{SL}(A_1 + A_2) + \pi b^2 \gamma_{LV} . \tag{5.5}$$

In this equation, when the particle is submerged, one must account for the extra liquid-vapor surface area of size $\pi b^2$ and surface energy $\gamma_{LV}$ that is created. In studying particles at interfaces, one must compare these differences in energies to find the energy the particle possesses as a result of the attachment to the interface,[344] thus

$$E = E_s - E_b = (\gamma_{SV} - \gamma_{SL})2\pi Rh + \tau 2\pi b - \gamma_{LV}\pi b^2 . \tag{5.6}$$

The spherical cap area that projects above the liquid-vapor interface is given by $A_1 = 2\pi Rh$.[345] Additionally, geometry dictates that

$$b = R\sin\theta , \qquad h = R(1-\cos\theta) \tag{5.7}$$

therefore,

$$E = \gamma_{LV}\cos\theta_\infty 2\pi R^2(1-\cos\theta) + \tau 2\pi R\sin\theta - \gamma_{LV}\pi R^2\sin^2\theta \tag{5.8}$$

where the Young equation (Eq. (5.1)) has been used in Eq, (5.6) and $\theta_\infty$ represents the macroscopic contact angle that a liquid droplet of PS would make with a molecularly smooth flat similarly coated solid surface. When the particle is in mechanical equilibrium at the interface,

$$\frac{dE}{d\theta} = 0 = \gamma_{LV}\cos\theta_\infty 2\pi R^2\sin\theta + \tau 2\pi R\cos\theta - \gamma_{LV}2\pi R^2\sin\theta\cos\theta \tag{5.9}$$

which gives rise to the modified Young equation given in Eq. (5.3). The modified Young equation determines how the contact angle $\theta$ the particle makes with the liquid-vapor interface is changed by the presence of the line tension $\tau$. In the limit that $\tau \to 0$ or $R \to \infty$ ($b = R\sin\theta$), we have $\theta \to \theta_\infty$ and the macroscopic contact angle is recovered. Alternatively, from Eq. (5.3), if the contact angle $\theta$ and lateral radius $b$ of a particle at the interface can be measured then the line tension can be determined from,

$$\tau = \gamma_{LV} b\left(1 - \frac{\cos\theta_\infty}{\cos\theta}\right) \tag{5.10}$$

provided that the liquid-vapor surface tension $\gamma_{LV}$ and macroscopic contact angle $\theta_\infty$ are known. Eq. (5.10) indicates that the line tension $\tau$ can be positive or negative depending upon whether $(\cos\theta_\infty/\cos\theta) < 1$ or $> 1$. There are additional restrictions on the interrelationship between $\cos\theta$ and $\cos\theta_\infty$. Eq. (5.9) (or equivalently Eq. (5.3)) determines the conditions for mechanical equilibrium of the particle at the liquid-vapor interface and corresponds to the balancing of the surface tension and line tension forces at the interface. An additional necessity for a solution to exist is that the energy $E$ must be a *minimum*,

$$\frac{d^2E}{d\theta^2} = 2\pi R^2 \gamma_{LV}\left[\frac{\cos\theta_\infty}{\cos\theta} - \cos^2\theta\right] > 0\,. \tag{5.11}$$

Here we have used Eq. (5.10) in deriving this equation. For macroscopic particles where $\theta = \theta_\infty$ and $d^2E/d\theta^2 > 0$, provided that $\theta_\infty > 0$, in other words macroscopic particles at the liquid-vapor interface are always stable. In contrast to the stability of macroscopic particles having large $R$, there is a minimum $R$, ($R_{min}$) below which single particles at liquid-vapor interfaces are unstable. When

$$\left.\frac{d^2E}{d\theta^2}\right|_{\theta_{\min}} = 0 \tag{5.12}$$

or equivalently,

$$\cos\theta_{\min} = \left[\cos\theta_\infty\right]^{1/3} \tag{5.13}$$

the energy $E$ no longer possesses a minimum and the energy $E$ crosses over into saddle point behavior. The existence of a minimum contact angle, $\theta_{min}$, also implies according to Eq. (5.10), that there is a particle radius $R_{min}$ below which single particles cannot be observed at a liquid-vapor interface, where

$$R_{\min} = \frac{\tau}{\gamma_{LV}\sin\theta_{\min}\left(1 - \dfrac{\cos\theta_\infty}{\cos\theta_{\min}}\right)}\,. \tag{5.14}$$

To better understand Eqs. (5.3), (5.8), (5.13) and (5.14) we consider a specific example of relevance to our experiments. For a dodecyltrichlorosilane coated silicon substrate at the PS-air interface, with PS having a glass transition temperature ($T_g \sim 46.9^oC$) and surface tension $\gamma_{LV} \approx$ 39.9 mN/m, the macroscopic PS contact angle on a molecular smooth dodecyltrichlorosilane coated surface is $\theta_\infty \approx 64.8^o$ (Sec. 5.4). Our experiments indicate that when the silica spheres are coated in a similar manner as the silicon substrate and deposited into the PS and allowed to cool to $T_g$, $\tau = 0.93$ nN (Sec. 5.5). For these values of $\gamma_{LV}$, $\theta_\infty$ and $\tau$ Fig. 5.2.A plots $E/kT$ as a function of particle radius $R$ and contact angle $\theta$ (Eq. (5.8)) where $kT$ is the thermal energy. The heavy solid line on this plot corresponds to the modified Young equation, Eq. (5.3), indicating the minimum in the energy. Fig. 5.2.B provides an alternative view of $E$ by plotting cross-sections of $E/kT$ versus $\theta$ at several fixed $R$ values.

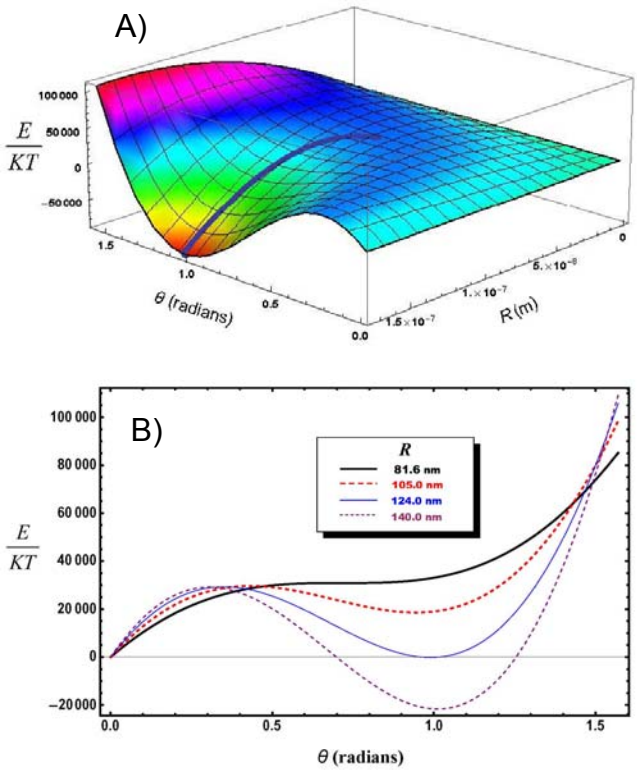


**Fig. 5.2: (A) Plot of $E/KT$ (Eq. (8)) with $\gamma_{LV}$ = 39.9 mN/m, $\theta_\infty = 64.8^o$, and $\tau$ = 0.93 nN; solid line corresponds to the minimum in the (Eq. (8)). (B) Cross-sections of (A) at fixed $R$. Heavy solid line: $E/kT$ at $R_{min}$ (Eq. (14)) where particles with $R \leq R_{min}$ must have a contact angle of $\theta = 0^o$.**

The minimum in energy occurs at around $\theta \sim 1$ radians [$\theta \sim (41.2 \rightarrow 64.8)^o$ as $R$ goes from $R_{min} \rightarrow R_\infty$] corresponding to the minimum described by the modified Young equation (Eq. (5.3)). For $R > 124$ nm this minimum is a *global* minimum and possesses a lower energy than the energy minimum at $\theta = 0$. For 81.5 nm < $R$ < 124.0 nm the "modified Young minimum" is a *local* minimum and possesses a higher energy than the energy minimum at $\theta = 0$; however, particles at the liquid-vapor interface are kinetically trapped in this local minimum because there is a large energy barrier (>> $kT$) which separates the modified Young minimum from the global minimum at $\theta = 0$. At $R_{min}$ = 81.5nm (Eq. (5.14)) and $\theta_{min} = 41.2^o$ (Eq. (5.13)) the modified Young minimum disappears (heavy solid line, Fig. 5.2.B) as the energy $E$ exhibits a saddle point and single particles with $R < R_{min}$ can no longer be found at the liquid-vapor interface. In theory, any single particle at the liquid-vapor interface with $R < R_{min}$ will acquire a contact angle of $\theta = 0$ and will be completely wetted by the liquid (i.e. submerged beneath the liquid interface). In experiment, clusters of particles with $R < R_{min}$ & $R > R_{min}$, which are not described by Eq. (5.8),

still exist at the liquid-vapor interface due additional known forces beyond the scope of this Chapter. All such clusters were not analyzed. The considerations in this section are applicable only for any single spherical particle at a liquid-vapor interface provided that surface tension forces dominate gravitational forces. Specifically, the particle radius $R$ << the capillary length , $\kappa^{-1} = \sqrt{\gamma_{LV} / \Delta\rho g}$ ,[346] where $\Delta\rho$ is the density difference between solid and liquid while $g$ is the acceleration due to gravity.

## 5.4 Experimental Methods

***Materials*** **–**Non-crystalline polystyrene of molecular weight (MW) ~ 1890 g·mol$^{-1}$ and polydispersity index ~ 1.06 was obtained from Polymer Standards Service, Mainz, Germany. The following chemicals of purity 99+%, excepted where stated, were from Sigma-Aldrich: acetone, absolute ethanol, tetraethylorthosilicate (98% purity). From Fisher Scientific (99+%): toluene, chloroform, concentrated hydrofluoric acid solution (48-50 % conc.), ammonium hydroxide solution (29.0 % conc.), concentrated sulfuric acid (97% purity), hydrogen peroxide solution (31.5 % conc.). From Fluka: dodecyltrichlorosilane (99% purity). Silicon substrates were purchased from Silicon Materials Inc. (1 – 10 Ω·cm resistivity and <100> orientation). All water used in this experiment was first purified by a custom reverse osmosis deionization system built by Siemens and then by a Millipore Academic A10 water purification system, which provided 18.2 MΩ·cm resistivity at 25$^{o}$C. Ultrahigh purity dry nitrogen (99.999+ %) was used in all drying steps. Standard Fisherfinest premium microscope slides were used for all sample preparations.

***Silica spheres*** **–** Silica spheres were either purchased from Bang Laboratories ($R_{TEM}$ ~ 248 nm and 518 nm), supplied by Fiber Optic Center, Inc. ($R_{TEM}$ ~ 67 nm), or grown via the Stöber method[347] [$R_{TEM}$ ~ (66 – 184) nm]. The brief procedure given by Khlebtsov *et al.*[348] was used as a guide for the Stöber synthesis. The success of the experiments is highly dependent upon the cleanliness of glassware used. Typical atmospheric dust particles can range from tens of nanometers to tens of microns. One of these submicron particles can completely destroy the cleanliness of the systems studied in this experiment. Therefore, any vial containing water, purchased spheres, or spheres in their initial/final stages of development were first cleaned with Fisherbrand Versa Clean all purpose detergent and tap water, then sonicated in acetone, ethanol,

toluene, and chloroform. Nitrogen is used between each rinse to dry the vial. Then, hydrofluoric acid is placed in the vial, sealed, and rotated for several minutes until visible macroscopic layers of glass are removed from the inside walls of the vial. The vial is then thoroughly rinsed with Millipore water and then dried with a heat gun. All vials have Teflon lids. This glass etching and drying are both performed in a laminar flow hood.

Spherical silica particles of varying sizes ($R_{TEM}$ ~30 – 250 nm) were produced by precisely controlling the amount of ammonium hydroxide (0.7 – 7 mL) in 10 mL of absolute ethanol (Fig. 5.3). These two components were stirred in a 'clean' vial for 5 minutes. The silica particle reaction was initiated by adding 300 μL of tetraethylorthosilicate (TEOS) drop-wise while continuously stirring this mixture. The solution is stirred for an additional hour and then left undisturbed for a minimum of 12 hours, during which time the silica particles continue to grow. (Note that addition of > 300 μL TEOS, while keeping the volume of ethanol constant, did not consistently make spherical silica particles.) The silica particles were separated from solution via centrifugation then decanted (3000 RPMs for spheres $R$ > 130nm and 6000 RPMS for $R$ < 130nm, this corresponds to a force of ~ 800$g$ & ~ 3200$g$ respectively). The silica particles were then cleaned by sonication[349] in 20 mL of fresh ethanol followed by centrifugation and decanting. This procedure was repeated a total of 2 times. Further cleaning was achieved by repeating the above procedure in chloroform a total of 3 times. When the spheres are required for use, the chloroform is removed by applying heat. The dry silica spheres created via the Stöber method, purchased from Bangs Laboratories, or supplied by Fiber Optics Inc. were then cleaned by stirring in fresh piranha solution (12mL sulfuric acid + 12 mL hydrogen peroxide) for 2 hours, followed by centrifugation and decanting. Excess piranha solution was removed by repeated (10x) sonication in fresh hot (~ 90$^{o}$C) Millipore water followed by centrifugation and decanting. This procedure was followed by sonication in ethanol (2x) and then in chloroform (3x), each sonication then requiring centrifugation and decanting. The vial and its contents were dried by alternate sonication and then drying (using a heat gun) until the silica spheres were completely dry as evidenced by their powdery non-stick free flow behavior. The clean silica spheres were stored in the same vial under 10 mL of fresh chloroform until needed.

The dry silica spheres were coated with dodecyltrichlorosilane ligand following the procedure given in McBride and Law.[2] Modifications to this procedure include: prior to starting the coating procedure, the spheres are sonicated in the silanization solvent, toluene, for 20

minutes to ensure complete dispersion after drying. After the silane is added, the vial is sonicated for 1 minute then placed back in the cold chamber. The vial is then removed from the cold chamber and sonicated for 1 minute every 15 minutes for the first hour of silanization. The vial is then left undisturbed for 5 hours in the cold chamber. After the coating procedure, the coated spheres were cleaned by repeated (3x) sonication in chloroform, each sonication followed by centrifugation and decanting. In each Stöber synthesis (100 ± 5) mg of silica spheres were produced, independent of sphere size.

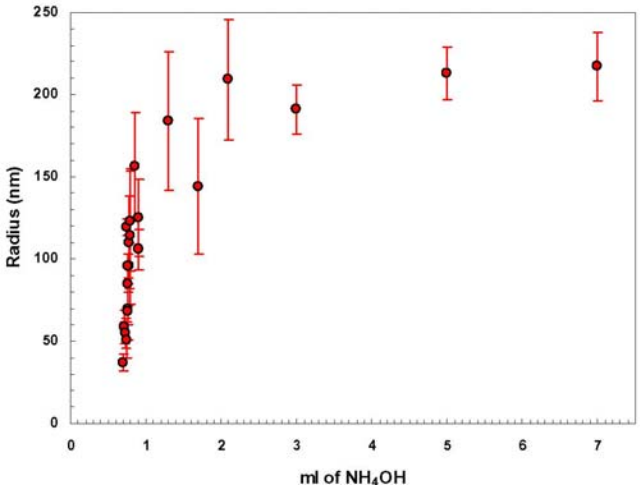


**Fig. 5.3: Stöber silica particle radius as a function of $NH_4OH$ concentration in 10mL of ethanol & 300μL TEOS.**

***PS & silica sphere samples –*** The theory in Sec. 5.3 is only valid for *single* isolated silica spheres at a interface and cannot be applied to clusters of spheres at a interface. In this chapter we study only single isolated silica spheres at the interface of solidified polystyrene (PS) at the glass transition temperature $T_g$ of PS is studied. Coated silica spheres are dispersed in PS at typical concentrations of ~ 2 - 8 wt % as follows. In order to minimize sample contamination all preparation steps were carried out in a laminar flow hood. The coated silica spheres are stored at known concentration in chloroform (100mg of spheres to 10μL of chloroform). Several mL of this chloroform silica particle stock solution is mixed with ~ 30 mg of PS by sonicating for 20 minutes in a thoroughly cleaned vial. Most of the chloroform from this solution is slowly evaporated from the sample using a heat gun and periodic sonication. A 10-20 μL sample of this liquid mixture is transferred to a freshly glass-etched microscope slide contained within a closed

glass Petri dish. The remaining chloroform is then slowly evaporated off by first leaving this sample for 30-60 minutes at room temperature, followed by heating to 100°C for 12 hours; this temperature is well above both $T_g$ of the PS and the boiling point of chloroform (~ 61°C). After heating, the sample, which is now free of chloroform, is then allowed to cool below $T_g$ naturally over many hours, thus "freezing" the liquid equilibrium state of the silica particles at the PS-air interface.

The amount of stock solution added to the PS depends upon the desired wt% of silica. For the $R_{TEM}$ ~ (56, 67, and 68) nm sample, the average $R_{TEM}$ value is less than $R_{min}$ as determined in Sec. 5.3 (Eq. (5.14)) and most spheres remain in the bulk liquid PS due to the fact that $R < R_{min}$. This results in a larger concentration of silica spheres needed (11.9 -19.8) wt % to produce enough spheres to image at the interface. Even with the larger concentration, AFM imaging on the smaller diameter samples took significantly longer to find single isolated spheres at the interface. The wt% given is only estimates of the concentrations as some spheres are lost during the many decanting processes.

***$T_g$, $\gamma_{LV}$ and $\theta_\infty$ –*** The surface tension $\gamma_{LV}$ and macroscopic contact angle $\theta_\infty$ at the glass transition temperature $T_g$ are required in the analysis. A glass transition temperature of $T_g = 46.9^oC$ for the molecular weight polystyrene MW ~ 1890 g·mol$^{-1}$ was determined from the following equation[135]

$$T_g\left(^oC\right) = \left[373 - \frac{1.0 \cdot 10^5}{MW}\right] - 273.15 \qquad (5.15)$$

A long range microscope (First Ten Angstroms 100 Series) was used to determine $\gamma_{LV}$ and $\theta_\infty$ at $T_g$ for pure polystyrene samples in a custom built oven.[108] For experimental consistency in both measurements, both $\gamma_{LV}$ and $\theta_\infty$ were measured from a well-mixed and sonicated 10 mg PS/1mL particle free chloroform mixture from which the chloroform had been evaporated off by heating and vacuum drying.

$\gamma_{LV}$ was determined using the pendant droplet technique by suspending a droplet of this pure polystyrene from the end of a syringe tip inside the oven.[350] From the shape of the droplet one can determine $\gamma_{LV}$ if the PS density as a function of temperature is known.[351,352,353] Fig. 5.4 shows the $\gamma_{LV}$ determination at a sequence of high temperatures. At each specified temperature, $\gamma_{LV}$ was recorded every second for 5 minutes and the average represents the data points; the error

bars representing the standard deviation are smaller than the data points. Linear extrapolation of this high temperature data to $T_g$ given by (Eq. 5.15) yields $\gamma_{LV}$ ( = 39.9 mN/m). Such a large extrapolation from high temperature data to $T_g$ is undesirable, however, high temperatures were used to avoid any possible "skin" formation on the outside of liquid PS pendent droplet at lower temperatures. As a result of this large extrapolation, and to account for potential changes in $T_g$, a large error bar of $\Delta\ \gamma_{LV} = \pm$ 0.5 mN/m was assigned to this surface tension measurement. The overestimate of $\Delta\ \gamma_{LV} = \pm$ 0.5 mN/m would suggest $T_g$ to be in the range (42.2 – 51.6)$^o$C represented by the vertical lines in Fig. 5.4. It has been shown that the presence of nanoparticles in PS-$SiO_2$ mixtures can alter $T_g$ (40% wt $SiO_2$ causes less than a 10$^o$C change in $T_g$).[354,355] Due to the low weight % of $SiO_2$ used in this experiment, the uncertainty in $T_g$ due to the presence of nanoparticles is expected to be less than the assigned uncertainty in $T_g$.

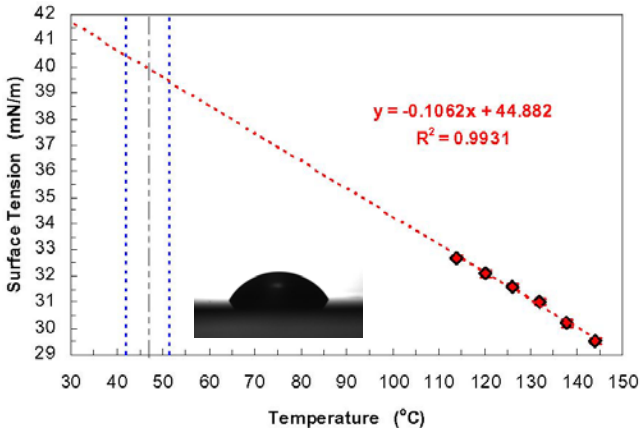


**Fig. 5.4: Polystyrene surface tension $\gamma_{LV}$ extrapolated to the glass transition temperature $T_g$ = 46.9$^o$C. Inset: Solidified polystyrene droplet on a dodecyltrichlorosilane coated Si water from which $\theta_\infty$ = 64.8$^o$ was determined (Fig. 5.1.A).**

The macroscopic contact angle $\theta_\infty$ was determined by placing a solidified 10 mg sphere of the vacuum dried PS on a dodecyltrichlorosilane coated Si wafer in the custom built oven at room temperature. The coated Si wafer is of excellent quality having a critical surface tension $\gamma_c$ of 21.0 mN/m, low surface roughness (0.16 nm over 5x5 μm), and small contact angle hysteresis (as low as 3$^o$) as demonstrated in previous work.[2] The solidified sphere was gradually changed to its liquid state by increasing the temperature to145$^o$C. The initial $\theta_\infty$ was 68.9$^o$ at elevated temperatures. The system was then allowed to cool naturally below $T_g$ to room temperature thus "freezing" the equilibrium state of the liquid droplet (Fig. 5.4 inset). After 2 ¼ hours the contact

angle monotonically decreased to 64.8°. Five measurements over the next 5 ½ hours indicated that $\theta_\infty$ remained constant at (64.8 ± 0.1)°. The absolute uncertainty in this contact angle measurement, $\Delta\theta_\infty$ is estimated at ± 1.0°.

***AFM measurement of silica particles at the solidified PS interface –*** All AFM images of solidified PS surfaces were obtained using an Asylum Research MFP-3D AFM in AC mode with an Olympus AC240TS cantilever. These AFM cantilever tips are specified to have a tip radius of (9 ± 2) nm. Prior to AFM imaging, both the PS sample and AFM imaging tip were exposed to a 500 microcurie polonium 210 source (NRD LLC Model 3C500) which removes any static charge on the sample/tip. AFM imaging of *pure* solidified PS (with no nanospheres present) exhibited a surface roughness of (0.31 ± 0.02) nm over a 30 $\mu m^2$ area, which is comparable to the smoothness of a Si wafer surface. According to theory (Eq. (5.10)), a determination of the line tension $\tau$ for a particular silica sphere situated at a solidified PS interface, can be determined by experimentally measuring two parameters such as the sphere radius $R$ and contact angle $\theta$, provided that $\gamma_{LV}$ and $\theta_\infty$ are known. $R$ and $\theta$ are not the most convenient parameters to measure experimentally. The lateral radius $b$ and protrusion height $h$ are much more readily accessible via AFM and are interrelated to $R$ and $\theta$ via Eq. (5.7). The lateral radius $b$ is most accurately determined from the AFM *Amplitude Trace*, as shown in the upper portion of Fig.5.5, which possesses a higher three-phase boundary line contrast compared with the *Height Trace*. These images are imported into Image Pro Plus 5.0 software where sixteen points are placed equidistant around the circumference of the circular image of the three-phase contact line and then a circle is fitted to these 16 points in order to determine $b$. The worst case error bar in $b$ is estimated to be $\Delta b = \pm 11$ nm (determined from the worst case tip sharpness). The sphere protrusion height $h$ was determined from the *Height Trace* AFM signal (Fig. 5.5 lower images), which at the length scales examined, possesses lower noise than the "*Zsensor"* AFM signal. Based upon observations of many height profiles, the uncertainty in the height measurement is estimated to be $\Delta h = \pm 0.01R$; where, from simple geometry, the sphere radius

$$R = \frac{b^2 + h^2}{2h}. \tag{5.16}$$

At the length scales studied in these experiments, the PS interface is expected to meet the silica sphere horizontally because we are well below the capillary length for this system ($\kappa^{-1} \sim 2$mm).[133] This is verified as shown in Fig. 5.4 lower images.

Theory assumes single isolated spheres. The samples exhibited a non-uniform sphere surface coverage with large sections of the interface covered by interconnected rafts of particles (none of which were analyzed) while other sections contained isolated well-separated spheres. In most cases the measured spheres were well separated from other spheres by distances greater than 10 particle diameters. Any samples which exhibited any nano-scale contamination (Fig. 5.6.A) from *Phase Trace* imaging or three-phase contact line pinning (Fig. 5.6.B) from *Amplitude Trace* [131] imaging were discarded.

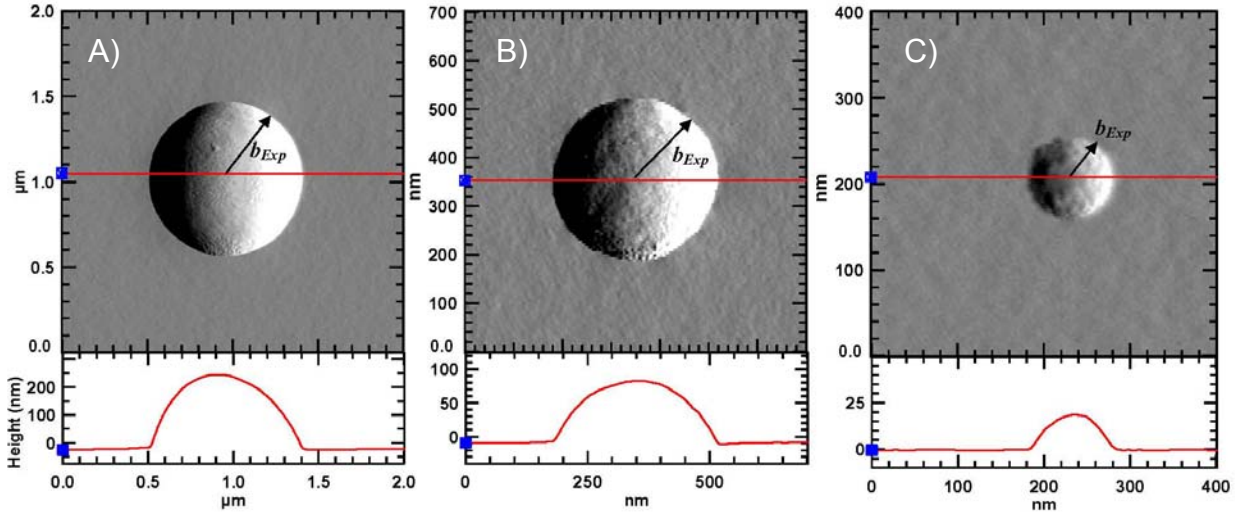


**Fig. 5.5: *Amplitude Trace* (upper) and *Height Trace* (lower) AFM plots for (A) Bangs Laboratories $R \sim 498$ nm, (B) Stöber $R \sim 184$ nm and (C) Particle Solutions $R \sim 88$ nm silica spheres.**

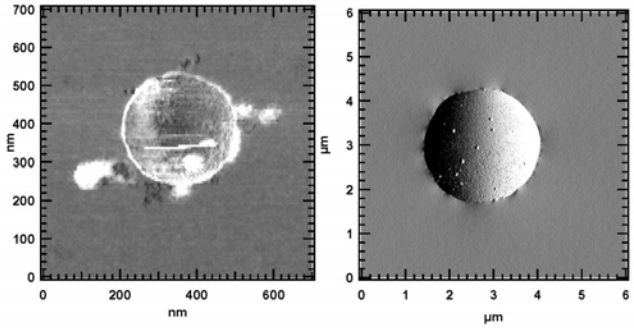


**Fig. 5.6: Examples of invalid experiments due to (A) nanoscale contamination (AFM *Phase Trace)* and (B) three-phase contact line pinning (AFM *Amplitude Trace*).**

## 5.5 Experimental Results and Discussion

The sphere contact angle $\theta$ and radius $R$ are calculated from AFM measurements of the lateral radius $b$ and protrusion height $h$ for each sphere using Eqs. (5.7) & (5.16). Fig. 5.7.A plots $\theta$ versus $R$ for 147 individual spheres with radii varying from ~ 88 nm to 498 nm.

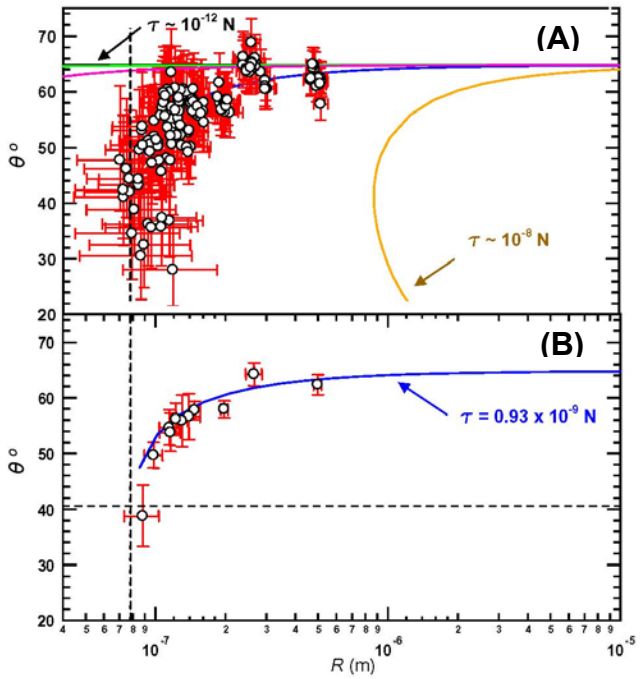


**Fig. 5.7: (A) Contact angle $\theta$ versus particle radius $R$ from 147 AFM measurements of single isolated spheres at the PS-air interface. Solid lines: modified Young equation (Eq. (3)) for various $\tau$ with $\gamma_{LV}$ = 39.9 mN/m and $\theta_\infty$ = 64.8°. (B) Silica particle group averaged results of (A). Solid line: best fit of 147 measurements where line tension $\tau$ = 0.93nN. Vertical and horizontal dashed lines: $R_{min}$ (Eq. (14)) and $\theta_{min}$ (Eq. (13)), respectively.**

The solid lines on this figure are plots of $\theta$ versus $R$ for various values of the line tension, $\tau = 10^{-8}$ N to $10^{-12}$ N with $\gamma_{LV}$ = 39.9 mN/m and $\theta_\infty = 64.8^o$ (knowing $\gamma_{LV}$, $\tau$, and $\theta_\infty$ in (Eq. (5.10)) and by generating systematic $b$ values allows for determination of theoretical $\theta$ values). The error bars in Fig. 5.7.A are calculated using the most extreme cases of experimental inaccuracies of $\Delta\theta_\infty = \pm 1.0^o$, $\Delta b = \pm 11$ nm, and $\Delta\gamma_{LV} = \pm 0.5$ mN/m, and $\Delta h = \pm 0.01$R. The error bars in Fig. 5.7.A highlight that despite using over estimates in the inaccuracy of experimental measurements, a measurable trend in the line tension is still easily observable. A non-linear least squares fit to the 147 measurements gives a line tension of $\tau = (0.93 \pm 0.01)$ nN (Fig. 5.7.B, solid

line). Fig. 5.7.B summarizes the results in Fig. 5.7.A by plotting the average values of $\theta$ and $R$ for each of the 11 groups of Stöber/purchased silica particles (Table 5.1) where the error bars correspond to the experimental standard deviation within each group. The horizontal and vertical dashed lines in Fig. 5.7.B represent $\theta_{min}$ ($\approx 40.4^{o}$) and $R_{min}$ ($\approx$ 78 nm) respectively, deduced from Eqs. (5.13) & (5.14) using most extreme cases of experimental inaccuracies; hence, the experimental data are consistent with these theoretical minima for $\theta_{min}$ and $R_{min}$. Similarly to Bresme and Quirke,[339] our results indicate that the line tension does not depend on the radius of the particle for the range studied.

**Table 5.1: Summary of PS-silica sphere sample characteristics. (#) equals the number of experimental measurements.**

| | (#) | $R_{TEM} \pm \Delta R_{TEM}$ (nm) | (#) | $R_{Exp} \pm \Delta R_{Exp}$ (nm) | $b_{Exp} \pm \Delta b_{Exp}$ (nm) | $h \pm \Delta h$ (nm) | $\theta_{Exp} \pm \Delta\theta_{Exp}$ (deg.) | (#) | Area ($\mu m^2$) | RMS $\pm$ $\Delta$RMS (nm) |
|---|---|---|---|---|---|---|---|---|---|---|
| Bangs Lab. Inc. | 34 | 518 ± 20 | 15 | 498 ± 19 | 440 ± 15 | 267 ± 12 | 62.3 ± 1.8 | 5 | 0.5 x 0.5 | 1.06 ± 0.09 |
| Bangs Lab. Inc. | 51 | 248 ± 21 | 20 | 265 ± 21 | 238 ± 16 | 150 ± 8 | 64.2 ± 2.1 | 5 | 0.3 x 0.3 | 0.82 ± 0.14 |
| Stöber (1.3 ml $NH_4OH$) | 34 | 184 ± 42 | 12 | 197 ± 7 | 167 ± 5 | 93 ± 4 | 58 ± 1.5 | 5 | 0.2 x 0.2 | 0.57 ± 0.05 |
| Stöber (1.7 ml $NH_4OH$) | 19 | 144 ± 41 | 20 | 147 ± 8 | 124 ± 6 | 69 ± 3 | 57.8 ± 1.6 | - | - | - |
| Stöber (0.9 ml $NH_4OH$) | 30 | 125 ± 23 | 5 | 139 ± 16 | 118 ± 13 | 67 ± 8 | 56.6 ± 4.1 | - | - | - |
| Stöber (0.8 ml $NH_4OH$) | 41 | 114 ± 41 | 5 | 130 ± 7 | 107 ± 5 | 57 ± 6 | 55.9 ± 4.6 | - | - | - |
| Stöber (0.77 ml $NH_4OH$) | 41 | 96 ± 14 | 16 | 122 ± 8 | 101 ± 5 | 54 ± 4 | 56.2 ± 2.8 | - | - | - |
| Stöber (0.766 ml $NH_4OH$) | 53 | 85 ± 13 | 11 | 115 ± 11 | 93 ± 7 | 48 ± 4 | 54.7 ± 3.1 | - | - | - |
| Stöber (0.762 ml $NH_4OH$) | 46 | 66 ± 9 | 9 | 116 ± 12 | 87.6 ± 8 | 43 ± 5 | 53.8 ± 3.4 | - | - | - |
| Stöber (0.71 ml $NH_4OH$) | 473 | 66 ± 1 | 16 | 98 ± 9 | 76.2 ± 6 | 35 ± 3 | 49.7 ± 2.3 | - | - | - |
| Particle Sol. LLC. | 131 | 67 ± 7 | 7 | 88 ± 15 | 57 ± 10 | 19 ± 4 | 38.8 ± 5.5 | - | - | - |

As a further check on the particle radii $R$ measurements, AFM averaged radii were compared with TEM radii measurements $R_{TEM}$ determined using a Philips CM-100 TEM (Table 5.1 and Fig. 5.8 including insets). There is excellent agreement between the AFM and TEM measurements for $R$ except for the smallest silica particles that are studied ($R$ < 150nm). The disagreement at the smallest values of $R$ is caused by the fact that the TEM measures all particles sizes in a sample, while the AFM measurements contain only measurements for $R > R_{min}$ found on the interface; according to theory, silica spheres with $R < R_{min} \sim$ 80 nm will not appear as single isolated spheres at the solidified PS interface. As evident in Fig. 5.8 (upper inset - 0.71 ml $NH_4OH$ sample) the smaller spheres produced using the Stöber method become more polydispersed, containing radii much lower than the ~ 80nm, only few of which are found at the interface during experiments.

Caution must be used when applying Eq. (5.3) to experiments. It is derived for simplest and most ideal systems like the one presented here. It is derived for non-interacting particles and

does *not* include the effects of adsorbed contaminants on the solid spheres, surface roughness of spheres, chemical heterogeneity of the sphere coating, flotation forces and capillary forces responsible for inducing particle self assembly on the interface, particle shape dependence, Casmir-like interactions between particles due to thermal fluctuations, and irregularly shaped three phase contact lines responsible for inducing particle self assembly.

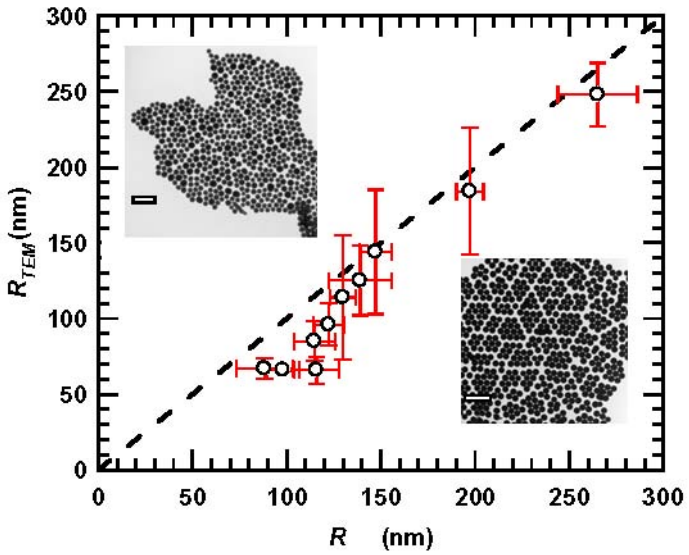


**Fig. 5.8: Comparison of TEM ($R_{TEM}$) and AFM ($R$) determined average particle radii. Insets: TEM images of Stöber silica particles with $R_{TEM}$ = (66 ± 1) nm; scale bar is 500 nm (upper) and $R_{TEM}$ = (184 ± 42) nm; scale bar is 2 µm (lower).**

The technique presented in this study is very unique and few comparison to previous experiments in the literature can be made with the exception of the novel works performed by Arnaudov *et al*.[333] and Maestro *et al*.[334] They both used the gel trapping technique (GTT) developed by Paunov[171] to "freeze" nanoparticles at a liquid - vapor interface by adding polysaccharide gellan, a secretion of the microbe *Sphinogomonas elodea*,[356] to the water phase of systems. The work by Arnaudov *et al.* uses an AFM to measure a PDMS (polydimethylsiloxane) replica cast of the nanoparticles at the interface while the method of Maestro *et al*. uses an SEM to measure the contact angles of the spheres directly. The exact values of $\tau$ obtained for these experiments ranged from ($10^{-12}$ – $10^{-11}$) N and negative $10^{-10}$ N to positive$10^{-9}$ N, respectively. Our method and the work by Arnaudov *et al.* successfully allows for nanoparticles to be imaged at the liquid vapor interface using AFM tapping mode imaging because the effects of capillary

waves during tapping mode imaging are suppressed. The method presented here has several advantages over both the works of Arnaudov *et al*. and Maestro *et al*.

Experimental testing shows the Gellan in GTT is not very surface active and only very weakly effects the surface tension measurements, which effect the contact angle less than the experimentally uncertainty of the contact angle measurement.[171,357] Ideally, my system is completely free of adsorption effects as it is compromised of solely PS and silica spheres after heating to 100$^{o}$C for 12 hours; no spreading liquids or gelling components need to be added to my system. My two component system (PS and silica) is verified by the results of *Phase trace* and *Amplitude trace* imaging acquired from AFM for each sphere.[131] Fig. 5.6.A shows the *Phase trace* for an invalid experiment due to adsorption effects on the nanoscale due to contamination; these effects are often not easily seen in standard *Height trace* imaging. The fact that our system uses no spreading solvent is an advantage as Maestro *et al*. demonstrate the line tine, hence $\theta$, is dependent upon the particle spreading solvent used in the GTT process. It is postulated by Maestro *et al*. that the contact angle solvent effects could be due to residual amounts of solvents trapped in the surface roughness of the spheres; however no surface RMS values are reported for comparison. An advantage of this study over the work of Maestro *et al*. is that smaller diameters spheres can be examined using our method; this is due to the lack of local heating of the surface from beam irradiated at higher magnifications when using SEM. This heating of the PDMS matrix when examining $R \leq 500$ nm may result in a large uncertainty in the measurement of the contact angle as mentioned by Arnaudov *et al.* It should be noted that Masestro *et al.* only acquired two data sets at $R \sim 250$ nm (corresponding to the octane-water interface using isopropyl alcohol as the spreading agent), the rest were $R \sim 500$ nm or larger. The resolution of our technique presented is only limited by the resolution of the AFM due to the sharpness of the tip.

In comparison to Arnaudov *et al*., our method has two advantages: (1) our system uses only pure materials with no spreading solvents and (2) uses truly individual contact angle measurements of *isolated* spheres to determine the $\tau$ of the system (instead of using average $b$ and $\theta$ measurements determined from large collections of spheres measured with an AFM). In our work, the AFM is used to determine each individual $h$ and $R$ via Eq. (5.7), hence the contact angle $\theta_{Exp}$ specific to each isolated sphere is individually determined. If $\tau$ is determined in my experiment using the same procedure except the average $b$ and average $\theta$ data are used for each

sized group like in the work of Arnaudov *et al.*, a ~10% higher value of $\tau \sim (1.03 \pm 0.02)$ nN is obtained.

It is of further interest to examine these experiments focused on the observed discontinuous wetting transition at $\theta_{min}$ and $R_{min}$ as a function of the sphere wettability. The line tension should play a larger role in these types of experiments and have a measurable impact on the stability of these systems. These experiments can easily be accomplished by changing the silane coating on the spheres to one having a critical surface tension, $\gamma_c$ closer to the value of $\gamma_{LV}$ = 39.9 mN/m; for example the silane coating can be changed to that of dimethyldichlorosilane ($\gamma_c$ = 25.3 mN/m) and chloropropyltrichlorosilane ($\gamma_c$ = 32.0 mN/m),[358] may be used considering they have large $\gamma_c$ compared to the current coating of dodecyltrichlorosilane ($\gamma_c$ = 21.0 mN/m).

## 5.6 Summary

In this Chapter we have experimentally tested the applicability of the modified Young equation (Eq. (5.3)) for single isolated spherical particles at liquid-vapor interfaces. The modified Young equation describes how the contact angle $\theta$ for a particle at this interface changes due to the presence of a line tension $\tau$ (or line energy per unit length) associated with the three-phase solid-liquid-vapor contact line of the particle. In the experiments, dodecyltrichlorosilane coated silica particles at the polystyrene-air interface are frozen into position by lowering the temperature of the solution below the glass transition of the non-crystalline mixture; thus, the contact angle $\theta$ of silica particles at this solidified polystyrene interface can readily be measured via atomic force microscopy. Excellent agreement is found between experiment and theory for the dependence of microscopic contact angle $\theta$ on particle radius $R$ at the polymer-air interface (Fig. 5.7.B), provided that the line tension is constant with a value $\tau = (0.93 \pm 0.01)$ nN. Our experimental results are also consistent with the existence of a discontinuous wetting transition, predicted theoretically, where single isolated particles with $\theta < \theta_{min}$ or $R < R_{min}$ are not found at the interface. According to theory (Fig. 5.2) particles with with $\theta < \theta_{min}$ or $R < R_{min}$, at the polymer-air interface, should immediately undergo a complete wetting transition ($\theta = 0$) and be submerged below the polymer interface. Our technique described in this Chapter is only limited by the resolution of the AFM (i.e. the AFM cantilever tip sharpness); hence, this technique can be used to measure microscopic contact angles on nanometer length scales. Bresme and Oettel[133] have specifically requested the development of experimental

techniques to confirm the line tension and contact angle for particles of a few nanometers in diameter at interfaces, as existing techniques are limited. We feel this study is a step towards fulfilling this request.

The authors agree with Aveyard and Clint[329] and Scheludko *et. al.*,[98] that the value for $\tau$ is system dependent (just as interfacial tensions are) and possibly method dependent. Comparison between systems and methods should be treated with extreme caution. Further, in agreement with Amirfazli and Neumann,[156] discrepancies in the sign and magnitude of the $\tau$ parameter in the current literature is partially due to inappropriate comparisons between studies and does not necessarily represent conflicting results, but simply reflects the diversity of the systems studied. This work contributes significantly toward the progress of experimental measurements of $\tau$ in the submicron range, which remains an open area of experimental research.

## 5.7 Acknowledgements

The authors thank Prof. Drs. Stephan Herminghaus and Ralf Seemann for supplying the mono-disperse polystyrene used in this study. The authors are also grateful for the gift of $R_{TEM}$ ~ 67 nm silica spheres (Lot # 101008-1) produced by Particles Solutions, LLC and distributed by Fiber Optic Center, Inc. The authors thank members of the NSF Interdisciplinary Research Teams (NIRT) at Kansas State University for useful comments. This research was funded by NSF grants DMR-0603144 and CTS-0609318.

# Chapter 6 - Summary

Colloidal probe atomic force microscopy (AFM) has been used to study the slip behavior of 18 liquids from two different homologous series, the n-alcohols and the n-alkanes, at molecularly smooth hydrophobic n-hexadecyltrichlorosilane coated surfaces. The AFM and the two chosen homologous series proved to be the simplest apparatus and liquids to investigate the slip length. Using these simple liquids, the same environmental conditions and test surfaces, combined with the nano-Newton sensitivity of colloidal probe AFM, allowed for trends in the slip length to be only attributed to dependencies of the physical properties of the liquids; thus, eliminating many of the suspected causes for the slip length demonstrated in the literature. Investigations reveal that the slip behavior is governed by the bulk viscosity $\eta$ of the liquid, specifically, the slip length $b \sim \eta^x$ with $x \sim 0.33$. For separations $h > 50nm$ the slip lengths were shear rate independent and agreed with Vinogradova theory.[68] The slip length parameter is expected to play a major role in micro and nanofluidic devices which are becoming a more prominent component of our lives.[8-11] Understanding the slip length at the interfaces within these devices will become a necessity for improved design characteristics.

In colloidal probe AFM, surface forces cannot be measured without an accurate determination of the cantilever spring constant. It has been shown the effective spring constant $k$ depends upon the cantilever geometry of the experiment and therefore should be measured in-situ. With current in-situ calibrations in viscous fluids extremely limited, a new in-situ $k$ calibration method was developed. This new method is based upon the residuals, namely, the difference between experimental force-distance data and Vinogradova slip theory, and is contrasted with two other popular $k$ determination methods. The optimal $k$ is the value of $k$ where the residuals are symmetrically displaced about zero for all colloidal probe separations. In the residuals method, the only adjustable parameter when comparing the experimental force-distance data and Vinogradova slip theory is the slip length parameter $b$ (the $k$ value remains fixed at each comparison). This new calibration method is applicable to all users of colloidal probe AFM. The calibration allows for an in-situ determination of the AFM cantilever spring constant that is representative of the system. The only constraints, important in this work, are that the silicon wafer surface and colloidal probe possess low RMS surface roughness and few, if any, large asperities. This calibration method will be of immediate interest to spherical colloidal probe

users in hydrodynamic drainage experiments where the drag force on the spherical probe has been well established.[68,89] Apart from accurately knowing the sphere radius and liquid viscosity, the only additional stipulations for using this residuals calibration are that the colloidal probe and surface are sufficiently smooth and the system must be immersed in a viscous non-volatile Newtonian fluid. It is expected that this calibration method may well become an essential component for any quantitative colloidal probe AFM experiment in a viscous fluid.

The AFM also has the capability to acquire accurate sub nanometer height profiles of structures on interfaces. Using this capability, a new experimental technique to measure the line tension parameter, indirectly via contact angle measurements of numerous isolated nanoparticles situated at the liquid-vapor interface has been presented. This novel approach suppresses the motion of the dodecyltrichlorosilane coated silica spheres at the liquid-vapor interface by freezing them into position by lowering the temperature of a heated solution of liquefied polystyrene (PS) and sphere mixture below the polystyrene's glass transition temperature. The microscopic contact angle $\theta$ of silica particles at this solidified polystyrene interface can then readily be measured via atomic force microscopy. The dependence of microscopic contact angle on radius from 147 isolated nanoparticles is compared to the modified Young equation for different radii spheres allowing accurate determination of the line tension yielding a value of $(0.93 \pm 0.01)$ nN. The modified Young equation describes how the contact angle $\theta$ for a particle at this interface changes due to the presence of a line tension $\tau$ (or line energy per unit length) associated with the three-phase solid-liquid-vapor contact line of the particle. This study provides experimental verification that the line tension presented in the modified Young equation can be accurately determined for isolated solid particles on the submicron length scale not previously accessible by other experimental techniques. In examining this submicron range, our experimental results also verify the existence of a discontinuous wetting transition, predicted theoretically, where single isolated particles with $\theta < \theta_{min}$ or $R < R_{min}$ are not found at the interface. This work contributes significantly toward the progress of experimental measurements of $\tau$ in the submicron range, which remains an open area of experimental research. The technique presented is only limited by the resolution of the AFM (i.e. the AFM cantilever tip sharpness); hence, this technique can be used to measure microscopic contact angles on nanometer length scales. Overall, the AFM is an ideal instrument for conducting the surface science experiments discussed within this dissertation.

# Appendix A - Derivation of Vinogradova Theory

In classical fluid mechanics the no slip boundary condition between a liquid and a solid is usually assumed to be valid. As stated by Vinogradova, early experiments[359-363] and polymer physics models[364,365] however found that the no slip boundary condition is not always valid and that the no slip boundary condition may sometimes need to be relaxed. This appendix verifies the original mathematical derivation of the slip length parameter between two identical non-deformable hydrophobic spherical surfaces as derived by Vinogradova.[68] It should be used as a guide for future students working alongside the original derivation; its purpose is to provide a starting point for students unfamiliar with the hydrodynamic equations and Mathematica. Not all algebraic steps are shown (but have been completed separately to verify the theory), and are left as exercises for the student; however, all crucial calculations are shown and verified. It is also shown that the experimental parameters in all experiments conform to the assumptions made in the theory, as necessary. This section maybe skipped by the general reader.

In order to make a comparison between force-distance measurements from colloidal probe atomic force microscopy (AFM) and Vinogradova's slip theory (V-theory), the experimental conditions must match the assumptions made in the theory. Fig. 1.2.A describes the slip length, $b$, at the solid-liquid boundary. V-theory originates by solving the Navier-Stokes equations (in cylindrical coordinates) for low Reynolds number hydrodynamics for the case of two spheres of radius $R_1$ and $R_2$ being driven towards each other, Fig. A.1. For the case of $k = 0$ (see original work for definition of $k$) the boundary conditions include an identical slip length present at each non-deformable hydrophobic surface. The theory is only valid for low Reynolds numbers, *(Re)* flow less than ~ 0.5 where viscous forces dominate and separations of $h << R_1$, $R_2$, where $h$ is the separation between the two spheres. These conditions are readily obeyed in our experiments where the largest separation $h(max) = 2\ \mu m$ with the silica colloidal probe diameter $2 \cdot R_1 = 55\ \mu m$ and the substrate is an atomically smooth Si wafer ($R_2 \sim \infty$). The Reynolds number

$$Re = \frac{\rho v D}{\eta} \tag{A.1}$$

Here, $\rho$ is the density of the liquid, $v$ is the velocity of the colloidal probe, $D$ is the diameter of the colloidal probe, and $\eta$ is the bulk viscosity of the liquid. Using the physical parameters of

heptane and decanol, Reynolds numbers of 0.004 and 0.0002 are obtained respectively. V-theory also assumes that all experiments are performed in the lubrication regime[366] where the z-component of fluid flow in the thin film between the apex of the sphere and the substrate is negligible; in other words, the z component of the fluid flow around the colloidal probe is negligible due to the large radius of the colloidal probe compared to the gap separation. The *'contact area'* for the 55 μm sphere is experimentally determined to be ~ 2 x 2 $\mu m^2$ by observing the wear pattern when the two surfaces are rubbed together. Based on the geometry in Fig. A.2, the difference between points (C) & (D) is then only 18.2 nm, thus, the lubrication theory is valid for our experiments; it is almost as if 2 flat surfaces with area 2 x 2 $\mu m^2$ were approaching each other, thus no z-component of fluid flow is possible.

V-theory also assumes there is no φ-component of the fluid velocity. This condition is experimentally meet by using very smooth surfaces; the 5 x 5 $\mu m^2$ and 2 x 2 $\mu m^2$ RMS roughness for the Si substrate and silica colloidal spheres are discussed in Chapter 4. If the surfaces were rough, a φ-component of the fluid velocity would occur as the fluid would need to flow around asperities on the surface, deviating from complete radial flow. V-theory neglects all forces on the fluid except viscous forces and forces as a result of pressure. The theory is only valid for non-volatile Newtonian liquids. The Navier-Stokes equations in cylindrical coordinates for low Reynolds number hydrodynamics can be simplified for the case of two spheres of radius $R_1$ and $R_2$ given the experimental test conditions. The Navier Stokes equation is

$$\overbrace{\rho\Big(\underbrace{\frac{\partial \mathbf{v}}{\partial t}}_{\text{Unsteady acceleration}} + \underbrace{\mathbf{v}\cdot\nabla\mathbf{v}}_{\text{Convective acceleration}}\Big)}^{\text{Inertia (per volume)}} = \overbrace{\underbrace{-\nabla p}_{\text{Pressure gradient}} + \underbrace{\mu\nabla^2\mathbf{v}}_{\text{Viscosity}}}^{\text{Divergence of stress}} + \underbrace{\mathbf{f}}_{\text{Other body forces}}. \qquad \text{(A.2)}$$

Using cylindrical coordinates, the components of the Navier Stokes equation become,

$$\begin{aligned}
r:\ & \rho\left(\frac{\partial u_r}{\partial t}+u_r\frac{\partial u_r}{\partial r}+\frac{u_\phi}{r}\frac{\partial u_r}{\partial \phi}+u_z\frac{\partial u_r}{\partial z}-\frac{u_\phi^2}{r}\right)=-\frac{\partial p}{\partial r}+\mu\left[\frac{1}{r}\frac{\partial}{\partial r}\left(r\frac{\partial u_r}{\partial r}\right)+\frac{1}{r^2}\frac{\partial^2 u_r}{\partial \phi^2}+\frac{\partial^2 u_r}{\partial z^2}-\frac{u_r}{r^2}-\frac{2}{r^2}\frac{\partial u_\phi}{\partial \phi}\right]+\rho g_r \\
\phi:\ & \rho\left(\frac{\partial u_\phi}{\partial t}+u_r\frac{\partial u_\phi}{\partial r}+\frac{u_\phi}{r}\frac{\partial u_\phi}{\partial \phi}+u_z\frac{\partial u_\phi}{\partial z}+\frac{u_r u_\phi}{r}\right)=-\frac{1}{r}\frac{\partial p}{\partial \phi}+\mu\left[\frac{1}{r}\frac{\partial}{\partial r}\left(r\frac{\partial u_\phi}{\partial r}\right)+\frac{1}{r^2}\frac{\partial^2 u_\phi}{\partial \phi^2}+\frac{\partial^2 u_\phi}{\partial z^2}+\frac{2}{r^2}\frac{\partial u_r}{\partial \phi}-\frac{u_\phi}{r^2}\right]+\rho g_\phi \\
z:\ & \rho\left(\frac{\partial u_z}{\partial t}+u_r\frac{\partial u_z}{\partial r}+\frac{u_\phi}{r}\frac{\partial u_z}{\partial \phi}+u_z\frac{\partial u_z}{\partial z}\right)=-\frac{\partial p}{\partial z}+\mu\left[\frac{1}{r}\frac{\partial}{\partial r}\left(r\frac{\partial u_z}{\partial r}\right)+\frac{1}{r^2}\frac{\partial^2 u_z}{\partial \phi^2}+\frac{\partial^2 u_z}{\partial z^2}\right]+\rho g_z \qquad \text{(A.3)}
\end{aligned}$$

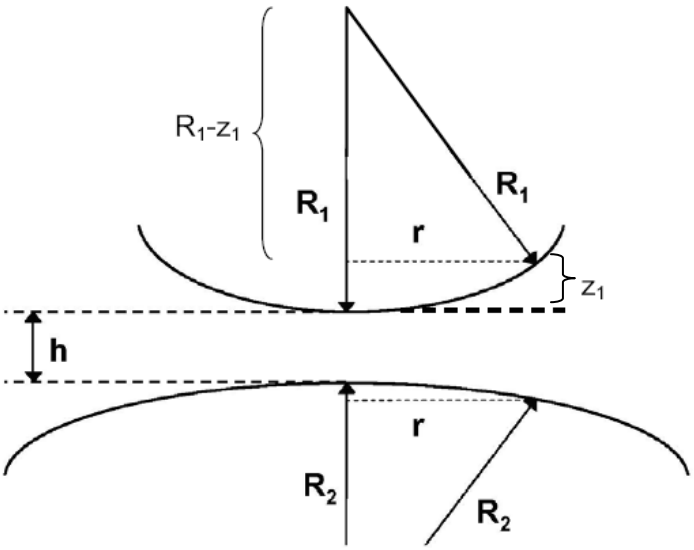


**Fig. A.1: Assumed schematic displaying the geometry under which V-theory is developed.**

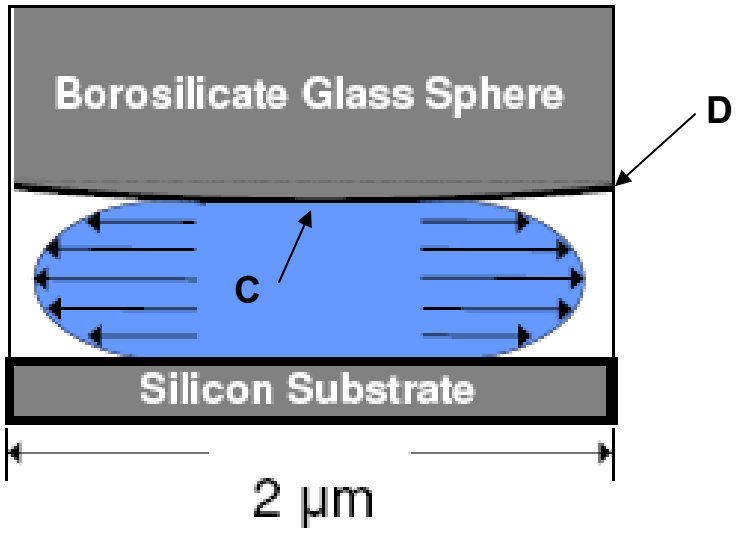


**Fig. A.2: Assumed fluid flow profile in a liquid volume element between the sphere apex and substrate demonstrating that the fluid has a negligible z-component of velocity when in the lubrication regime ($R_1 >> h$).**

Following Vinogradova's original derivation, if we use only non-volatile Newtonian fluids, then the density of the fluid and the amount of fluid remains conserved during transport from one location to another as it is squeezed out from beneath the colloidal probe as this probe is driven towards the substrate; therefore, we can use the continuity equation,

$$\frac{1}{r}\frac{\partial}{\partial r}\left(ru_r\right)+\frac{1}{r}\frac{\partial}{\partial \varphi}\left(u_\phi\right)+\frac{\partial}{\partial r}\left(u_z\right)=0 \tag{A.4}$$

If we follow the assumptions that there are no z & φ components of fluid flow, no unsteady and convective acceleration of the fluid, and no external or body forces on the liquid, then only the following parts of the Navier-Stokes equations and continuity equation will remain.

$$\begin{aligned} \mu\frac{\partial^2 u_r}{\partial z^2} &= \frac{\partial p}{\partial r} \\ \frac{\partial p}{\partial z} &= 0 \\ \frac{1}{r}\frac{\partial}{\partial r}\left(ru_r\right)+\frac{\partial u_z}{\partial z} &= 0 \end{aligned} \tag{A.5}$$

To take advantage of the surviving portions of the Navier-Stokes equations, the surfaces of the spheres must also be expressed in cylindrical coordinates. For the following derivation the *(0,0)* point, or origin, is located at the apex of the bottom sphere in Fig. A.1. From the simple geometry in Fig. A.1,

$$\left(R_1-z_1\right)^2+r=R_1{}^2. \tag{A.6}$$

Expanding this equation and using the quadratic equation to solve for $z_1$ yields,

$$z_1=R_1\pm R_1\left[1-\frac{r^2}{R_1{}^2}\right]^{1/2}. \tag{A.7}$$

Since $r << R_1$ we can approximate the second term using a binomial series to give

$$z_1=R_1\pm R_1\left(1-\frac{r^2}{2R_1{}^2}\right). \tag{A.8}$$

Choosing the minus case for simplicity, any z-point on the surface of the upper sphere may now be approximated as,

$$z_1=h+\frac{r^2}{2R_1} \tag{A.9}$$

where *h* is simply the separation distance between the two spheres. Likewise, to find a similar corresponding z-point on the bottom sphere, the same geometric relations and expansions are used with the only difference being that $R_2$ and $z_2$ are now negative measurements as they are

now measured from the origin of the system. This results in a corresponding point on the bottom sphere as

$$z_2 = -\frac{r^2}{2R_2}. \tag{A.10}$$

If one redefines a new system of coordinates *(r,z)* where $z = z_1 + z_2$, then $z = 0$ for any z-point on the lower sphere and any point on the upper sphere will be,

$$z = h + \frac{r^2}{2R_e} \tag{A.11}$$

where,

$$R_e = \frac{R_1 R_2}{R_1 + R_2}. \tag{A.12}$$

Since a flat surface is used for the second sphere, $R_2 = \infty$; this makes $R_e = R$, where $R=R_1$ is simply the radius of the upper sphere. With the new coordinate system defined, the boundary conditions can be stated. At $z = 0$

$$v_r = b\frac{\partial v_r}{\partial z}. \tag{A.13}$$

and at $z = h + \frac{r^2}{2R_e}$, also written as $z = H$,

$$v_r = -b(k+1)\frac{\partial v_r}{\partial z}. \tag{A.14}$$

Note that for all the experiments conducted within this research where the Vinogradova theory is used, both the colloidal probe and substrate are chemically identical so that $k = 0$ (see original derivation for explanation of dissimilar surfaces where $k \neq 0$).

First we can find the radial velocity flow of the fluid by using the second order differential equation from Eq. (A.5) with the two known boundary conditions given in Eqs. (A.13 & A.14) as shown below.

```
In[32]:= DSolve[{u * v''[z] == c, v[0] == b * v'[0], v[H] == -b * (k + 1) * v'[H]}, v, z]

Out[32]= {{v → Function[{z}, (-2 b^2 c H - b c H^2 - 2 b^2 c H k - 2 b c H z - c H^2 z - 2 b c H k z + 2 b c z^2 + c H z^2 + b c k z^2) / (2 (2 b + H + b k) u)]}}
```

Note that the pressure derivative $\partial p / \partial r$ is treated as a constant and labeled 'c' in the Mathematica code since the pressure derivative does not have any z dependence. The above answer maybe simplified as shown below.

```
In[33]:= Expand[
          (-2 b^2 c H - b c H^2 - 2 b^2 c H k - 2 b c H z - c H^2 z - 2 b c H k z + 2 b c z^2 + c H z^2 + b c k z^2) / (2 (2 b + H + b k) u)]

Out[33]= -(b^2 c H)/((2 b + H + b k) u) - (b c H^2)/(2 (2 b + H + b k) u) - (b^2 c H k)/((2 b + H + b k) u) - (b c H z)/((2 b + H + b k) u) -
         (c H^2 z)/(2 (2 b + H + b k) u) - (b c H k z)/((2 b + H + b k) u) + (b c z^2)/((2 b + H + b k) u) + (c H z^2)/(2 (2 b + H + b k) u) + (b c k z^2)/(2 (2 b + H + b k) u)
```

By grouping terms with similar powers in z, further simplification can be achieved.

```
In[34]:= Simplify[+(b c z^2)/((2 b + H + b k) u) + (c H z^2)/(2 (2 b + H + b k) u) + (b c k z^2)/(2 (2 b + H + b k) u)]

Out[34]= (c z^2)/(2 u)

In[35]:= Simplify[-(b c H z)/((2 b + H + b k) u) - (c H^2 z)/(2 (2 b + H + b k) u) - (b c H k z)/((2 b + H + b k) u)]

Out[35]= -(c H (H + 2 b (1 + k)) z)/(2 (H + b (2 + k)) u)

In[36]:= Simplify[-(b^2 c H)/((2 b + H + b k) u) - (b c H^2)/(2 (2 b + H + b k) u) - (b^2 c H k)/((2 b + H + b k) u)]

Out[36]= -(b c H (H + 2 b (1 + k)))/(2 (H + b (2 + k)) u)
```

Regrouping the terms one arrives at the final answer for the radial flow at the surface,

```
In[37]:= (c z^2)/(2 u) - (c H (H + 2 b (1 + k)) z)/(2 (H + b (2 + k)) u) - (b c H (H + 2 b (1 + k)))/(2 (H + b (2 + k)) u);
```

This radial flow velocity is the same as Eq. (3.13) in the original derivation. This radial flow velocity can then be used in the continuity equation Eq. (A.5) to find the velocity of the approaching spheres. After rearranging the continuity equation one should realize that each term will have some z-dependence. Each term is individually integrated and summed together to get the final result which mathematically is equivalent to Eq. (3.14) in the original derivation.

```
In[38]:= Integrate[c z^2 / (2 u), {z, 0, H}]

Out[38]= c H^3 / (6 u)

In[39]:= Integrate[-c H (H + 2 b (1 + k)) z / (2 (H + b (2 + k)) u), {z, 0, H}]

Out[39]= -c H^3 (H + 2 b (1 + k)) / (4 (H + b (2 + k)) u)

In[40]:= Integrate[-b c H (H + 2 b (1 + k)) / (2 (H + b (2 + k)) u), {z, 0, H}]

Out[40]= -b c H^2 (H + 2 b (1 + k)) / (2 (H + b (2 + k)) u)

In[70]:= c H^3 / (6 u) - c H^3 (H + 2 b (1 + k)) / (4 (H + b (2 + k)) u) - b c H^2 (H + 2 b (1 + k)) / (2 (H + b (2 + k)) u);
```

Following the original derivation, Eq. (3.14) can be used to find the expression for the pressure on the liquid induced by the motion of the approaching spheres. The parameters of A, B, F (=C in original derivation), H, and X are also defined as in the original derivation.

```
In[208]:= B = 2 * b * (2 + k + Sqrt[(1 + k + k^2)]);

In[209]:= F = 2 * b * (2 + k - Sqrt[(1 + k + k^2)]);

In[210]:= A = b * (2 + k);

In[217]:= H = h + r^2 / (2 * R);

In[96]:= Simplify[X[r] = 6 * (A + H) / (-H^2 * (H + B) * (H + F))]

Out[96]= -6 (A + H) / (H^2 (B + H) (F + H))
```

Rearranging Eq. (3.14) from the original derivation by using the boundary conditions that *dp/dr = 0* at *r = 0* and *p = 0* as *r* approaches infinity will yield,

$$p = \int X(r)\mu v r dr$$

```
In[157]:= Integrate[X[r] * u * v * r, r]

Out[157]= -6 R u v (-2 A R / (B F r^2 + 2 B F h R) - (-B F + A (B + F)) Log[r^2 + 2 h R] / (B^2 F^2) +
  (-A + B) Log[r^2 + 2 (B + h) R] / (B^2 (B - F)) + (A - F) Log[r^2 + 2 (F + h) R] / ((B - F) F^2))
```

As *r* approaches infinity this expression, as expected, equals zero as shown below.

$$\text{In[158]:=}\quad \text{Limit}\left[6\,R\,u\,v\left(-\frac{2\,A\,R}{B\,F\,r^2+2\,B\,F\,h\,R}-\frac{(-B\,F+A\,(B+F))\,\text{Log}\left[r^2+2\,h\,R\right]}{B^2\,F^2}+\frac{(-A+B)\,\text{Log}\left[r^2+2\,(B+h)\,R\right]}{B^2\,(B-F)}+\frac{(A-F)\,\text{Log}\left[r^2+2\,(F+h)\,R\right]}{(B-F)\,F^2}\right),\ r\to\infty\right]$$

$$\text{Out[158]=}\quad 0$$

This expression for the pressure can be further simplified.

$$\text{In[159]:=}\quad \text{FullSimplify}\left[\text{Together}\left[6\,R\,u\,v\left(-\frac{2\,A\,R}{B\,F\,r^2+2\,B\,F\,h\,R}-\frac{(-B\,F+A\,(B+F))\,\text{Log}\left[r^2+2\,h\,R\right]}{B^2\,F^2}+\frac{(-A+B)\,\text{Log}\left[r^2+2\,(B+h)\,R\right]}{B^2\,(B-F)}+\frac{(A-F)\,\text{Log}\left[r^2+2\,(F+h)\,R\right]}{(B-F)\,F^2}\right)\right]\right]$$

$$\text{Out[159]=}\quad \frac{1}{B^2\,(B-F)\,F^2\left(r^2+2\,h\,R\right)}\,6\,R\,u\,v\left(2\,A\,B\,F\,(-B+F)\,R-\left(r^2+2\,h\,R\right)\left((B-F)\,(-B\,F+A\,(B+F))\,\text{Log}\left[r^2+2\,h\,R\right]+(A-B)\,F^2\,\text{Log}\left[r^2+2\,(B+h)\,R\right]+B^2\,(-A+F)\,\text{Log}\left[r^2+2\,(F+h)\,R\right]\right)\right)$$

The above expression is mathematically equivalent (if the rules for logarithms and algebra are employed) to Eq. (3.16) in the original derivation as shown below.

```
In[197]:= FullSimplify[Together[(((-3*u*v*R) / (H^2)) * ((2*A*H) / (B*F) +
            (2*H^2) / (F - B) * ((((B - A) / (B^2)) *Log[1 + B / H]) - (((F - A) / (F^2)) *Log[1 + F / H])))]]
```

$$\text{Out[197]=}\quad -\frac{6\,R\,u\,v\left(2\,A\,B\,(B-F)\,F\,R+\left(r^2+2\,h\,R\right)\left((A-B)\,F^2\,\text{Log}\left[1+\frac{2\,B\,R}{r^2+2\,h\,R}\right]+B^2\,(-A+F)\,\text{Log}\left[1+\frac{2\,F\,R}{r^2+2\,h\,R}\right]\right)\right)}{B^2\,(B-F)\,F^2\left(r^2+2\,h\,R\right)}$$

The following equations, which are all identical to the original derivation (after algebraic manipulation), are the results for the pressure equation Eq.(3.15) in the original derivation for the different values of the parameter *k*.

```
In[211]:= Expand[Limit[(-3*u*v*R) / (H^2) * ((2*A*H) / (B*F) + (2*H^2) / (F - B) *
            ((((B - A) / (B^2)) * Log[1 + B / H]) - (((F - A) / (F^2)) * Log[1 + F / H]))), k → 0]]
```

$$\text{Out[211]=}\quad -\frac{R\,u\,v}{b\,H}+\frac{R\,u\,v\,\text{Log}\left[1+\frac{6\,b}{H}\right]}{6\,b^2}$$

```
In[212]:= Expand[Limit[(-3*u*v*R) / (H^2) * ((2*A*H) / (B*F) + (2*H^2) / (F - B) *
            ((((B - A) / (B^2)) * Log[1 + B / H]) - (((F - A) / (F^2)) * Log[1 + F / H]))), k → -1]]
```

$$\text{Out[212]=}\quad -\frac{3\,R\,u\,v}{4\,H^2}-\frac{9\,R\,u\,v}{8\,b\,H}+\frac{9\,R\,u\,v\,\text{Log}\left[1+\frac{4\,b}{H}\right]}{32\,b^2}$$

```
In[213]:= Expand[Limit[(-3*u*v*R) / (H^2) * ((2*A*H) / (B*F) + (2*H^2) / (F - B) *
            ((((B - A) / (B^2)) * Log[1 + B / H]) - (((F - A) / (F^2)) * Log[1 + F / H]))), k → ∞]]
```

$$\text{Out[213]=}\quad -\frac{R\,u\,v}{2\,b\,H}+\frac{R\,u\,v\,\text{Log}\left[1+\frac{3\,b}{H}\right]}{6\,b^2}$$

Eq. (3.17) in the original derivation is derived from a more complex general equation derived in Happel.[367] Note that the second term in the parenthesis of Eq. (3.17) is not actually included in the integration in the original derivation by Vinogradova; this term relates to the pressure outside of the contact region and is insignificant compared to the pressure between the colloidal probe apex and substrate in the contact region. Carrying out the integration of the first term only when $k = 0$ yields,

```
In[227]:= Integrate[1 * (-(R u v)/(b H) + (R u v Log[1 + 6 b/H])/(6 b^2)) * 2 * π * r, {r, 0, ∞}]
```

$$\begin{aligned}\text{Out[227]=}\quad &\frac{1}{3\,b^2}\pi\,R\,u\,v\,\text{If}\Big[\left(\text{Im}\left[\sqrt{h}\ \sqrt{R}\right]==0\ ||\ \text{Re}\left[\sqrt{h}\ \sqrt{R}\right]\neq 0\right)\ \&\&\ \left(\text{Im}\left[\sqrt{-(6\,b+h)\,R}\right]\neq 0\ ||\right.\\ &\left.\left(\text{Re}\left[\sqrt{-(6\,b+h)\,R}\right]\leq 0\ \&\&\ (\text{Im}[(6\,b+h)\,R]\neq 0\ ||\ \text{Re}[(6\,b+h)\,R]\geq 0)\ \&\&\ \sqrt{-(6\,b+h)\,R}\neq 0\right)\right),\\ &R\left(-h\,\text{Log}\left[1+\frac{6\,b}{h}\right]+6\,b\,(1+\text{Log}[h\,R]-\text{Log}[(6\,b+h)\,R])\right),\\ &\text{Integrate}\Big[\frac{r\left(-12\,b\,R+\left(r^2+2\,h\,R\right)\text{Log}\left[1+\frac{12\,b\,R}{r^2+2\,h\,R}\right]\right)}{r^2+2\,h\,R},\ \{r,\ 0,\ \infty\},\\ &\text{Assumptions}\to\left(\text{Im}\left[\sqrt{-(6\,b+h)\,R}\right]==0\ \&\&\ \left(\sqrt{-(6\,b+h)\,R}==0\ ||\ \text{Re}\left[\sqrt{-(6\,b+h)\,R}\right]>0\ ||\right.\right.\\ &\left.\left.(\text{Im}[(6\,b+h)\,R]==0\ \&\&\ \text{Re}[(6\,b+h)\,R]<0)\right)\right)\ ||\ \left(\text{Re}\left[\sqrt{h}\ \sqrt{R}\right]==0\ \&\&\ \text{Im}\left[\sqrt{h}\ \sqrt{R}\right]\neq 0\right)\Big]\Big]\end{aligned}$$

This can be further simplified,

```
In[230]:= Simplify[Expand[1/(3 b^2) π R u v * (R (-h Log[1 + 6 b/h] + 6 b (1 + Log[h R] - Log[(6 b + h) R])))]]
```

$$\text{Out[230]=}\quad \frac{\pi\,R^2\,u\,v\left(-h\,\text{Log}\left[1+\frac{6\,b}{h}\right]+6\,b\,(1+\text{Log}[h\,R]-\text{Log}[(6\,b+h)\,R])\right)}{3\,b^2}$$

This result is identical to the result found in the original derivation for the vertical force for the case of $k = 0$ (after algebra manipulation of course) and is used in all colloidal probe force measurements for the chemically similar colloidal probes and substrates used in this work. The final form of this force for $k = 0$ is presented in Chapters 2, 3, & 4. Similarly, the other pressures for different $k$ values can be integrated to find the vertical force between the different systems.

For $k = \infty$,

```
In[239]:= Integrate[1 * (-(R u v)/(2 b H) + (R u v Log[1 + 3 b/H])/(6 b^2)) * 2 * π * r, {r, 0, ∞}]

Out[239]= 1/(3 b^2) π R u v If[(Im[√h √R] == 0 || Re[√h √R] ≠ 0) && (Im[√(-(3 b + h) R)] ≠ 0 ||
            (Re[√(-(3 b + h) R)] ≤ 0 && (Im[(3 b + h) R] ≠ 0 || Re[(3 b + h) R] ≥ 0) && √(-(3 b + h) R) ≠ 0)),
          R (-h Log[1 + 3 b/h] + 3 b (1 + Log[h R] - Log[(3 b + h) R])),
          Integrate[(r (-6 b R + (r^2 + 2 h R) Log[1 + 6 b R/(r^2 + 2 h R)]))/(r^2 + 2 h R), {r, 0, ∞},
           Assumptions → (Im[√(-(3 b + h) R)] == 0 && (√(-(3 b + h) R) == 0 || Re[√(-(3 b + h) R)] > 0 ||
              (Im[(3 b + h) R] == 0 && Re[(3 b + h) R] < 0))) || (Re[√h √R] == 0 && Im[√h √R] ≠ 0)]]

In[241]:= Simplify[Expand[1/(3 b^2) π R u v * (R (-h Log[1 + 3 b/h] + 3 b (1 + Log[h R] - Log[(3 b + h) R])))]]

Out[241]= (π R^2 u v (-h Log[1 + 3 b/h] + 3 b (1 + Log[h R] - Log[(3 b + h) R])))/(3 b^2)
```

and for $k = -1$.

```
In[244]:= Integrate[1 * (-(3 R u v)/(4 H^2) - (9 R u v)/(8 b H) + (9 R u v Log[1 + 4 b/H])/(32 b^2)) * 2 * π * r, {r, 0, ∞}]

Out[244]= 1/(16 b^2) 3 π R u v If[(Im[√h √R] == 0 || Re[√h √R] ≠ 0) && (Im[√(-(4 b + h) R)] ≠ 0 ||
            (Re[√(-(4 b + h) R)] ≤ 0 && (Im[(4 b + h) R] ≠ 0 || Re[(4 b + h) R] ≥ 0) && √(-(4 b + h) R) ≠ 0)),
          R (-3 h Log[1 + 4 b/h] + (4 b (-2 b + 3 h + 3 h Log[h R] - 3 h Log[(4 b + h) R]))/h),
          Integrate[(r (-8 b R (3 r^2 + 4 b R + 6 h R) + 3 (r^2 + 2 h R)^2 Log[1 + 8 b R/(r^2 + 2 h R)]))/(r^2 + 2 h R)^2, {r, 0, ∞},
           Assumptions → (Im[√(-(4 b + h) R)] == 0 && (√(-(4 b + h) R) == 0 || Re[√(-(4 b + h) R)] > 0 ||
              (Im[(4 b + h) R] == 0 && Re[(4 b + h) R] < 0))) || (Re[√h √R] == 0 && Im[√h √R] ≠ 0)]]

In[247]:= FullSimplify[
           Expand[1/(16 b^2) 3 π R u v * (R (-3 h Log[1 + 4 b/h] + (4 b (-2 b + 3 h + 3 h Log[h R] - 3 h Log[(4 b + h) R]))/h))]]

Out[247]= -(3 π R^2 u v (3 h^2 Log[1 + 4 b/h] + 4 b (2 b - 3 h - 3 h Log[h R] + 3 h Log[(4 b + h) R])))/(16 b^2 h)
```

# Appendix B - Using Igor Pro Programs to Acquire Colloidal Probe Force Measurements and Slip Length Measurements

## B.1 Overview of Colloidal Probe AFM Force and Slip Length Measurements

This appendix outlines the step-by-step procedure of using the Igor Pro software/programs to determine accurate and reliable colloidal probe force and slip length measurements discussed in detail in Chapters 3 and 4 of this dissertation. This appendix has been specifically written for an incoming graduate student and may be skipped by the general reader. The comments and details in portions of this appendix have come from the Igor Pro software programming manuals,[368] information within the Igor Help files for the MFP-3D AFM, personal experience, trial and error, and/or information obtained through phone conversations with Asylum Research technical support team (specifically Jason Bemis: 1-805-696-6467 ext. 229, or general technical support: 1-888-472-275). When colloidal probe work is discussed, all reported results are obtained using a ~ 55μm diameter colloidal probe (the cantilever without a sphere is an NP-S1 from Veeco; published k = 0.6 N/m without sphere attached) and a similar silane coated silicon wafer for the substrate. These instructions are meant to be used in conjunction with the stand alone Asylum Research MFP-3D Atomic Force Microscope in room 35 Cardwell Hall @ KSU that has already been appropriately cleaned and leveled (see videotape series for cleaning/leveling procedure).

All basic procedures using the Igor Pro software for plotting, fitting , etc. and Igor Pro programming are given in the Igor Pro software manuals.[368] The program files that have been created for use in all the following operations that automatically provide answers with the click of a mouse button should be analyzed and studied so that the complete process of what is happening with each mouse click is understood (otherwise the programs are simply "black boxes" to the new student, which is undesirable). I have completely annotated these software programming files to make understanding them easier. With any Igor Pro file open (such as 'Sean's Set-Up 5-20-2010' on the desktop of the AFM computer) they can be opened/viewed/edited by going to the 'File" tab at the top of the page, then go to the 'Open File'

option, then chose ‘Procedure’, then select ‘My Computer’, ‘C Drive’, ‘Program Files’, ‘Wave Metrics’, ‘Igor Pro’ folder, and then finally ‘Igor Procedures’.[††]

## B.2 Obtaining Accurate Colloidal Probe InvOLS Calibrations

An ideal starting place for this discussion is in parallel with the information found in the Igor Help files; this file is called ‘MFP-3D Spring Constant Tutor’ from Asylum Research (Copyright Asylum Research 2004-2006; Last Updated: 03.16.06). To get to this file, first select the icon on the desktop of the AFM computer labeled ‘Sean’s Set-Up 5-20-2010’, then after Igor Pro has loaded (after fully loaded all the options on the top of the screen turn from grey to black), select the ‘Help’ option at the top of the screen, select the ‘Igor Help Browser’ option, then type ‘spring constant’ into the ‘Search For’ line, and then select the first file that comes up. To start out, much of the same information found in this tutorial will be reproduced in the following section with numerous additional invaluable details and comments.

As with AFM imaging, if very accurate force results are desired the AFM laser should be aligned on a clean de-charged cantilever for 30-60 minutes prior to performing an experiment and the electronics should never be turned off; this is not ideal in high humidity. In these types of experiments the environmental chamber can be used to control the humidity prior to conducting force measurements or prior to injecting liquid for hydrodynamic force measurements. First, maximize the ‘Sum’ signal and minimize the ‘Deflection’ signal on the cantilever and record the ‘Sum’ value in air (see manual). Recording the ‘Sum’ values in air, and in fluid when necessary, will allow you to determine when problems occur; drastic changes in the ‘Sum’ signal indicate a problem. Remember, throughout all of the following steps your goal will be to make nanoscale measurements; thus, the system needs to be clean on the sub nanometer length scale, conditions are not ideal for this, but you will have to make do. Prior to starting the following steps, the AFM system and environmental chamber should be cleaned with ethanol soaked lens cloths and blown off with the UHP nitrogen.

To start, the clean de-charged substrate is placed on the x-y substrate with the rare earth magnets. Then the clean chamber is then placed over the AFM scanner as shown in the video tape series, making sure to align the legs of the head with the cavities in the scanner base, leaving

[††] There exist numerous back-up copies of these Igor Pro programs. Bruce M. Law retains 2 back-up copies on separate external hard drives and Sean P. McBride retains 1 back-up copy on a separate external hard drive.

ample room to move the sample around underneath the probe with the x-y scanner adjustment knobs. If conducting liquid force experiments, the custom designed AFM scanner protective lips on the scanner and microscope objective should be installed (see video tape series for installation procedure). These protect the internal components of the scanner against excess liquid, which by nature of the experiments ***will*** spill off the substrate. If liquid gets behind the scanner plate it will slowly damage the internal components of the scanner and possibly **short out** the circuitry. When ready to start an experiment, remove the AFM head which is far from the surface of the substrate, de-charge the colloidal probe and substrate, place the head back in the chamber, then purge the environmental chamber by opening the valve that shoots nitrogen directly onto the probe until the humidity falls below %10 (usually takes 1-2 minutes, it is assumed to be %0 percent humidity at the probe), then with the gas still on, open the additional side valve on the chamber, this diverts the flow of nitrogen so that liquid can be injected, close the valve that shoots nitrogen directly on to the probe, continue to fill the chamber while the pre-prepared super clean syringe of desired solution is obtained, remove the piece of scotch tape from the syringe port on the chamber, insert the syringe fully without letting the syringe touch the inside walls of the syringe port and slowly inject the desired amount of fluid. Only sufficient fluid is required so that a capillary bridge of fluid exists between the cantilever holder and substrate. Withdraw the syringe fully out of the syringe port without touching the inside walls, replace the piece of scotch tape on the syringe port, shut off the gas, and then close the side valve of the chamber. After the liquid is injected, the optical path of the laser beam has now shifted, so again maximize the 'Sum' signal and minimize the 'Deflection' signal and record the 'Sum' signal value (compare it to the air value, they will be only slightly different, but the air and liquid sums signals should not change drastically, if they do something is wrong or the colloidal probe has been damaged). At this point it is desirable to let the fluid come to thermal equilibrium with the AFM cantilever holder and probe (usually 10 minutes is enough for the deflection signal of the cantilever to stabilize). After the experiment is completed, the syringe port should be cleaned using chloroform/ethanol and lab grade Q-tips in case any liquid has contaminated the side walls of the injection port.

By visual inspection, make sure there is no large macroscopic air bubbles in-between the cantilever and the substrate. If bubbles do exist, angle the head up slightly on one side several times being careful not to break the liquid bridge interaction between the fluid cell and the

substrate; the bubbles should move away from the cantilever and pop as they reach the edge of the liquid. If there is an air bubble between the prism and cantilever this will show up as an unusual deflection in the steps that follow and this set-up procedure will most likely need to be repeated as it is very difficult to remove this type of air pocket in the system.

The next problem to overcome in AFM force measurements (and calibrating the PSD for Contact Mode imaging) is "Virtual Deflection". 'Virtual Deflection', as shown in Fig. B.1, is most likely a mechanical coupling of the cantilever deflection signal to the movement of the z piezo, which controls the up-down motion of the cantilever holder to which the colloidal probe is attached. As the piezo moves, it is most likely causing mechanical stress to the internal components of the AFM; these components under stress are then connected to the mechanical rubber pulley that positions the PSD detector. Its exact origin is still not fully understood by Asylum Research, but they state it also may be dependent on how the light is aligned on the lever. As Fig. B.1 demonstrates this is a problem since far from the surface there should be no force on the cantilever; thus, the measured deflection should be zero independent of the position of the z-piezo, which it is not. The 'Virtual Deflection' calibrations, like all other calibrations, should be done in situ in the same environment (either liquid or air) as the desired experiment.

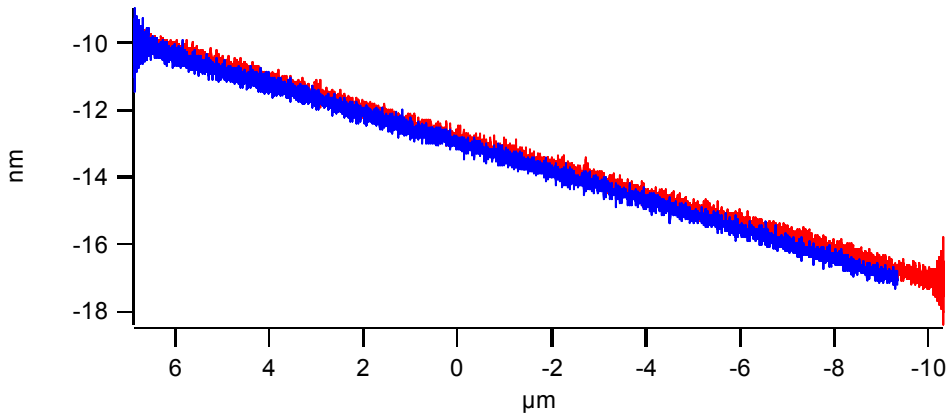


**Fig. B.1: Deflection vs. Z-position in decane for 40 um/s far from the surface.**

With the cantilever mounted, liquid injected, and the system warmed up, lower the AFM head using the leveling wheels, keeping it level as it is lowered. Lower the head such that the cantilever is 200 µm or greater from the surface (thickness of 4 human hairs, this is done by the naked eye). For safety of the probe, click the 'Engage' option in the 'Sum and Deflection Meter'. Open up the 'Force' tab from the 'Master Panel' on the left side of the screen. Enter '–inf' as the

‘Start Dist’ and ‘inf’ as the ‘Force Dist’, this means that the z-piezo will be extended over its full range of motion (~ 16 μm). For collecting regular colloidal probe force measurements 2 μm from the surface is sufficient, but the full range is needed for this Virtual Deflection calibration. Set the ‘Trigger Channel’ to ‘None’. The ‘Trigger Channel’ controls which signal the AFM uses to retract the z-piezo. For example, if we set the ‘Trigger Channel’ to ‘DeflVolts’ with a ‘Trigger Point’ of 2.0V, the AFM would tell the z-piezo to start retracting once the deflection volts due to the bending of the cantilever reaches 2.0V as measured by the PSD (Invols must be calibrated first before ‘DeflVolts’ can be used as a meaningful ‘Trigger Channel’).

Now select ‘Single Force’, this will cause the z-piezo to extend through its full range of motion at approximately 40 μm/sec. The probe should never come into contact with the surface during this calibration. No significant difference in the slope of virtual deflection occurs between fast and slow data far from the surface in air (or in liquid) as shown in Fig. B.1. Due to the slip length parameter and the hydrodynamic force, this is not true for most liquids close to the surface. However, the first fact allows us to assume that if we neglect the slip length and the hydrodynamic force which is very small at slow speeds, we can assume that the Virtual Deflection close to the surface is the same for the fast and slow approach in liquid far from the surface. When calibrating the virtual deflection close to the surface in liquids always use a slow approach speed such as 300-500 nm/sec at which the effects of slip and hydrodynamic force are minute.

After selecting ‘Single Force’ when the probe is far from the surface the Deflection vs. LVDT graph (bottom graph that appears on the screen) should update, hit Ctrl + I to show the cursors (they appears as a circle and square in the lower left corner of the graph). Note, sometimes the approach and retraction data lie on top of each other and it is hard to distinguish them; one can zoom in to distinguish them by selecting a square by dragging the mouse with the left button depressed followed by right clicking in this square area and selecting the zoom option. Click on the cursors with the mouse and drag them to the endpoints on the approach portion of the graph (this would be the endpoints of the red line in Fig. B.1). If the arrow keys on the keyboard are pushed very fast many times the cursors on the graph should both move in the same direction. If one cursor is on the approach data and the other is on the retraction data, and the arrow keys are repeatedly pressed, then the cursors will move toward each other (this is not what we want). In the ‘Master Panel’ under the ‘Force’tab, select the ‘Cal’ tab, from the ‘Set Sens.’

drop down menu, select 'Virtual Defl Line'. This calibrates the Virtual Deflection between the cursor points. This will put a best fit line to your data which calibrates the Virtual deflection (the software removes this fit function describing the Virtual Deflection from your approach and retraction data). Right click on the black best fit line and select 'remove fit_DeflVolts'. If your plot has some non-linearity to it, first use 'Virtual Defl Poly', then remove the fit, do another 'Single Force', then use 'Virtual Defl Line'. This process should be repeated until a flat horizontal line is achieved for the deflection as a function of z-piezo position when the 'Single Force' option is chosen as shown in Fig. B.2.

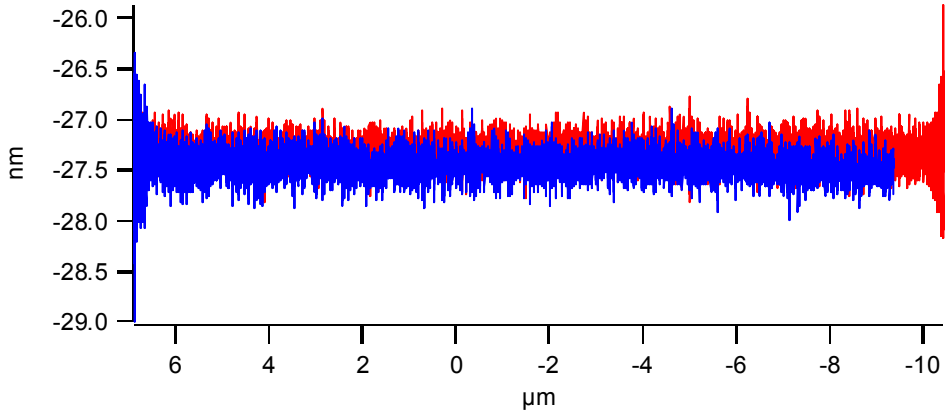


**Fig. B.2: Deflection vs. Z-position in decane @ 40 um/s far from the surface after virtual deflection calibration.**

If a horizontal plot can not be obtained it is most likely due to static charge or contamination (if small spring constants are used, this might be normal behavior, but it has only been observed when static charge or contamination is present using the stiffer cantilevers in this work). This difference between the surface forces and static charge when using floppy colloidal probes might be indistinguishable. Clean the cantilever in the AFM holder first with acetone, then with ethanol followed by a rinse in chloroform and then blown dry with UHP nitrogen. It is okay that the solvents mix at first. This procedure is then repeated 2 more times without the acetone, (acetone might damage the circuit boards on the backside of the holder if in contact for extended periods of time, limit its use), blow dry in-between each solvent with nitrogen, then blow nitrogen on the backside containing the electronics (the prism window should remain clean), and then vacuum dry the entire assembly (starting the AFM with residual solvents on the backside will surely **short circuit** the AFM, so be sure it is dry). After vacuum drying (5 minutes), it is crucial that the backside of the prism in the holder is clean and free of any films. If

not, use lens tissue to clean it and repeat the vacuum drying procedure. Now repeat the Virtual Deflection calibration procedure from the beginning, again including the Staticmaster brush to remove the charge from the probe and the substrate. If the Deflection vs LVDT plot still remains non-linear, the 'Virtual Defl Poly' option could be used, but I would be very suspicious of the data that is produced if using stiff cantilevers, this probably indicates a damaged probe and it should probably be discarded. This cleaning procedure is the same procedure used to clean the colloidal probes between hydrodynamic force measurements in different liquids. The substrate also needs to be cleaned between liquid experiments. This is accomplished by first rinsing in acetone, ethanol, then chloroform, then blow drying with the nitrogen. The substrate, not as fragile as the colloidal probes, is then sonicated in chloroform for a minute and blown dry with the nitrogen. The substrate is then vacuum dried with the cantilever holder at the same time. The Staticmaster brush is then used to remove the static charge from the substrate.

Next, the InvOLS needs to be calibrated which requires a 'Hard Engage'. Performing the 'Hard Engage' for force measurements is the same as discussed in Chapter 2 for AC mode imaging except now make sure that 'Contact Mode' is chosen from the pull down menu in the 'Master Pane'l instead of AC Mode. Press the Engage button in the 'Sum and Deflection Meter' window. Initially the z-piezo is fully extended to its 150V maximum. To start the 'Hard Engage', the large thumbwheel is moved counter clockwise to lower the AFM head onto the sample. All three legs must be continuously adjusted to keep the AFM head level with the substrate. When a beep sound from the computer is heard that means the amplitude of the cantilever has reached the 'Set Point' value (usually 1.0V works well). The cantilever is now interacting with the surface and all the feedback circuitry is activated. The thumbwheel can then be slowly lowered so that the z- piezo is in the approximate center of its range of mobility at 70V as shown in the 'Sum and Deflection Meter'.

It is at this point where you might (90 % of the times) start to hear a high to low pitch humming. Immediately hit the 'Withdraw' button, this fully retracts the z-piezo. This humming is coming from the fact that the surface and the sphere are now interacting producing an auditable resonance frequency. It originates from approaching the surface too fast with the cantilever. If you hit the surface to fast (moving the AFM head down too fast with the mechanical z position wheel) the z-piezo tries to adjust very quickly and overcompensates for the sudden impact and withdraws the cantilever, it then overestimates and then tries to extend the

piezo which is already too close to the surface, it then gets into this infinite feedback loop and never gets out of it. The easiest solution to this is to approach the surface slowly, watch the deflection voltage, when it moves slightly you are getting close to the surface. One can also lower the 'Integral Gain' of the z-piezo on the main panel, this adjusts how quickly the cantilever will respond after hitting the surface; one can think of this as making the cantilever more rigid if lowered and more floppy if increased. Sometimes this effect seems unavoidable and it is best just to operate the wheel well with your right hand and the mouse with your left and do everything at a slow speed. Humm or no humm, click on the withdraw button once 70 Volts on the z voltage is reached to move your colloidal probe back away from the surface.

In the 'Force' tab set the overall 'Force Dist' to 2 μm. You want to have the distance large enough so that you can pull your tip off the surface and so that all hydrodynamic data is captured. This will depend on how sticky your surface and tip are and how much approach and retraction data you want, which depends upon how viscous your liquid is and how fast you are approaching the surface. In air, you may want to use 3 - 4 microns to capture the adhesion data. In the 'Force' tab set your 'Trigger Channel' to 'DeflVolts'. Also set your 'Trigger Point' to + 2 Volts. The 'Trigger Point' is what tells the piezo on what magnitude of the 'Trigger Channel' should be responsible for retracting the z-piezo. When the 'Trigger Point' is reached, the z-piezo then retracts. So in this case, when the photodiode (deflection volts) reads 2 Volts for the deflection, it will then start to retract the piezo. Adjust the position of the photodiode knob so that your deflection away from the surface reads -2 Volts. This is done because we want to have a nice linear region symmetric around zero Volts to fit to a straight line to for the InvOLS calibration; the photodiode is most linear around 0 Volts, which is where we will collect our data for the thermal spring constant calibrations and hydrodynamic force data (see manual for thermal spring constant instructions and Chapter 4 for improvements to the thermal method). Basically, this makes the slope of the contact region (region 2 as described in Chapter 2) of the approach and retraction data centered about the zero Volts reading on the photodiode (adjust the photodiode voltage from -2Volts so that this is true, -2Volts is just a suggested starting parameter and will be different depending upon how large the contact region is). When in liquids, the approach and retraction data is almost exactly the same at low speeds; however, I always use the fast approach data for analysis when doing slip length and hydrodynamic force measurements in liquids.

If working in air, place the hood over the AFM head (the cantilever is super sensitive to vibrations in air, if you don't believe that, just talk or whistle while doing 'Continuous Forces', I am sure you see the sensitivity). The hood is not needed in liquids. Do a 'Single Force' @ 40 μm/s to center the z-piezo with a z-piezo range of 2μm. On the first single force, you should see from the deflection vs. LVDT plot that update if the probe has hit the surface or not, if it did not, you will see the message on the command line that says "Never Triggered," then redo the Hard Engage process. If it did hit, the deflection vs LVDT plot should update, do the second force plot with the same parameters to get the correct data (the correct data is obtained when the approach and retraction data roughly start and end in the same location). Now do a third single force at 300nm/s with a z-piezo range of 2μm. On the deflection vs. LVDT graph, move your cursors so they are in the contact region (Region 2, see Chapter 2) of the force plot (chose a symmetric region about zero volts). Just like before, move the cursors using the arrow keys to test if they are both placed on the approach data. Select 'Deflection' from the 'Set Sens.' drop down menu in the 'Force Panel' under the 'Cal' tab. Make sure the black line on the deflection trace is a decent fit, and then right click on it and select remove fit_Deflection. If the slope of region 2 is extremely non-linear then this colloidal probe can not be used for hydrodynamic colloidal probe measurements. Only a colloidal probe that remains linear in region 2, obeying the linearity of Hooke's Law well past the point of contact between the sphere apex and substrate can be used for accurate colloidal probe measurements (determining this point of contact is discussed in the next section). The InvOLS calibration and the Virtual Deflection calibration are rumored to be slightly coupled; so it is advised that the Virtual Deflection be recalibrated using the cursors as before; therefore, do another single force @ 300nm/s @ 2 um. Usually in air there is only a 1-3nm rise over 2um at this point; this is what we want to get rid of, see Fig. B.3). Use either 'Virtual Defl Poly' or 'Virtul Defl Line' to remove as done before. Sometimes this step might not even be necessary in liquids. See Fig. B.4 for a calibrated data set in liquid not needing re-calibration. Now do another single force @300nm/s @2 um and recalibrate the InvOLS using the 'Deflection' from the 'Set Sens.' drop down menu in the 'Force Panel' under the 'Cal' tab. Now do the final single force @ 300nm/s @ 2 um to recalibrate the Virtual deflection. I always then make sure to do another InvOLS calibration last. Zero the 'Deflection' on the PSD and replace the hood if necessary, then do another single force @300nm/s @2 um. You should see a perfect data set with the linear approach data still perfectly flat (Fig. B.4 is an example of the data at this

point in decane, but a 1nm slope in air is still reasonable. You should copy all three important data sets in the table on the far right under the 'Sum and Deflection Meter' and paste them into a new table (go to 'Windows' tab on the top of the screen and then select 'New Table'). You should select these data sets with the mouse in the new table and rename them by right clicking; these are your slow calibration runs that you might need or want to look at later (allows save and copy the final correctly calibrated slow approach data into a separate table). If you do not rename them, the data will be over written automatically by the data collected the next time the do single force option is selected. At this point one can then determine the thermal value of the spring constant if interested (see manual and Chapter 4, this process is straight forward after withdrawing from the surface). The AFM is now calibrated for the correct InvOLS and Virtual Deflection. Each time the AFM head is touched or adjusted with respect to level, or the laser is readjusted, or a new liquid is inserted, or the 'Sum' signal is adjusted both of these calibrations need to be repeated.

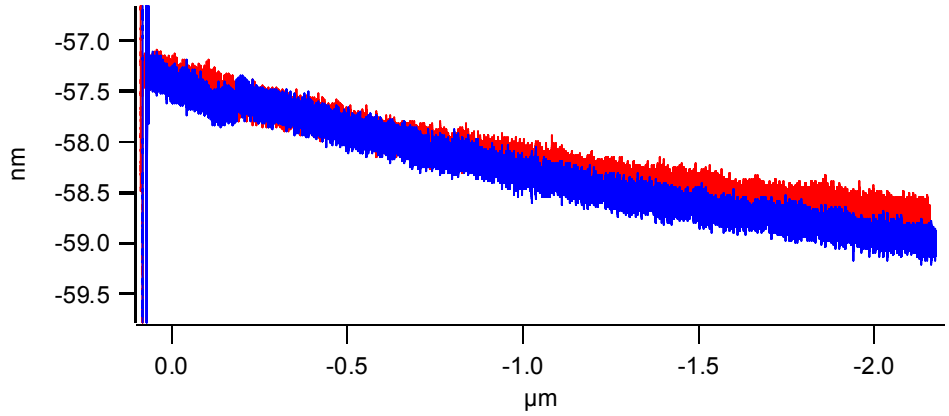


**Fig. B.3: Deflection vs. Z-position in decane showing the approach data when doing a single pull close to the surface after calibrating the virtual deflection far from the surface.**

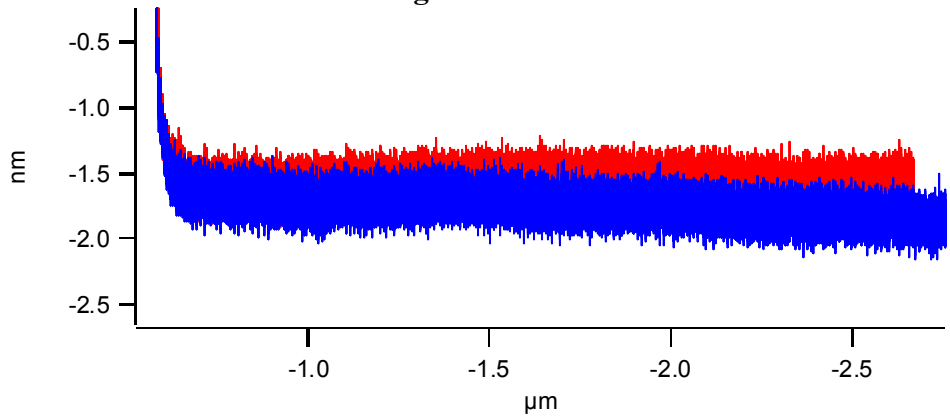


**Fig. B.4: Deflection vs. Z-position in decane after virtual deflection calibration close to the surface and properly calibrated InvOLS. This Fig. shows the approach data after repeating a single pull calibrating the virtual deflection and the InvOLS multiple times.**

## B.3 Obtaining Accurate Colloidal Probe AFM Force Measurements

After the InvOLS and Virtual Deflection calibrations are completed hydrodynamic data can be collected. The 'Velocity' should now be increased back to 40 μm/s (this is only a suggested speed, this value works well for the n-alkanes and n-alcohols). The surface should be re-engaged using the 'Hard Engage'. Now by selecting 'Single Force' multiple times until the approach and retraction data start and end in the same place, an accurate hydrodynamic data set is obtained. Copy and rename the data sets under the sum and deflection meter into a new table (go to the 'Windows' tab on the top of the screen and then select 'New Table'). Name the data as def1, zpos1, and defvolts1 for trial 1 etc. A minimum of three trials in different spots on the substrates should be obtained and analyzed for the slip length measurements. The substrate can be moved underneath the colloidal probe by using the x-y scanner adjustment knobs with the environmental chamber still in place. All three trials should have the same slip length value within several nanometers if the following procedure is carried out correctly.

The problem remains that you have to determine if a hydrodynamic data set is good or not before analyzing it for slip length. In order to properly use the slip software programs to determine accurate slip lengths from the hydrodynamic data, the data must undeniably show that the probe has come into hard contact with the solid substrate for an extended period of time. The part of the program that determines where the zero of separation is based on a derivative and needs at least two consecutive points in contact with the surface to calculate the minimum separation. If hard contact between the sphere and surface is not made the slip length software may still provide a zero point, but this will be totally incorrect. Fig. B.5 shows these artifacts on a deflection vs. separation plot for the separation range of ~ 2.0 μm for colloidal probe hydrodynamic tests collected in decanol. Fig. B.6 shows a close up view of the same data set as Fig. B.5. Remember the separation is defined as the deflection signal *plus* the LVDT, or z-position signal of the z-piezo (see Chapter 4 for details). This means that when the point of zero separation is reached, and the colloidal probe and sphere are in hard contact, the deflection data should go completely vertical independent of how much further the z-piezo is moved. The different trials in Figs. B.5 and B.6 represent 'Single Force' hydrodynamic tests done in exactly the same spot on the substrate; the only change was that the 'Trigger Point' for the 'Trigger Channel', which was on 'deflVolts', was incrementally changed from 1V to 10V. This shows that if too low of a 'Trigger Point' is used **not all the liquid is squeezed out from between the**

**colloidal probe and substrate** and the z-piezo **falsely** retracts. The slip software will also **falsely** determine a zero point for these data sets, so be careful! Basically what is happening is that as the liquid is squeezed out between the two surfaces, the cantilever resists this motion through the fluid and starts to bend. The severity of the bending will depend upon how viscous the fluid is and how fast the probe is moved through the fluid. Once the cantilever bends enough so that the 'Trigger Point' is reached, even if hard contact with the substrate is not yet made, the colloidal probe starts to retract. We can see from Fig. B.6 that only the trials that the 'Trigger Point' has been set to 9V and 10V provide a completely vertical line, meaning only in those two cases can we say the all the liquid has been squeezed out between the colloidal probe and substrate and the two surfaces are in hard contact. Therefore if a desired liquid is to be tested with a specified viscosity and specified spring of the colloidal probe is used, then there is a limit as to how fast the probe can be pushed through the fluid; if the maximum ± 10V deflection on the PSD is reached before hard contact with the substrate is made, then velocity of approach must be lowered (only the positive side of the PSD was used for these example tests, but the full 20V range can also be used). A stiffer spring constant can be used to lower the deflection of the cantilever; likewise, if a very low viscosity liquid is used a less stiff cantilever can be used to increase the deflection to obtain better sensitivity in the measurements. Also remember, the larger the colloidal probe used, the large the hydrodynamic force response will be.

Keep in mind that some colloidal probes will not provide a completely vertical line on the deflection vs. separation plot; this is either due to an improper InvOLS calibration or the colloidal probes do not behave according to Hooke's law. These cantilevers must be discarded, only colloidal probes that exhibit complete linearity during the full range of hard contact during the InvOLS calibration and also exhibit a completely vertical line when deflection vs separation is plotted are acceptable probes. These two conditions, along with the fact that a 2x2 μm area at the apex of the colloidal probe (positioned at $11^{o}$ during imaging, see Chapter 4) must have an atomically smooth surface free of asperities, will inevitably leave you with dozens of unacceptable colloidal probes and weeks of 8-12 hour days before you find a single good probe.

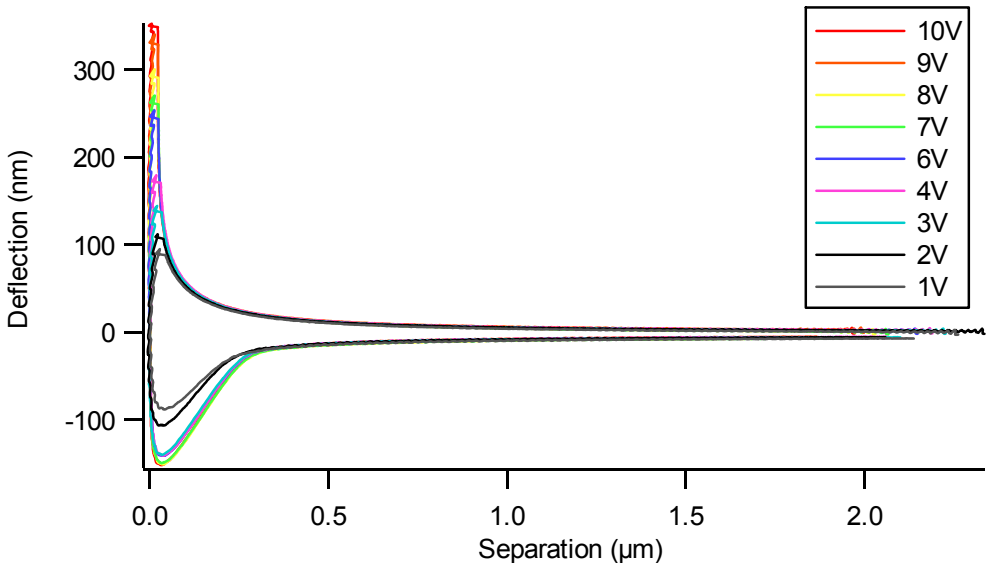


**Figure B.5: Fast approach Deflection vs. Separation in decanol (at 40 µm/s) after proper virtual deflection and InvOLS calibration close to the surface (at 0.5 µm/s). This Fig. shows the approach and retraction data after repeating a 'Single Force' in the same spot at different 'Trigger Point' values.**

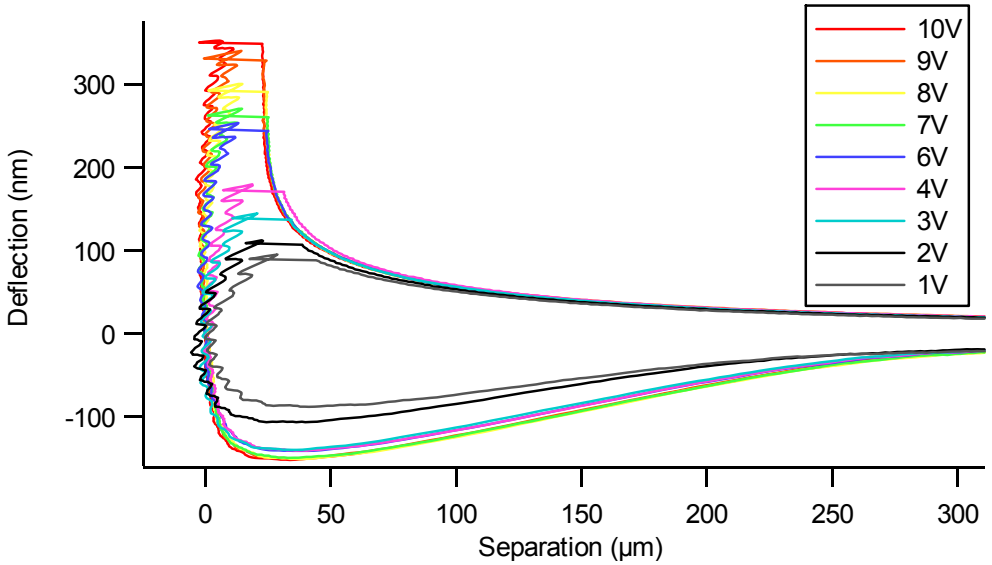


**Fig. B.6: Same Deflection vs. Separation data as Fig. B.5, just on a different scale.**

## B.4 Determining Offsets for Slip Length Measurements

Once 3 trials of accurate hydrodynamic force data in different spots on the substrate are obtained, the data may start to be analyzed for the appropriate slip length. Figs. B.7 and B.8 show the same deflection vs. separation data on different scales close to the surface using the 10V decanol data set from Fig. B.5 and B.6. Fig. B.7 was obtained by plotting def1 vs. sep1

(sep1 = defl - zpos1). Fig. B.8 is just a zoomed in version of Fig. B.7. The zero point marked on Figs. B.7 and B.8 is the natural interpretation by eye as to where the point of zero contact occurs. This is where the start of the vertical slope begins; thus, where the sphere and substrate first come into hard contact. At this point, it is suggested that the new student save their hydrodynamic data experiment and open the example experiment on the desktop of the AFM lab computer labeled 'Slip Length Example' and follow along. In this example, the viscosity is 10.750 mPas, the sphere diameter is 56.20 μm, and the colloidal probe spring constant is 1.22. You should determine this point of zero separation by eye for the example data provided. I have chosen an example for you. Next, click on the tab at the top of the screen labeled 'Sean's AFM Analysis'. Then select the tab labeled 'Force Curves'. Next select the tab labeled '2nd Experimental Force vs. Separation 4-7-08'. This will open a user interface that asks for the deflection and z-position data. These are the data sets you renamed defl1 and zpos1 for your data; I have provided you with them in this example. This interface also asks for the spring constant of the colloidal probe (this will be the spring constant you obtain using what you learn in this appendix and from the method given in Chapter 4). You can also add a z-position (or LVDT) and deflection offset to your data. The deflection offset will must likely always be used with z-position offsets used very seldom. For starters, use zero offsets for both and select 'Continue'. This program will automatically bring up a plot of the force data (which is simply the deflection data multiplied by the spring constant) as a function of the separation data (which is simply the deflection data *minus* the z-position data, theoretically this should be *plus* as discussed in Chapter 4, but based on the coordinates of the AFM software it has to be *minus*) with the zero point of contact determined. The program creates and names these waves ForceAppr1 and SeparationAppr1 (other useful waves are produced by this program; you can view them by using any drop down menu within any of the user interfaces). Going back to the previous example, the zero point of contact determined by the program in Fig. B.9 exactly matches that determined by eye in Fig. B.8 just from plotting the raw data; therefore, no additional z-offsets need to be added. If the program has difficulty determining the correct point of zero contact, the additional z-offset can be added into the program at this point so that the point of zero is correctly determined by the program (these added offsets will simply shift your data left or right depending upon the sign of the added offset). The zero you determine with your eye is the correct zero as long as the deflection data is a clearly vertical line; the program should

match or be adjusted to match this value determined by eye. No z-offset is needed in the example.

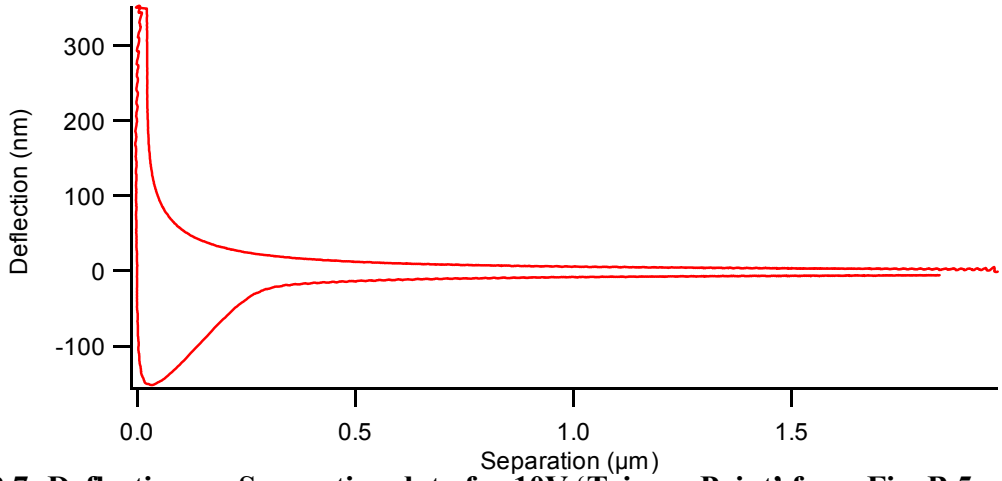


**Fig. B.7: Deflection vs. Separation data for 10V 'Trigger Point' from Fig. B.5 and Fig. B.6.**

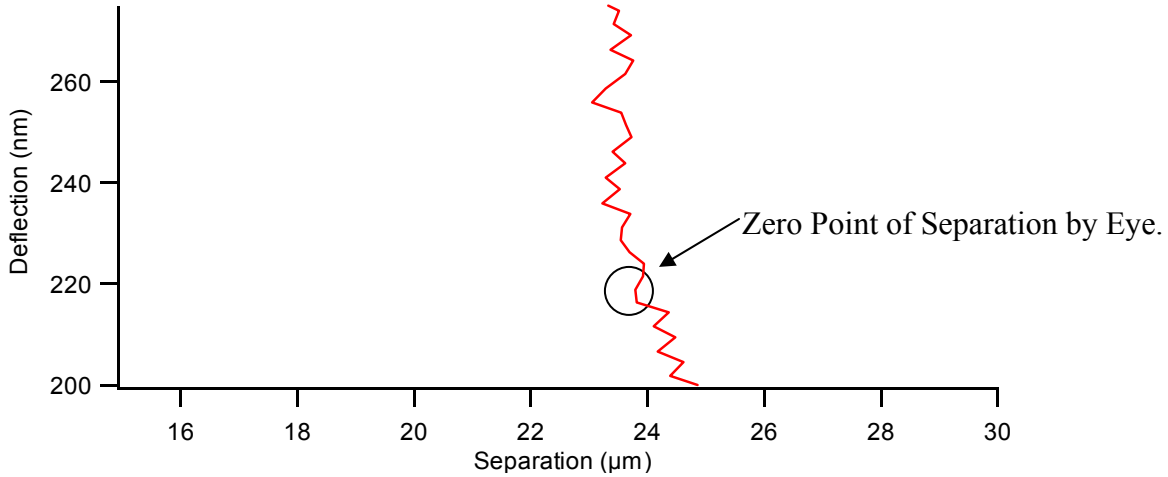


**Fig. B.8: Deflection vs. Separation data for 10V 'Trigger Point' from Fig. B.7.**

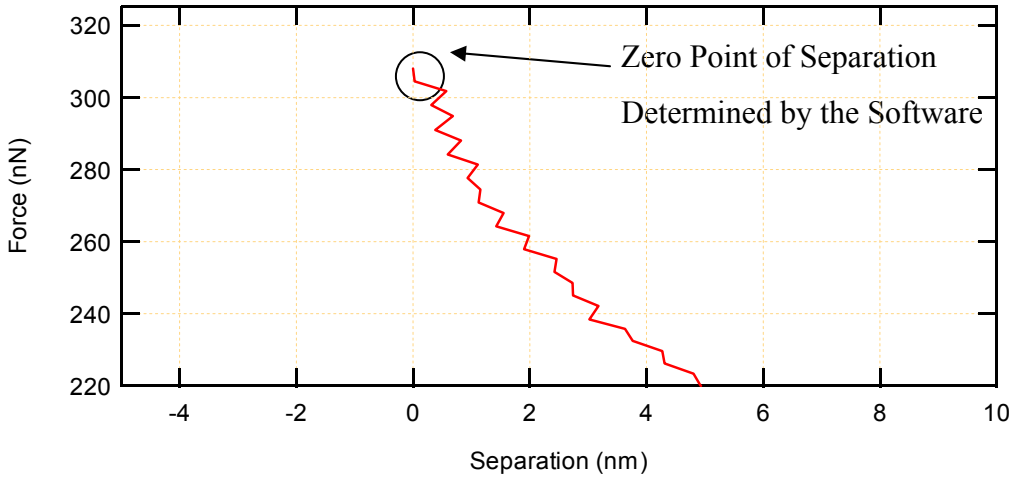


**Fig. B.9: Zero point of separation determined from software for the data in Fig. B.7 and Fig. B.8.**

Next, how to determine the correct deflection offset? Again, click on the tab at the top of the screen labed 'Sean's AFM Analysis'. Then select the tab labeled 'Hydrodynamics'. Next select the tab labeled '5th Calculate Slip Force 4-8-08'. This will open a user interface that asks for the deflection data (def1), z-position/LVDT data (zpos1), slip length, viscosity, diameter of colloidal probe, the spring constant of the colloidal probe, the added offsets, and whether the retraction data is used. Given our raw data, we want to find out what the corresponding Vinogradova theory data looks like for a near zero slip far from the surface. To generate this data we need to enter in 0.1 nm for the slip length. Enter the correct experimental viscosity based on temperature and diameter of the colloidal probe as discussed in Chapters 3 and 4. Enter zero for the retraction data option. Select def1 and zpos1 along with the appropriate z-offset if needed and the spring constant. Click 'Continue'. This will automatically bring up a new graph showing the z-offset corrected data still named ForceAppr1 vs SeparationAppr1, but now the Vinogradova slip theory for 0.1nm is also plotted on the graph. Far from the surface (zoom in to see this data), the slip length has little effect on the force; so, it is here that we want to compare the experimental data (ForceAppr1) to the theory data for 0.1nm of slip. See Fig. B10. There is no physical reason as to the offset of deflection of the experimental data (ForceAppr1) in the first program. The program simply assumes the first data point is at a deflection value of zero, this is not realistic. The point at which the experimental data oscillates around should be centered on the non-slip case (b = 0.1nm) far from the surface. For the example case provided a deflection offset is needed to center the experimental data on top of this theoretical data far from the surface (use the data range data point 0 to data point 258 to determine the offset for this example). This second program produces waves called Force1slip0.1nm. Now place the cursors on a 0.5 μm range of the force data in this new plot (0-258). Next, click on the tab at the top of the screen labed 'Sean's AFM Analysis'. Then select the tab labeled 'Hydrodynamics'. Next select the tab labeled 'Offset Code 4'. This will open a user interface that asks for the stick data (this is the wave Force1slip0.1nm just created from the second program), the force data (ForceAppr1), the separation data (SeparationAppr1), the estimated offset (usually 0.1nm works well for an initial guess), the spring constant of the colloidal probe, and if the cursors have been placed on the graph (enter '1' since they have been). When you click 'Continue' the program will determine the best deflection offset value for the range of experimental data you have chosen by the placement of the cursors. See Fig. B. 11. The value of the force offset is shown on the command

line following the notation ‘w_0 = force offset’, the number on the following line represents the deflection offset (7.93e-10). This offset is given by a positive number in the command line, but in reality this will be re-entered as a negative number in the first program of (-0.8  nm). You should have come up with this number or else you have done something wrong. The graph produced by this program can now be closed.

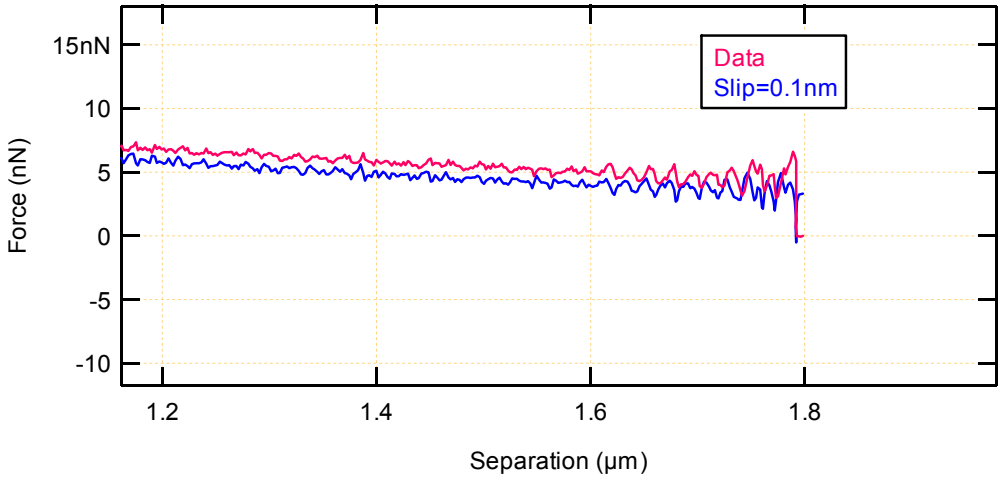


**Fig. B.10: Force vs. Separation data for ‘Slip Length Example’. Uncorrected data.**

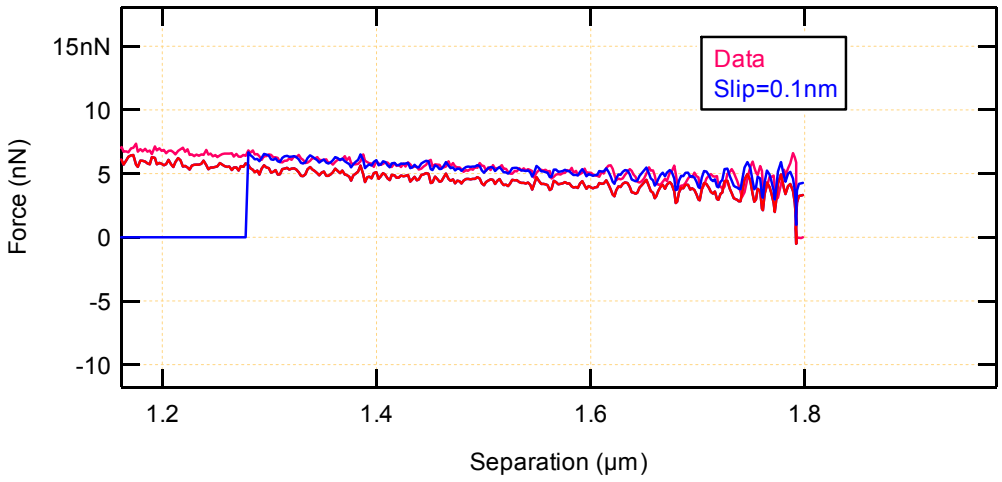


**Fig. B.11: Force vs. Separation data for ‘Slip Length Example’. Determining the deflection offset.**

Now, to make sure everything is correct, go back to the first program re-enter the requested data and the newly determined deflection offset as a negative number (along with the z-offset if needed), and click continue (this overwrites the existing data), re-open the second

program and repeat the same steps; the resulting graph should look like the following with the experimental and theoretical data centered on top of each other far from the surface. Do not close this graph.

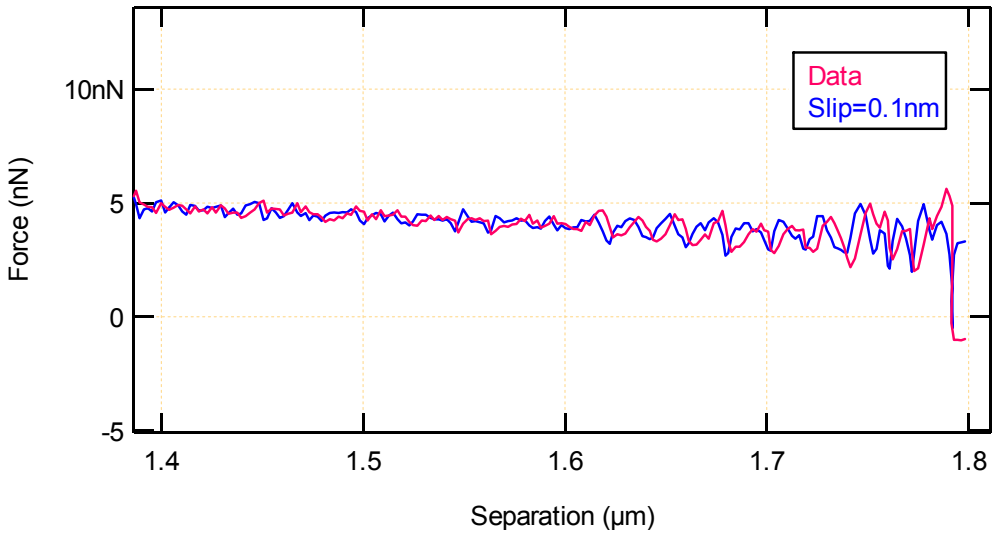


**Fig. B.12: Force vs. Separation data for 'Slip Length Example' after deflection offset.**

## B.5 Obtaining Accurate Slip Length Measurements

Once the correct offsets have been determined, the data can be analyzed for the slip length. On the previous graph created by the second program, place the cursors on the experimental data where you would like to analyze the slip length (usually anywhere from 2 μm to 10 nm from the surface works well). In this example the slip length is determined from data point 0 to data point 834. Next, click on the tab at the top of the screen labeled 'Sean's AFM Analysis'. Then select the tab labeled 'Hydrodynamics'. Next select the tab labeled '4$^{th}$ Fit Slip Using Levenberg-Marquardt Algorithum 4-8-08'. This will open a user interface that asks for the force data (ForceAppr1), separation data (separationAppr1), velocity data (velAData1), an initial guess for the slip length (usually 20 nm works well), the viscosity of the test liquid, the diameter of the colloidal probe, and whether cursors were placed on the data (enter '1' because they have been). The force data is the data is created by the first program with the correct offsets and is still named ForceAppr1; likewise for the separation (separationAppr1) and velocity data (velAData1). Simply select these from the drop down menus. Again, enter the correct experimental viscosity based on temperature and diameter of the colloidal probe as determined in

Chapters 3 and 4. Click ‘Continue’. The value of the slip length is shown on the command line following the notation ‘w_0 = slip length’. You should have obtained 17.9 nm for the slip length; if not, you have done something wrong. To generate a theoretical data set that corresponds to this slip length, close the existing graph, re-open the second program and keep everything the same, except this time you will enter the value of slip this program previously gave you (17.9 nm). The second program for this case will then generate the wave called Force1slip17.9nm and display it on a new graph with the experimental force data (ForceAppr1) with the corrected offsets, see Fig. B.13. It is this theoretical wave that is then compared to the experimental wave (ForceAppr1) in the Residual Calibration Method using different *k* values as discussed in Chapter 4.

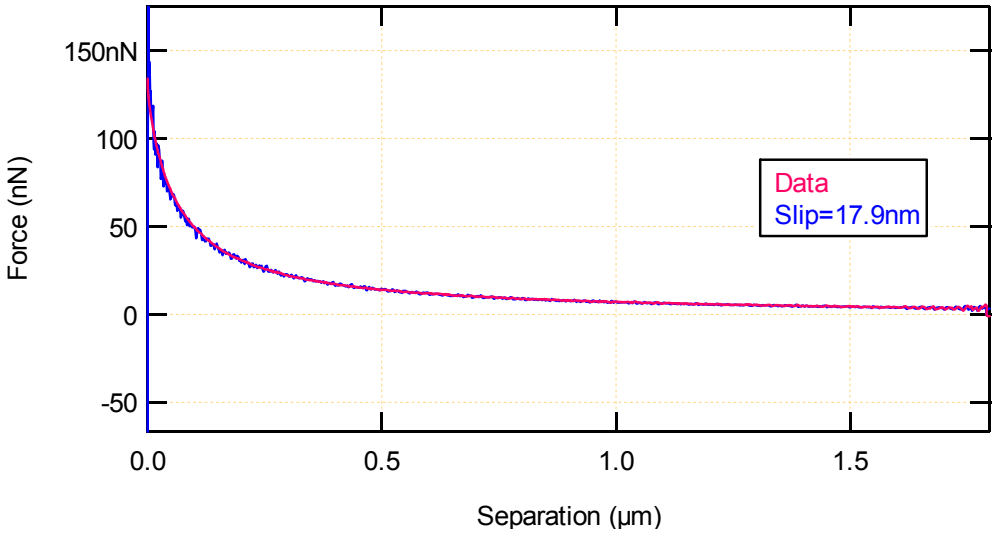


**Fig. B.13: Force vs. Separation data for ‘Slip Length Example’ after slip length determination.**

# Appendix C - Permission from Publishers to Include Previously Published Works

## C.1 – Physical Review E - American Physical Society - Copyright Permission

Dear Dr. McBride,

Thank you for your email. As the author, you have the right to use the article or a portion of the article in a thesis or dissertation without requesting permission from APS, provided the bibliographic citation and the APS copyright credit line are given on the appropriate pages.

Best wishes,
Eileen LaManca
Publications Marketing Coordinator
American Physical Society

---

From: "McBride, Sean" <seanpm@phys.ksu.edu>
Date: October 17, 2011 2:23:17 PM EDT
To: "help@aps.org" help@aps.org
Subject: Permission to Include My PRE Ariticle in My Dissertation

Kansas State University
Physics Department
Cardwell Hall Rm. 116
Manhattan, KS 66506-2601
785-249-6865
seanpm@phys.ksu.edu<mailto:seanpm@phys.ksu.edu><mailto:seanpm@phys.ksu.edu>

10-16-2011
To Whom It May Concern:

I am a doctoral student at Kansas State University and I am writing for permission to include in my dissertation all of the material from my article published in Physical Review E, Viscosity-dependent liquid slip at molecularly smooth hydrophobic surfaces 80, 060601(R), (2009). My dissertation will be made available online through the K-State Researc h Exchange (http://krex.ksu.edu). In addition, my dissertation will be microfilmed by UMI/ProQuest Information and Learning, and copies of the dissertation will be available for purchase.

Please supply a signed letter granting me permission to use the work. You can mail, email, or fax the permission (Fax: 785-532-6806).

Thank you for your assistance.
Sincerely,

Sean P. McBride

## C.2 – Review of Scientific Instruments – American Institute of Physics - Copyright Permission

Dear Dr. McBride:

Thank you for requesting permission to reproduce material from American Institute of Physics publications.

Permission is granted - subject to the conditions outlined below - for the following:

Review of Scientific Instruments,
Improved in situ spring constant calibration for colloidal probe atomic force microscopy, 81, 113703, (2010)

To be used in the following manner:

Reproduced in your dissertation for submission to Kansas State University. It is understood that the dissertation will be made available online through the K-State Research Exchange (http://krex.ksu.edu), and in addition, will be microfilmed by UMI/ProQuest Information and Learning, copies of which will be available for purchase.

1. The American Institute of Physics grants you the right to reproduce the material indicated above on a one-time, non-exclusive basis, solely for the purpose described. Permission must be requested separately for any future or additional use.

2. This permission pertains only to print use and its electronic equivalent, including CD-ROM or DVD.

3. The following copyright notice must appear with the material (please fill in the information indicated by capital letters): "Reprinted with permission from [FULL CITATION]. Copyright [PUBLICATION YEAR], American Institute of Physics."
Full citation format is as follows: Author names, journal title, Vol. #, Page #, (Year of publication).
For an article, the copyright notice must be printed on the first page of the article or book Chapter. For Fig.s, photographs, covers, or tables, the notice may appear with the material, in a footnote, or in the reference list.

4. This permission does not apply to any materials credited to sources other than the copyright holder.

Please let us know if you have any question.

Sincerely,
Susann Brailey

Manager, Rights and Permissions

Office of the Publisher, Journals and Technical Publications
American Institute of Physics
Suite 1NO1
2 Huntington Quadrangle
Melville, NY 11747-4502
Phone: 1-516-576-2268
Fax: 1-516-576-2450
Email: rights@aip.org

-----Original Message-----
From: McBride, Sean [mailto:seanpm@phys.ksu.edu]
Sent: Monday, October 17, 2011 1:21 PM
To: AIPRights Permissions
Subject: Permission to Include Paper in My Dissertation
Kansas State University
Physics Department
Cardwell Hall Rm. 116
Manhattan, KS 66506-2601

785-249-6865
seanpm@phys.ksu.edu<mailto:seanpm@phys.ksu.edu><mailto:seanpm@phys.ksu.edu>

10-16-2011
Office of Rights and Permissions
American Institute of Physics
Suite 1NO1, 2 Huntington Quadrangle
Melville, NY 11747-4502

To Whom It May Concern:

I am a doctoral student at Kansas State University and I am writing for permission to include in my dissertation all of the material from my article published in Review of Scientific Instruments, Improved in situ spring constant calibration for colloidal probe atomic force microscopy, 81, 113703, (2010). My dissertation will be made available online through the K-State Research Exchange (http://krex.ksu.edu). In addition, my dissertation will be microfilmed by UMI/ProQuest Information and Learning, and copies of the dissertation will be available for purchase.

Please supply a signed letter granting me permission to use the work. You can mail, email, or fax the permission (Fax: 785-532-6806).

Thank you for your assistance.

Sincerely,
Sean P. McBride

# Appendix D - Table of Contents of Supplementary Videos for Chapter 2

**Disk # 1**

1) Overall introduction
2) Introduction to leveling the AFM head
    - Leveling the active vibration table
        - Cleaning surfaces
    - Leveling standalone base
    - Environmental chamber notes
    - Explanation of gap between environmental chamber and AFM head
        - Problems with paper leveling
    - Overview of AFM controller, head, and environmental chamber components
    - Adjusting wheels on AFM head
        - Make marks on front wheels
    - Explanation of Staicmaster brushes and demo
    - Custom cantilever holder fo imaging colloidal probes
    - Hazardous storage and waste removal
        - Reminder to sign up for hazardous waste class and shop class
    - Inserting and removing cantilever holder from AFM head
    - Inserting and removing cantilever in cantilever holder

**Disk # 2**

- *Continuation of:* Inserting and removing cantilever in cantilever holder from disk 1
- Using the thermal method to determine if the cantilever is properly mounted (needed for both the colloidal probes and AC imaging tips)
    - Use the video feature to align the laser
    - How to use the objective microscope with the stand alone base
    - The sum and the deflection meter
    - Video of the laser spot on the backside of the cantilever
    - Thermal graph
- Using the AFM scanner protective lip and objective microscope plug protector
- Final tuning of active vibration scanner making the silicon substrate parallel to the AFM head prior to liquid insertion
- AET cleaning procedure for glassware
- Labeling and final product of silane coated surfaces
- Mounting AFM scanner protective lip
- EC cleaning of colloidal probe
- AET cleaning Needle and substrate

**Disk # 3**

- Vacuum drying all components
- Procedure for injecting liquid.
- Finally leveling the AFM head

3) Test to see if the right calibration liquid is used (vertical deflection vs. separation)
   - Decanol, which is too high viscosity for the probe used in the video

4) Sphere etching process
   - Basic set-up (heating water/dunce cap cover)
   - Modifications to colloidal probe holder

**Disk # 4**

- *Continuation of:* Sphere etching process
- Cantilever removal procedure

5) Colloidal probe assembly:
- UV61 glue application in inverted optical microscope set-up
- 3F-3Cl coated microscope slide
- Sphere drying process
- AC Mode imaging of the spheres on the slide
- Use of the transparency

**Disk # 5**

- Finding a good sphere/attaching a good sphere
- UV Curing

**Disk # 6**

- Finding a good sphere/attaching a good sphere
- UV Curing
- High Temperature oven programming and operation.
- Needed glassware and silane syringe cleaning procedure

**Disk # 7**

- Cleaning plasma cleaner chamber glass tube.
- Plasma cleaning and vacuum drying
- Transferring to toluene

# Appendix E - Procedure for Using Physical Vapor Deposition Chamber in Chemistry Department

1. Turn on the **water** to cool the **turbo pump**. This is the Blue value underneath the sink on the left side of the room. The value should be adjusted until water streams out of the two hoses and just dribbles out of the third hose.
2. Open **chamber vent** (chamber will take several minutes to reach atmosphere).
3. Lift **bell jar** and rotate to lock in the overhead position. Secure with wooden block just to be sure that bell jar will not fall down. It is irreplaceable.
4. Clean all surfaces inside the bell jar. **Be sure to only use clean tools washed with methanol, and do not drop anything through the screen. Always wear clean, powder-free gloves while working inside the chamber or while handling items to be placed in the chamber. Use methanol and paper towels/Kimwipes. If deposits from other runs are still present use the scouring pad with water to remove them.
5. Verify that all vacuum valves are closed on console (chamber vent closed).
6. Load samples into the chamber. Use the square glass slide with the circular holes cut out of them. Attach the cantilever with doubled sided tape so that the underside of the cantilever is halfway exposed over the hole. Note: the side that has the ball attached to it will be facing the top of the bell Jar. The aluminum will be evaporated on the cantilever from below.
7. Prepare Al ball using 18 inches Al wire. Wipe off Alumina coating with a Kimwipe and methanol and curl the ends. Then roll the wire at its center into a ball.
8. Install tungsten boat and Al ball on stage. Slightly tighten the screws. Note: each boat can be used up to three times if using the same material in each boat. Wrap the boats up in foil after you are done and the table and place on the table.
9. Make an Aluminum foil skirt to go all the way around the sample holder. The skirt can not touch the bottom electrode, nor can it get in the way of the shutter moving in and out. The skirt prevents Al from being deposited on the bell jar. The better the skirt the less mess one has to clean up in the end.
10. Make sure Al foil does not touch any metal support after repositioning Al skirt.
11. Close bell jar and chamber vent.
12. Turn **power** on at breaker box behind the instrument.
13. Power on the instrument with the **Main Power** switch located on the console.
14. Record the hours in the lab log book of operation of turbo pump.
15. Turn on the **Mechanical Pump** and start pumping out chamber by opening the **Rough Valve**.
16. Turn on Thermocouple Gauge.
17. Pump chamber below 50 millitorr on the **Thermocouple Gauge** (usually about 15 minutes).

18. Close **Rough Valve** and **open Back Valve** to pump on the back side of the turbo pump.
19. Pump until pressure is below 30 millitorr.
20. Press **Start** on turbo pump power supply.
21. Once the **Normal Operation** indicator lights up on the turbo pump power supply, slowly open the **Main Valve**.
22. Turn on the **Discharge Gauge** (943 HV on) to monitor the chamber pressure.
23. Turn to Zero and zero the discharge gauge with **zero knob**.
24. Turn to $10^{-4}$ and press **Vacuum Read** button.
25. Pump for 2 hours until pressure falls below 5x1 0-$^{5}$ Torr on the discharge gauge.
26. Fill the **Cryopump** with 1-2 liters of liquid nitrogen.
27. Wait for pressure drop below 5x1 $0^{-6}$ Torr, or less, before beginning deposition.

**Procedure foir Deposition**

1. Turn On Deposition Monitor.
2. Ensure that source shutter is in the closed position.
3. Turn Off Discharge Gauge.
4. Turn On **Filament Power**, do not exceed 200Amps. Normal operation 135Amps.
5. Turn **Filament Powerstat** up slowly, 3-5% every 1-2 minutes until 20%
6. Continue to turn Filament Powerstat 1-2% every 1 minute until metal melts.
7. Once metal melts, continue to turn Filament Powerstat up, about 1 % every 15 seconds until metal Wets and fills the sample boat. This is the point at which the aluminum is boiling. This can be observed as seeing the molten swirls in the metal beginning to move.
8. Begin deposition by increasing Filament Powerstat (35%-40%, should less than 40%), Zero deposition monitor, and open shutter . All three of these steps should be attempted to be as simultaneously as possible.
9. When desired thickness has been reached (either about 400 A, or less than 45 seconds), turn Filament Powerstat to 0, close shutter, and turn Off Filament Power.

**Procedure for Shutdown After Deposition is Complete**

1. Re-Zero and shut Off Deposition Monitor
2. Record thickness in log book
3. Turn Off Discharge Gauge and close Main Valve.
4. Wait 15 minutes.

5. Stop turbo pump.
6. Vent chamber remove sample and clean the bell jar.
7. After removing sample, close chamber Vent and close Backing Valve.
8. Open Rough Valve to pump down chamber to approximately 50 millitorr.
9. Turn off the Thermocouple Gauge and close Rough Valve.
10. Open Back Valve and let the mechanical pump run for 2-3 hours until the Cryopump warms back to room temperature.
11. Close Back Valve and turn Off Mechanical Pump
12. Turn off Main Power and shut off cooling water.

# References


1 S. P. McBride and B. M. Law, Phys. Rev. E **80** 060601 (R) (2009).

2 S. P. McBride and B. M. Law, Rev. Sci. Instrum. **81,** 113703 (2010).

3 S. P. McBride and B. M. Law, In preparation, soon to be submitted to Phys. Rev. Lett. or alternately Langmuir (2012).

4 B. Kaur, S. P. McBride, A. Paul, and W. T. Ford, Langmuir **26,** 15779-15785 (2010).

5 G. Paneru, P. S. Thapa, S. P. McBride, D. Moore-Nichols, and B. M. Law, Appl. Phys. Lett. **99,** 09302 (2011).

6 R. Seemann, M. Brinkmann, S. Herminghaus, K. Khare, B. M. Law, S. P. McBride, K. Kostourou, E. Gurevich, S. Bommer, C. Hermann, and D. Michler, J. Phys.: Condens. Matter **23,** 184108 (2011).

7 G. Paneru, S. P. McBride, B. M. Law, and B. N. Flanders, "Detection of cellular forces exerted by topside pseudopods." In Preparation. (2012).

8 http://www.bccresearch.com/report/SMC036C.html, Semiconductor Manufacturing, Microfluidics Technology, Report Code: SMC036C (2006, BBC September Research Report).

9 C. Habor, Lab on a Chip **6,** 1118-1121 (2006).

10 Y. Zhang, S. Park, S. Yang, and T. Wang, Biomed. Microdevices **12,** 1043 (2010).

11 N. A. M. Yunus and N. G. Green, Microsyst. Technol. **16,** 2099 (2010).

12 A. A. G. Bruzzone, H. L. Costa, P. M. Lonardo, and D. A. Lucca, CIRP Annals - Manufacturing Technol. **57,** 750-769 (2008).

13 S. Prakash, M. B. Karacor, and S. Banerjee, Surf. Sci. Rep. **64,** 233-254 (2009).

14 G. M. Whitesides, Nature **422,** 368-373 (2006).

15 F. K. Balagddé, L. You, C. L. Hansen, F. H. Arnold, and S. R. Quake, Science **309,** 137-140 (2005).

16 R. B. Fair, Microfluid Nanofluid **3,** 245-281 (2007).

17 D. J. Beebe, G. A. Mensing, and G. M. Walker, Annu. Rev. Biomed. Eng. **4,** 261-286 (2002).

18 R. B. Fair, A. Khlystov, T. D. Tailor, V. Ivanov, R. D. Evans, P. B. Griffin, V. Srinvasan, V. K. Pamula, M. G. Pollack, and J. Zhou, Design and Test of Computers, IEEE **24,** 10-24 (2007).

19 D. B. Weibel and G. M. Whitesides, Curr. Opin. Chem. Bio. **10,** 584-591 (2006).

20 J. Melin and S. R. Quake, Annu. Rev. Biophys. Biomol. Struct. **36,** 213-231 (2007).

21 V. Srinvasan, V. K. Pamula, and R. B. Fair, Lab Chip **4,** 310-315 (2004).

22 C. H. Ahn, J.-W. Choi, G. Beaucage, J. H. Nevin, J.-B. Lee, A. Puntambekar, and J. Y. Lee, Proc. IEEE **92,** 154-173 (2004).

23 P. Yager, G. J. Domingo, and J. Gerdes, Annu. Rev. Biomed. Eng. **10,** 107-144 (2008).

24 C.-H. H. Choi, U. Ulmanella, J. Kim, C. M. Ho, and C. J. Kim, Phys. Fluids **18,** 08105 (2006).

25 J. Eijkel, Lab Chip **7,** 299-301 (2007).

26 T. Sochi, arXiv:1101.4421v1 (2011).

[27] E. Lauga, M. P. Brenner, and H. A. Stone, *Handbook of Experimental Fluid Dynamics, Chapter 19, Microfluidics: The No-Slip Boundary Condition* (Springer, New York, 2007).
[28] C. Neto, D. R. Evans, E. Bonaccurso, H.-J. Butt, and V. S. J. Craig, Rep. Prog. Phys. **68,** 2859-2897 (2005).
[29] O. I. Vinogradova, Int. J Miner. Process **56,** 31-60 (1999).
[30] J. S. Ellis and M. Thompson, Phys. Chem. Chem. Phys. **6,** 4928-4938 (2004).
[31] S. Granick, Y. Zhu, and H. Lee, Nat. Mater. **2,** 221-227 (2003).
[32] H. Spikes and S. Granick, Langmuir **19,** 5065-5071 (2003).
[33] C. H. Choi, J. A. Westin, and K. Breuer, Phys. Fluids **15,** 2897-2902 (2003).
[34] J.-L. Barrat and L. Bocquet, Physical Review Letters **82,** 4671 (1999).
[35] D. M. Huang, C. Sendner, D. Horinek, R. R. Netz, and L. Bocquet, Phys. Rev. Lett. **101,** 226101 (2008).
[36] C. Cottin-Bizonne, A. Steinberger, B. Cross, O. Raccurt, and E. Charlaix, Langmuir **24,** 1165-1172 (2008).
[37] Y. Zhu and S. Granick, Physical Review Letters **87,** 096105 (2001).
[38] R. Pit, H. Hervet, and L. Leger, Physical Review Letters **85,** 980-983 (2000).
[39] Y. Zhu and S. Granick, Physical Review Letters **88,** 106102 (2002).
[40] D. Quére, Annu. Rev. Mater. Res. **38,** 71-99 (2008).
[41] P. Joseph and P. Tabeling, Physical Review E **71,** 035303 (2005).
[42] D. C. Tretheway and C. Meinhart, Physics of Fluids **14,** L9-L12 (2002).
[43] S. Lichter, A. Roxin, and S. Mandre, Phys. Rev. Lett. **93,** 086001 (2003).
[44] D. Andrienko, B. Dunweg, and O. I. Vinogradova, Chem. Phys. **119,** 13106 (2003).
[45] D. C. Tretheway and C. Meinhart, Physics of Fluids **16,** 1509 -1515 (2004).
[46] P. A. Thompson and M. O. Robbins, Phys. Rev. A **41,** 6830 (1990).
[47] G. Sun, E. Bonaccurso, V. Franz, and H.-J. Butt, J. Chem. Phys. **117,** 10311-10314 (2002).
[48] E. Bonaccurso, H.-J. Butt, and V. S. J. Craig, Phys. Rev. Lett. **90,** 144501 (2003).
[49] O. I. Vinogradova and A. V. Belyaev, Submtted to: J. Phys.: Condens. Matter (arXiv:1009.4772v3) (2011).
[50] D. Gérard-Varet and M. Hillairet, (arXiv: 1103.0864v1) (2011).
[51] S. Guriyanova, B. Semin, T. S. Rodriques, H.-J. Butt, and E. Bonaccurso, Microfluid Nanofluid **8,** 653-663 (2010).
[52] V. S. J. Craig, C. Neto, and D. R. M. Wiliams, Phys. Rev. Lett. **87,** 054504 (2001).
[53] C. D. F. Honig and W. A. Ducker, Phys. Rev. Lett. **98,** 028305 (2007).
[54] A. Martini, H.-Y. Hsu, N. A. Patankar, and S. Lichter, Phys. Rev. Lett. **100,** 206001 (2008).
[55] N. V. Priezjev and S. M. Troian, Physical Review Letters **92,** 018302 (2004).
[56] C. Neto, V. S. J. Craig, and D. R. M. Williams, Eur. Phys. J. E **12,** S71-S74 (2003).
[57] P. A. Thompson and S. M. Troian, Nature **389,** 360-362 (1997).
[58] P. G. de Gennes, Langmuir **18,** 3413-3414 (2002).
[59] E. Lauga and H. A. Stone, Fluid Mechanics **489,** 55-77 (2003).
[60] N. Ishida, T. Inoue, M. Miyahara, and K. Higahitani, Langmuir **16,** 6377-6380 (2000).
[61] J. W. G. Tyrell and P. Attard, Phys. Rev. Lett. **87,** 176104 (2001).
[62] C. H. Choi and C. J. Kim, Phys. Rev. Lett. **96,** 066001 (2006).
[63] J. Hyväluoma, C. Kunert, and J. Harting, J. Phys.: Condens. Matter **23,** 184106 (2011).

[64] T. Schmatko, H. Hervet, and L. Leger, Phys. Rev. Lett. **94,** 244501 (2005).
[65] J.-H. J. Cho, B. M. Law, and F. Rieutord, Phys. Rev. Lett. **92,** 166102 (2004).
[66] X. Gu and M. Chen, Appl. Phys. Lett. **99,** 063101 (2011).
[67] E. S. Asmolov, A. V. Belyaev, and O. I. Vinogradova, Phys. Rev. E **84,** 026330 (2011).
[68] O. I. Vinogradova, Langmuir **11,** 2213-2220 (1995).
[69] J. N. Israelachvili, *Intermolecular and surface forces*, second ed. (Academic Press, London, 1991).
[70] A. P. Bowles, C. D. F. Honig, and W. A. Ducker, J. Phys. Chem. C **115,** 8613-8621 (2011).
[71] W. A. Ducker, T. J. Senden, and R. M. Pashley, Nature **353,** 239-241 (1991).
[72] E. Ruckenstein and P. Rajora, J. Colloid Interface Sci. **96,** 488-491 (1983).
[73] C. D. F. Honig and W. A. Ducker, J. Phys. Chem. C **114,** 20114-20119 (2010).
[74] L. Zhu, P. Attard, and C. Neto, Langmuir **27,** 6701-6711 (2011).
[75] L. Zhu, P. Attard, and C. Neto, Langmuir **27,** 6712-6719 (2011).
[76] N. Asproulis and D. Drikakis, Phys. Rev. E **84,** 031504 (2011).
[77] N. V. Priezjev, Phys. Rev. E **85** (2010).
[78] G. Binnig, C. F. Quate, and C. Gerber, Phys. Rev. Lett. **56,** 930-933 (1986).
[79] G. Binnig, C. Gerber, E. Stoll, T. R. Albrecht, and C. F. Quate, Europhys. Lett. **3,** 1281-1286 (1987).
[80] J. P. Cleveland, S. Manne, D. Bocek, and P. K. Hansma, Rev. Sci. Instrum. **64,** 403-405 (1993).
[81] J. L. Hutter and J. Bechhoefer, Rev. Sci. Instrum. **64,** 1868-1873 (1993).
[82] J. E. Sader and L. White, J. Appl. Phys. **74,** 1-9 (1993).
[83] J. E. Sader, P. Mulvaney, I. Larson, and L. R. White, Rev. Sci. Instrum. **66,** 3789-3797 (1995).
[84] J. E. Sader, J. Appl. Phys. **84,** 64-76 (1998).
[85] J. E. Sader, J. W. M. Chon, and P. Mulvaney, Rev. Sci. Instrum. **70,** 3967-3969 (1999).
[86] S. A. Edwards, W. A. Ducker, and J. E. Sader, J. Appl. Phys. **103,** 064513-064513 (2008).
[87] V. S. J. Craig and C. Neto, Langmuir **17,** 6018-6022 (2001).
[88] R. Fuierer, (Asylum Research, Procedural Operation 'Manualette' Beta Version 10, Based on software version 080501, http://nano.indiana.edu/Files/MFP3D/MFP3D%20Manual2.pdf, 2008).
[89] H. Brenner, Chem. Eng. Sci. **16,** 242-251 (1961).
[90] R. Chatchaidech, Thesis, Virginia Polytechnic Institute and State University, 2011.
[91] R. D. Gretz, Suface Science **5,** 239-251 (1966).
[92] A. Scheludko, B. V. Toshev, and D. Platikanov, in *The Modern Theory of Capillarity: To the Centennial of Gibbs Theory of Capillarity*, edited by F. C. Goodrich, A. I. Rusanov, H. Sontag, and M. Bülow (Akademie-Verlag, Berlin, 1981), p. 163-182.
[93] I. B. Ivanov, P. A. Kralchevsky, and A. D. Nikolov, J. Colloid Interface Sci. **112,** 97-107 (1986).
[94] R. Aveyard, B. D. Beake, and J. H. Clint, J. Chem. Soc., Faraday Trans. **92,** 4271-4277 (1996).
[95] R. Aveyard, J. H. Clint, and T. S. Horozov, Phys. Chem. Chem. Phys. **5,** 2398-2409 (2003).

[96] J. W. Gibbs, *The Scientific Papers of J. Willard Gibbs*, Vol. 1 (Ox Bow Press, Connecticut, 1961).
[97] A. I. Rusanov, Surf. Sci. Rep. **58,** 111-239 (2005).
[98] A. Scheludko, B. V. Toshev, and D. T. Bojadjiev, J. Chem. Soc., Faraday Trans. I **72,** 2815-2828 (1976).
[99] L. Brinon, S. Geiger, V. Alard, Jean-François, T. Pouget, and G. Couarraze, J. Cosmet. Sci. **49,** 1-11 (1998).
[100] E. Dickinson, *An Introduction to Food Colloids* (Oxford University Press, New York, 1992).
[101] D. Rousseau, Food Res. Int. **33,** 3-14 (2000).
[102] A. Yusoff and B. S. Murray, Food Hydrocoll. **25,** 42-55 (2011).
[103] G. H. Sager, M. A. Arunagirinathan, and J. R. Bellare, Indian J. Exp. Biol. **45,** 133-159 (2007).
[104] P. Shah, D. Bhalodia, and P. Shelat, Sys. Rev. Parm. **1,** 24-32 (2010).
[105] Y.-N. Wu, D.-H. Chen, X.-Y. Shi, C.-C. Lian, Y.-Y. Wang, C.-S. Yeh, K. R. Ratinac, P. Thordarson, F. Braet, and D.-B. Shieh, Nanomedicine: Nanotech. Biol. Med. **DOI:10.1016/j.nano.2011.01.002** (2011).
[106] H. Xin, X. Jiang, J. Giu, X. Sha, L. Chen, K. Law, Y. Chen, X. Wang, Y. Jiang, and X. Fang, Biomaterials **DOI:10.1016/j.biomaterials.2011.02.044,** 1-13 (2011).
[107] D. J. Irvine, Nat. Mater. **10,** 342-343 (2011).
[108] H. S. Wi, S. Cingarapu, K. J. Klabunde, and B. M. Law, Langmuir **DOI: 10.1021/la201791g** (2011).
[109] S. Herminghaus, A. Frey, and D. Reim, Ultramicroscopy **69,** 211-217 (1997).
[110] T. Pompe, A. Frey, and S. Herminghaus, Langmuir **10,** 2585-2588 (1998).
[111] W. A. Gifford and L. E. Scriven, Chem. Eng. Sci. **26,** 287-297 (1971).
[112] D. Y. Chan, J. D. Henry, and L. R. White, J. Colloid Interface Sci. **79,** 410-418 (1981).
[113] M. A. Fortes, Can. J Chem. **60,** 2889-2895 (1982).
[114] V. N. Paunov, P. A. Kralchevsky, N. D. Denkov, and K. Nagayama, J. Colloid Interface Sci. **157,** 100-112 (1993).
[115] P. A. Kralchevsky and K. Nagayama, Adv. Colloid Interface Sci. **85,** 145-192 (2000).
[116] P. A. Kralchevsky and N. D. Denkov, Curr. Opin. Colloid Interface Sci. **6,** 383-401 (2001).
[117] J. Faraudo and F. Bresme, J. Non-Equilib. Thermodyn. **29,** 397-404 (2004).
[118] L. Dong and D. T. Johnson, Langmuir **21,** 3838-3849 (2005).
[119] F. Bresme, Eur. Phys. J. B **64,** 487-491 (2008).
[120] H. Lehle, E. Noruzifar, and M. Oettel, Eur. Phys. J. E **26,** 151-160 (2008).
[121] J. C. Loudet, A. M. Alsayed, J. Zhang, and A. G. Yodh, Phys. Rev. Lett. **94,** 018301 (2005).
[122] J. Faraudo and F. Bresme, J. Chem. Phys. **118,** 6518-6528 (2003).
[123] C. A. Bearchell, D. M. Heyes, D. J. Moreton, and S. E. Taylor, Phys. Chem. Chem. Phys. **3,** 4774-4783 (2001).
[124] E. Noruzifar and M. Oettel, Phys. Rev. E **79,** 051401 (2009).
[125] H. Lehle, M. Oettel, and S. Dietrich, Eur. Phys. Lett. **75,** 174-180 (2006).
[126] H. Lehle and M. Oettel, Phys. Rev. E **75,** 011602 (2007).
[127] H. Lehle and M. Oettel, J. Phys.: Condens. Matter **20,** 10 (2008).
[128] D. Stamou and C. Duschl, Phys. Rev. E **62,** 5263-5272 (2000).

[129] P. A. Kralchevsky, N. D. Denkov, and K. D. Danov, Langmuir **17,** 7694-7705 (2001).
[130] K. D. Danov, P. A. Kralchevsky, B. N. Naydenov, and G. Brenn, J. Colloid Interface Sci. **287,** 121-134 (2005).
[131] K. L. Babcock and C. B. Prater, (Veeco Instrumets Inc., *Phase Imaging: Beyond Topography,* Santa Barbra, CA, 2004).
[132] Due to thermal drift of the x-y stage during imaging, accuracy of the RMS surface roughness measurements on the 50 nm by 50 nm available areas of the small spherical caps is limited.
[133] F. Bresme and M. Oettel, J. Phys.: Condens. Matter **19,** 413101 (2007).
[134] F. Behroozi, B. Lambert, and B. Buhrow, Appl. Phys. Lett. **78,** 2399-2401 (2001).
[135] T. G. Fox and P. J. Flory, J. Appl. Phys. **21,** 581-591 (1950).
[136] K. Khare, Thesis, Max Planck Institute, Göttingen, Germany, 2007.
[137] H. B. Weiser, *Inorganic Colloid Chemistry*, Vol. 1-3 (John Wiley and Sons, New York, 1933, 1935, 1938).
[138] H. B. Weiser, *Colloid Chemistry*, 2nd ed. (John Wiley and Sons, New York, 1949).
[139] J. T. Davies and E. K. Rideal, *Interfacial Phenomena* (Academic Press, New York, 1961).
[140] D. J. Shaw, *Introduction to Colloid and Surface Chemistry*, 2nd ed. (Butterworths & Co. Ltd., London, 1970).
[141] A. W. Adamson, *Physical Chemistry of Surfaces*, 3rd ed. (John Wiley and Sons, New York, 1976).
[142] F. C. Goodrich, A. I. Rusanov, H. Sontag, and M. Bülow, Eds., *The modern Theory of Capillarity. The Centennial of Gibbs' Theory of Capillarity.* (Akademie-Verlag, Berlin, 1981).
[143] P.-Å. Albertsson, *Partition of Cell Particles and Macromolecules*, 3rd ed. (John Wiley and Sons, New York, 1986).
[144] W. B. Russel, D. A. Saville, and W. R. Schowalter, *Colloidal Dispersions* (Cambridge University Press, Cambridge, 1989).
[145] A. W. Neumann and J. K. Spelt, *Applied Surface Thermodynamics*, Vol. 63 (Marcel Dekker, Inc., New York, 1996).
[146] B. P. Binks, *Modern Aspects of Emulsion Science* (The Royal Society of Chemistry, Cambridege, UK, 1998).
[147] K. Esumi, *Polymer Interfaces and Emulsions* (Marcel Dekker, Inc., New York, 1999).
[148] P. A. Kralchevsky and K. Nagayama, *Particles at Fluid Interfaces and Membranes: Attachment of Colloid Particles and Proteins to Interfaces and Formation of Two-Dimesional Arrays*, Vol. 10 (Elsevier, Amsterdam, 2001).
[149] J. S. Rowlinson and B. Widom, *Molecular Theory of Capillarity* (Dover Publications, Inc., Mineola, New York, 2002).
[150] H.-J. Butt, K. Graf, and M. Kappl, *Physics and Chemistry of Interfaces* (Wiley/VCH Berlin, 2003).
[151] R. M. Pashley and M. E. Karaman, *Applied Colloid and Surface Chemistry* (John Wiley and Sons, The Atrium, Southern Gate, Chichester, West Sussex PO19 8SQ, England, 2004).
[152] B. P. Binks and T. S. Horozov, *Colloidal Particles at Liquid Interfaces* (Cambridge University Press, Cambridge, 2006).

[153] K. T. Ranjit and K. J. Klabunde, in *Kent and Riegel's Handbook of Industrial Chemistry and Biotechnology*, 11th ed., edited by J. A. Kent (Springer, Boston, MA, 2007), p. 328-344.
[154] K. J. Klabunde and R. M. Richards, *Nanoscale Materials in Chemistry*, 2nd ed. (John Wiley and Sons, Hoboken, New Jersey, 2009).
[155] W. Norde, *Colloids and Interfaces in Life Sciences and Bionanotechnology* (CRC Press, Boca Raton, FL., 2011).
[156] A. Amirfazli and A. W. Neumann, Adv. Colloid Interface Sci. **110,** 121-141 (2004).
[157] M. E. Flatte, A. A. Kornyshev, and M. Urbakh, J. Phys.: Condens. Matter **20,** 073102 (2008).
[158] A. V. Nguyen and H. J. Schulze, *Colloidal Science of Flotation*, Vol. 118 (Marcel Dekker, Inc., New York, 2004).
[159] (First Ten Angstroms, FTA 100 Series, User Manual: Drop Shape Analysis, http://www.firsttenangstroms.com, 2002).
[160] G. Meyer and N. M. Amer, Appl. Phys. Lett. **53,** 1045-1047 (1988).
[161] R. A. Wilson and H. A. Bullen, *Introduction to Scanning Probe Microscopy (SPM): Basic Theory; Atomic Force Microscope (AFM), http://asdlib.org/onlineArticles/ecourseware/Bullen/SPMModule_BasicTheoryAFM.pdf ,* (Department of Chemistry, Northern Kentucky).
[162] J. E. Lennard-Jones, in *Cohesion, The Proceedings of The Physical Society, Vol. 43, Part 5, No. 240*, 1931, p. 461-482.
[163] H. Margenau, Rev. Mod. Phys. **11,** 1-35 (1939).
[164] D. Y. Abramovitch, S. B. Andrsson, L. Y. Pao, and G. Schitter, in *A Tutorial on the Mechanisms, Dynamics, and Control of Atomic Force Microscopes, Proceedings of the American Control Conference*, Marriott Marquis Hotel at Times Square, 2007.
[165] (NRD, LLC., http://www.amstat.com/solutions/staticmaster.html, & http://www.nrdstaticcontrol.com/, 2011).
[166] (Webster's Online Dictionary: http://www.websters-online-dictionary.org/definitions/Polonium, 2011).
[167] J. M. Neumeister and W. A. Ducker, Rev. Sci. Instrum. **65,** 2527-2531 (1994).
[168] J. Mingins and A. Scheludko, J. Chem. Soc., Faraday Trans. **75,** 1-6 (1979).
[169] R. Aveyard and J. H. Clint, J. Chem. Soc., Faraday Trans. **91,** 2681-2697 (1995).
[170] B. P. Binks and S. O. Lumsdon, Langmuir **16,** 8622-8631 (2000).
[171] V. N. Paunov, Langmuir **19,** 7970-7976 (2003).
[172] R. A. W. Dryfe, Phys. Chem. Chem. Phys. **8,** 1869-1883 (2006).
[173] D. O. Grigoriev, J. Krägel, V. Dutschk, R. Miller, and H. Möhwald, Phys. Chem. Chem. Phys. **9,** 6447-6454 (2007).
[174] J. Mi, Y. He, and C. Zhong, AIChE Journal **55,** 747-755 (2009).
[175] T. T. Chau, W. J. Bruckard, P. T. L. Koh, and A. V. Nguyen, Adv. Colloid Interface Sci. **150,** 106-115 (2009).
[176] M. Zeng, J. Mi, and C. Zhong, Phys. Chem. Chem. Phys. **13,** 3932-3941 (2011).
[177] K. P. Oza and S. G. Frank, J. Disp. Sci Technol. **7,** 543-561 (1986).
[178] W. Jahn and R. Stry, J. Phys. Chem. **92,** 2294-2301 (1988).
[179] J. Li and K. D. Caldwell, J. Pharm. Sci **83,** 1586-1592 (1994).
[180] B. R. Midmore, Coll. Surf. A **145,** 133-143 (1998).

[181] J. Vermant, G. Cioccolo, K. Golapan Nair, and P. Moldenaers, Rheol. Acta. **43,** 529-538 (2004).
[182] E. Dressaire, R. Bee, D. C. Bell, A. Lips, and H. A. Stone, Science **320,** 1198-1201 (2008).
[183] M. Borden, Soft Matter **5,** 716-720 (2009).
[184] J. H. M. Willison and A. J. Rowe, *Freeze etching techniques*, Vol. 8 (Elsevier/North Holland Biomedical Press, Amsterdam, 1980).
[185] E. Sjöblom and S. Friberg, J. Colloid Interface Sci. **67,** 16-30 (1978).
[186] J. Kuntsche, J. C. Horst, and H. Bunjes, Int. J. Pharm. **DOI:10.1016/j.ijpharm.2011.02.001** (2011).
[187] E. Engel and C. Colliex, Curr. Opin. Biotechnol. **4,** 403-411 (1993).
[188] S. B. Andrews and R. D. Leapman, Microsc. Anal. **36,** 19-22 (1993).
[189] C. Colliex and C. Mory, Biol. Cell **80,** 175-180 (1994).
[190] B. P. Binks and M. Kirkland, Phys. Chem. Chem. Phys. **4,** 3727-3733 (2002).
[191] G. D. Danilatos, Microsc. Res. Tech. **25,** 354-361 (1993).
[192] L. Muscariello, F. Rosso, G. Marino, A. Giordano, M. Barbarisi, G. Cafiero, and A. Barbarsi, J. Cell. Phys. **205,** 328-334 (2005).
[193] M. Brugnara, C. Della Volpe, S. Sinboni, and D. Zeni, Scanning **28,** 267-273 (2006).
[194] S. E. Kirk, J. N. Skepper, and A. M. Donald, J. Microscopy **233,** 205-224 (2009).
[195] K. K. Varanasi, M. Hsu, N. Bhate, W. Yang, and T. Deng, Appl. Phys. Lett. **95,** 094101 (2009).
[196] R. G. Matthews and A. M. Donald, Scanning **24,** 75-85 (2002).
[197] A. Bogner, G. Thollet, D. Basset, P. H. Jouneau, and C. Gauthier, Ultramicroscopy **104,** 290-301 (2005).
[198] Z. Barkay, Appl. Phys. Lett. **96,** 183109 (2010).
[199] A. K. F. Dyab and V. N. Paunov, Soft Matter **6,** 2613-2615 (2010).
[200] I. Barshack, J. Kpolovic, Y. Chowers, O. Gileadi, A. Vainshtein, O. Zik, and V. Behar, Ultrastruct. Pathol. **28,** 29-31 (2004).
[201] A. Bogner, P. H. Jouneau, G. Thollet, D. Basset, and C. Gauthier, Micron **38,** 390-401 (2007).
[202] R. McIntosh, D. Nicastro, and D. Mastronarde, Trends Cell Biol. **15,** 43-51 (2005).
[203] M. F. Hohmann-Marriott, A. A. Sousa, A. A. Azari, S. Glushakova, G. Zhang, J. Zimmerberg, and R. D. Leapman, Nat. Meth. **6** (2009).
[204] M. O. Gallyamov, Macromol. Rapid. Commun. **DOI: 10.1002marc.201100150** (2011).
[205] N. A. Stelmashenko, J. P. Craven, A. M. Donald, E. M. Terentjev, and B. L. Thiel, J. Microscopy **204,** 172-183 (2001).
[206] A. A. Sousa, M. A. Aronova, Y. C. Kim, L. M. Dorward, G. Zhang, and R. D. Leapman, J. Struct. Biol. **159,** 507-522 (2007).
[207] T. Nei, J. Microscopy **99,** 227-233 (1973).
[208] K. R. Miller, C. S. Prescott, T. L. Jacobs, and N. L. Lassignal, J. Ultrastruct. Res. **82,** 123-133 (1983).
[209] R. J. Mikula and V. A. Munoz, Coll. Surf. A. **174,** 23-36 (2000).
[210] J. Dubochet, Q. Rev. Biophys. **21,** 129-228 (1988).
[211] X. H. Zhang and W. A. Ducker, Langmuir **23,** 12475-12480 (2007).
[212] X. H. Zhang and W. A. Ducker, Langmuir **24,** 110-115 (2008).

[213] H. A. Rinia, M. M. E. Snel, van der Ewrden, P. J. M. , and B. de Kruijff, FEBS Lett. **501,** 92-96 (2001).
[214] D. E. Saslowsky, J. Lawrence, X. Ren, D. Brown, R. M. Henderson, and J. M. Edwardson, J. Bio. Chem. **277,** 26966-26970 (2002).
[215] K. Simons and W. L. C. Vaz, Ann. Rev. Biophys. Biomolec. Struct. **33,** 269-295 (2004).
[216] S. D. Connell and A. Smith, Mol. Membr. Biol. **23,** 17-28 (2006).
[217] Z. Leonenko, D. Cramb, M. Amrein, and E. Finot, in *Applied Scanning Probe Methods IX*, edited by B. Bhushan, A. Fuchs, and M. Tomitori (Springer-Verlag, Berlin-Hiedelberg, 2008), p. 207-234.
[218] K. Mulligan, D. Brownholland, A. Carnini, D. H. Thmpson, and L. J. Johnston, Langmuir **26,** 8525-8533 (2010).
[219] K. El Kirat, S. Morandat, and Y. F. Dufrêne, Biochim. Biophys. Acta. **1798,** 750-765 (2010).
[220] F. Bresme, H. Lehle, and M. Oettel, J. Chem. Phys. **130,** 214711 (2009).
[221] G. Andreatta, J. Cousty, and J.-J. Benattar, Chem. Commun. **47,** 3571-3573 (2011).
[222] R. S. Gates and M. G. Reitsma, Rev. Sci. Instrum. **78,** 086101 (2007).
[223] L. Gao and T. J. McCarthy, Langmuir **22,** 6234-6237 (2006).
[224] E. Lauga, M. P. Brenner, and H. A. Stone, edited by J. Foss, C. Tropea, and A. Yarin (Springer, New York, 2005).
[225] T. M. Squires and S. R. Quake, Rev. Mod. Phys. **77,** 977-1026 (2005).
[226] C. Cottin-Bizonne, B. Cross, A. Steinberger, and E. Charlaix, Phys. Rev. Lett. **94** (2005).
[227] C. I. Bouziques, L. Bocquet, E. Charlaix, C. Cottin-Bizonne, B. Cross, L. Joly, A. Steinberger, C. Ybert, and P. Tabeling, Philosophical Transactions of the Royal Society A. **366,** 1455-1468 (2008).
[228] E. Lauga and M. P. Brenner, Phys. Rev. E **70,** 026311 (2004).
[229] A. Steinberger, C. Cottin-Bizonne, P. Kleimann, and E. Charlaix, Phys. Rev. Lett. **100,** 134501 (2008).
[230] Z. Lin and S. Granick, Langmuir **19,** 7061 (2003).
[231] O. I. Vinogradova, H.-J. Butt, G. E. Yakubov, and F. Feuillebois, Rev. Sci. Instrum. **72,** 2330-2338 (2001).
[232] J. B. Brzoska, I. Ben Azouz, and F. Rondelez, Langmuir **10,** 4367-4373 (1994).
[233] C. L. Yaws, *Handbook of Viscosity*, Vol. I.-III. (Houston, Gulf Publishing Company, 1995).
[234] T. M. Galea and P. Attard, Langmuir **20,** 3477 (2004).
[235] A ~ 2 nm zero of separation rror changes the magniude of b by ~ 1 nm (see Eq. (3)).
[236] L. Bocquet and J.-L. Barrat, Soft Matter **3,** 685 (2007).
[237] R. Fetzer, M. Rauscher, A. Münch, B. A. Wagner, and K. Jacobs, Eur. Phys. Lett. **75,** 638-644 (2006).
[238] W. W. Graessley, *Polymeric liquids and networks: dynamics and rheology* (Garland Science, London, 2008).
[239] C. D. F. Honig and W. A. Ducker, J. Phys. Chem. C **112,** 17324-17330 (2008).
[240] P. G. de Gennes, Rev. Mod. Phys. **57,** 827 (1985).
[241] X. Xiao, J. Hu, D. H. Charych, and M. Salmeron, Langmuir **12,** 235 (1996).
[242] M. Voué, R. Rioboo, M. H. Adao, J. Conti, A. I. Bondar, D. A. Ivanov, T. D. Blake, and J. De Coninck, Langmuir **23,** 4695 (2007).
[243] D. Long, A. Ajdari, and L. Leibler, Langmuir **12,** 1675 (1996).

[244] D. Long, A. Ajdari, and L. Leibler, Langmuir **12,** 5221 (1996).
[245] W. A. Ducker, T. J. Senden, and R. M. Pashley, Langmuir **8,** 1831-1836 (1992).
[246] H.-J. Butt, Biophys. J. **60,** 1438-1444 (1991).
[247] E. Spruijt, M. A. Cohen Stuart, and J. van der Gucht, Macromolecules **43,** 1543-1550 (2010).
[248] K. Kurihara, in *Nanohybridization of Organic-Inorganic Materials*; *Vol. 13*, edited by A. Muramatsu and T. Miyashita (Springer, Berlin Heidelberg, 2009), p. 125-137.
[249] U. Mohideen and A. Roy, Phys. Rev. Lett. **81** (1998).
[250] G. L. Klimchitskaya, U. Mohideen, and V. M. Mostepanenko, Rev. Mod. Phys. **81,** 1827-1885 (2009).
[251] M. Kappl and H.-J. Butt, Part. Part. Syst. Charact. **19,** 129-143 (2002).
[252] L.-O. Heim, M. Kappl, and H.-J. Butt, Langmuir **20,** 2760-2764 (2004).
[253] J. L. Hutter, Langmuir **21,** 2630-2632 (2005).
[254] S. Leporatti, R. Sczech, H. Riegler, S. Bruzzano, J. Storsberg, F. Loth, W. Jaeger, A. Laschewsky, S. Eichhorn, and E. Donath, J. Colloid. Interface Sci. **281,** 101-111 (2005).
[255] E. Bonaccurso, M. Kappl, and H.-J. Butt, Phys. Rev. Lett. **88,** 076103 (2002).
[256] O. I. Vinogradova and G. E. Yakubov, Langmuir **19,** 1227-1234 (2003).
[257] O. I. Vinogradova and G. E. Yakubov, Phys. Rev. E **73,** 045302 (2006).
[258] C. D. F. Honig and W. A. Ducker, J. Phys. Chem. C **111,** 16300-16312 (2007).
[259] T. S. Rodriques, H.-J. Butt, and E. Bonaccurso, Colloids Surf. A: Physicochem. Eng. Aspects **354,** 72-80 (2010).
[260] H.-J. Butt, M. Jaschke, and W. A. Ducker, Bioelectrochem. Bioenerg. **38,** 191-201 (1995).
[261] B. Cappella and G. Dietler, Surf. Sci. Reports **34,** 1-104 (1999).
[262] H.-J. Butt, B. Cappella, and M. Kappl, Surf. Sci. Reports **59,** 1-152 (2005).
[263] T. R. Albrecht, S. Akamine, T. E. Carver, and C. F. Quate, J. Vac. Sci. Technol. A **8,** 3386-3396 (1990).
[264] D. Sarid and V. Elings, J. Vac. Sci. Technol. B **9,** 431-436 (1991).
[265] H.-J. Butt, P. Siedle, K. Sefert, K. Fendler, T. Seeger, E. Bamberg, L. Weisenhorn, K. Goldie, and A. Engel, J. Microscopy **169,** 75-84 (1993).
[266] R. Lévy and M. Maaloum, Nanotechnology **13,** 33-37 (2002).
[267] S. M. Cook, T. E. Schäffer, K. M. Chynoweth, M. Wigton, R. W. Simmonds, and K. M. Lang, Nanotechnology **17,** 2135-2145 (2006).
[268] P. Attard, A. Carambassis, and M. W. Rutland, Langmuir **15,** 553-563 (1999).
[269] N. A. Burnham, X. Chen, C. S. Hodges, G. A. Matei, E. J. Thoreson, C. J. Roberts, M. C. Davies, and S. J. B. Tendler, Nanotechnology **14,** 1-6 (2003).
[270] T. J. Senden and W. A. Ducker, Langmuir **10,** 1003-1004 (1994).
[271] M. B. Viani, T. E. Schäffer, A. Chand, M. Rief, H. E. Gaub, and P. K. Hansma, J. Appl. Phys. **86,** 2258-2262 (1999).
[272] D. A. Walters, J. P. Cleveland, N. H. Thomson, and P. K. Hansma, Rev. Sci. Instrum. **67,** 3583-3590 (1996).
[273] H.-J. Butt and M. Jaschke, Nanotechnology **6,** 1-7 (1995).
[274] R. Proksch, T. E. Scäffer, J. P. Cleveland, R. C. Callahan, and M. B. Viani, Nanotechnology **15,** 1344-1350 (2004).
[275] T. E. Schäffer, Nanotechnology **16,** 664-670 (2005).

[276] Colloidal probes were glued to pre-December-2008 NP-S series AFM cantilevers that were distributed by Veeco. These probes originally had a Pyrex base to which the silicon nitride cantilevers were bonded to. Unfortunately, the manufacturing process has changed and it is no longer possible to glue colloidal probes to the more recent NP-S cantilevers produced by Veeco Probes. The newer cantilevers bend during the glue curing process.


[277] M. Preuss and H.-J. Butt, J. Colloid Interface Sci. **208,** 468-477 (1998).

[278] C. Neto and V. S. J. Craig, Langmuir **17,** 2097-2099 (2001).

[279] B. Semin, S. Guriyanova, and E. Bonaccurso, Rev. Sci. Instrum. **77,** 116107 (2006).

[280] K. Visin, Mechanical Design and Test Engineer for Asylum Research. Information exchanged with Sean P. McBride via email on May 10, 2010: Every MFP 3D AFM is currently checked by the test department to have less than a 0.5% non-linearity throughout the full range of the PSD. In most cases less than 0.2% throughout the full PSD range is achieved.

[281] J. E. Sader, Rev. Sci. Instrum. **74,** 2438-2443 (2003).

[282] The zero frequency amplitude, or amplitude at DC, is equivalent to the Thermal DC value in the Asylum Research Software.

[283] M. J. Higgins, R. Proksch, J. E. Sader, M. Polick, S. McEndoo, J. P. Cleveland, and S. P. Jarvis, Rev. Sci. Instrum. **77,** 013701 (2006).

[284] R. W. Stark, T. Drobek, and W. M. Heckl, Ultramicroscopy **86,** 207-215 (2001).

[285] P. Fontaine, P. Guenoun, and J. Daillant, Rev. Sci. Instrum. **68,** 4145-4151 (1997).

[286] Cantilever tilt 11 degrees, colloidal probe angle 5.5 degrees, H = 56 microns, cantilever leg width d = 31 microns, V cross-section b = 122 microns, length L = 114 microns, colloidal probe attachment point relative to cantilever tip 16 microns, and silicon nitride Poisson's ratio 0.24.

[287] T. Young, Philos. Trans. Soc. London **95,** 65 (1805).

[288] V. G. Babak, Rev. Chem. Eng. **15,** 157-221 (1999).

[289] B. P. Binks, Curr. Opin. Colloid Interface Sci. **7,** 21-41 (2002).

[290] C. Johans, P. Liljeroth, and K. Kontturi, Phys. Chem. Chem. Phys. **4,** 1067-1071 (2002).

[291] Y. Lin, H. Skaff, T. Emrick, A. D. Dinsmore, and T. P. Russell, Science **299,** 226-229 (2003).

[292] R. Aveyard, B. P. Binks, and J. H. Clint, Adv. Colloid Interface Sci. **100-102,** 503-546 (2003).

[293] W. H. Binder, Angew. Chem. Int. Ed. **44,** 5172-5175 (2005).

[294] G. Kaptay, Coll. Surf. A **282-283,** 387-401 (2006).

[295] S. P. Moulik and A. K. Rakshit, J. Surface Sci. Technol. **22,** 159-186 (2006).

[296] A. Böker, J. He, T. Emrick, and T. P. Russell, Soft Matter **3,** 1231-1248 (2007).

[297] A. Studart, U. T. Gonzenbach, I. Akartuna, E. Tervoort, and L. J. Gauckler, J. Mater. Chem. **17,** 3283-3289 (2007).

[298] B. L. V. Prasad, C. M. Sorensen, and K. J. Klabunde, Chem. Soc. Rev. **37,** 1871-1883 (2008).

[299] F. Ravera, M. Ferrari, L. Liggieri, G. Loglio, E. Santini, and A. Zanobini, Coll. Surf. A. **323,** 99-108 (2008).

[300] T. N. Hunter, R. J. Pugh, G. V. Franks, and G. J. Jameson, Adv. Colloid Interface Sci. **137,** 57-81 (2008).

[301] A. E. Nel, L. Mädler, D. Velegol, T. Xia, E. M. V. Hoek, P. Somasundaran, F. Klaessig, V. Castranova, and M. Thompson, Nat. Mater. **8,** 543-557 (2009).

[302] J. Gao, H. Gu, and B. Xu, Acc. Chem. Res. **42,** 1097-1107 (2009).
[303] D. L. Cheung and S. A. F. Bon, Phys. Rev. Lett. **102,** 066103 (2009).
[304] R. Krishnaswamy and A. K. Sood, J. Mater. Chem. **20,** 3539-3552 (2010).
[305] R. McGorty, J. Fung, D. Kaz, and V. N. Manoharan, Mat. Today **13,** 34-42 (2010).
[306] M. Grzelczak, J. Vermant, E. M. Furst, and L. M. Liz-Marzán, ACS Nano **4,** 3591-3605 (2010).
[307] P. Singh, D. D. Joseph, and N. Aubry, Soft Matter **6,** 4310-4325 (2010).
[308] W. Ramsden, Proc. R. Soc. London, Ser. A. **72,** 156-164 (1903).
[309] S. U. Pickering, J. Chem. Soc., Trans. **91,** 2001-2021 (1907).
[310] B. P. Binks and C. P. Whitby, Coll. Surf. A. **253,** 105-115 (2005).
[311] K. J. Wilkinson and J. R. Lead, *Environmental Colloids and Particles*, Vol. 10 (John Wiley and Sons Ltd., The Atrium, Southern Gate, Chicheser, West Susses, England, 2007).
[312] B. P. Binks and S. O. Lumsdon, Langmuir **16,** 2539-2547 (2000).
[313] V. B. Menon, R. Nagarajan, and D. T. Wasan, Sep. Sci. and Tech. **22,** 2295-2322 (1987).
[314] S. Crossley, J. Faria, M. Shen, and D. E. Resasco, Science **327,** 68-72 (2010).
[315] S. K. Bindal, A. D. Nikolov, and D. T. Wasan, Environ. Sci. Technol. **35,** 3941-3947 (2001).
[316] K. S. Iyer, B. Zdyrko, S. Malynych, G. Chumanov, and I. Luzinov, Soft Matter **7,** 2538-2542 (2011).
[317] M. A. Cohen Stuart, W. T. S. Huck, J. Genzer, M. Müller, C. Ober, M. Stamm, G. B. Sukhorukov, S. Igal, V. V. Tsukruk, M. Urban, F. Winnin, S. Zauscher, I. Luzinov, and S. Minko, Nat. Mater. **9,** 101-113 (2010).
[318] M. Geiser, V. Im Hof, P. Gehr, and S. Schürch; *Vol. 143*, edited by C. Lenfant, P. Gehr, and J. Heyder (Marcel Dekker, Inc., New York, 2000).
[319] T. J. Russell, Y. Lin, A. Böker, L. Su, P. Carl, H. Zettl, J. He, K. Sill, R. Tangirala, T. Emrick, K. Littrell, P. Thiyagarajan, D. Cookson, A. Fery, Q. Wang, and T. P. Russell, Angew. Chem. Int. Ed. **44,** 2420-2426 (2005).
[320] M. Geiser, B. Rothen-Ruthishauser, N. Kapp, S. Schürch, W. Kreyling, H. Schulz, M. Semmler, V. Im Hof, J. Heyder, and P. Gehr, Environ. Health Perspect. **113,** 1555-1560 (2005).
[321] H. C. Fischer and W. C. W. Chan, Curr. Opin. Biotechnol. **18,** 565-571 (2007).
[322] A. El-Ansary and S. Al-Daihan, J. Toxicology **DOI:10.1155/2009/754810,** 1-9 (2009).
[323] I. W. Wark, J. Phys. Chem. **37,** 623-644 (1933).
[324] H. J. Schulze, Int. J. Miner. Process. **4,** 241-259 (1977).
[325] J. Leja, *Surface Chemistry of Froth Flotation* (Plenum Press, New York, 1982).
[326] H. J. Schulze, *Physico-chemical Elementary Processes in Flotation*, Vol. 4 (VEB Deutscher Verlag der Wissenschaften, Berlin, 1983).
[327] J. Ralston, D. Fornasiero, and R. Hayes, Int. J. Miner. Process. **56,** 133-164 (1999).
[328] A. J. García-Sáez, S. Chiantia, and P. Schwille, J. Bio. Chem. **282,** 33537-33544 (2007).
[329] R. Aveyard and J. H. Clint, J. Chem. Soc., Faraday Trans. **91,** 175-176 (1995).
[330] R. Aveyard and J. H. Clint, J. Chem. Soc., Faraday Trans. **92,** 85-89 (1996).
[331] I. Kasatkin, B. Kniep, and T. Ressler, Phys. Chem. Chem. Phys. **9,** 878-883 (2007).
[332] S. Sivaramakrishnan, J. Wen, M. E. Scarpelli, B. J. Pierce, and J.-M. Zuo, Phys. Rev. B **82,** 195421 (2010).

[333] L. N. Arnaudov, O. J. Cayre, M. A. Cohen Stuart, S. D. Stoyanov, and V. N. Paunov, Phys. Chem. Chem. Phys. **12,** 328-331 (2010).
[334] A. Maestro, L. J. Bonales, H. Ritcco, R. G. Rubio, and F. Ortega, Phys. Chem. Chem. Phys. **12,** 14115-14120 (2010).
[335] G. Gillies, M. Kappl, and H.-J. Butt, Langmuir **21,** 5882-5886 (2005).
[336] G. E. Yakubov, O. I. Vinogradova, and H.-J. Butt, J. Adhesion Sci. Technol. **14,** 1783-1799 (2000).
[337] J. Drelich, Coll. Surf. A **116,** 43-54 (1996).
[338] H. Vinke, G. Bierman, P. J. Hamersma, and J. M. H. Fortuin, Chem. Eng. Sci. **46,** 2497-2506 (1991).
[339] F. Bresme and N. Quirke, Phys. Rev. Lett. **80,** 3791-3794 (1998).
[340] F. Bresme and N. Quirke, J. Chem. Phys. **110,** 3536-3547 (1999).
[341] F. Bresme and N. Quirke, Phys. Chem. Chem. Phys. **1,** 2149-2155 (1999).
[342] C. Powell, N. Fenwick, F. Bresme, and N. Quirke, Coll. Surf. A **206,** 241-251 (2002).
[343] C. Duan and A. Majumdar, Nat. Nanotechnol. Lett. **5,** 848-852 (2010).
[344] J. Drelich, Coll. Surf. A **116,** 43 - 54 (1996).
[345] M. R. Spiegel, *Mathematical Handbook* (McGraw-Hill, New York, 1968).
[346] P.-G. De Gennes, F. Brochard-Wyart, and D. Quere, *Capillarity and wetting phenomena* (Springer-Verlag, New York, 2004).
[347] W. Stöber, A. Fink, and E. Bohn, J. Colloid Interface Sci. **26,** 62-69 (1968).
[348] B. N. Khlebstov, V. Khanadeev, and N. Khlebstov, Langmuir **24,** 8964-8970 (2008).
[349] All sonications/cetrifugation steps during cleaning/decanting were carried out for 10 minutes.
[350] J. M. Andreas, E. A. Hauser, and W. B. Tucker, J. Phys. Chem. **42,** 1001 (1938).
[351] R. A. Orwoll, in *Physical Properties of Polymers handbook, Part III*, 2nd ed., edited by J. E. Mark (Springer Science and Business Media, LLC., New York, 2007).
[352] P. Zoller and H. H. Hoehn, J. Poly. Sci., Polym. Sci. Ed. **20,** 1385 (1982).
[353] The change in air density is insignificant compared to the change in density of the PS as a function of temperature.
[354] A. Bansal, H. Yang, C. Li, K. C. Cho, B. C. Benicewicz, S. K. Kumar, and L. S. Schadler, Nat. Mater. **4** (2005).
[355] G. Tsagaropoulos and A. Eisenberg, Macromol. **28,** 6067-6077 (1995).
[356] G. R. Sanderson, in *Food Gels*, edited by P. Harris (Elsevier, New York, 1990).
[357] O. J. Cayre and V. N. Paunov, Langmuir **20,** 9594-9599 (2004).
[358] B. P. Frank and G. Belfort, Langmuir **17,** 1905-1912 (2001).
[359] H. Helmholtz and G. Pictowsky, Sitzungsber. Kais. Akad. Wiss. Wein, Math-Naturwiss. Kl., Abt. 2 **40,** 607 (1868).
[360] E. Schnell, J. Appl. Phys. **27** (1956).
[361] D. M. Tolstoi, Dokl. Acad. Nauk SSSR **85,** 1329 (1952).
[362] A. N. Somov, Kolloidn. Zh. **44,** 160 (1982).
[363] N. V. Churaev, V. D. Sobolev, and A. N. Somov, J. Colloid Interface Sci. **97,** 574 (1984).
[364] F. Brochard and P. G. De Gennes, Langmuir **8,** 3033 (1992).
[365] P. G. De Gennes, C. R. Acad. Sci. **288B,** 219 (1979).
[366] G. K. Batchelor, *An Introduction to Fluid Dynamics* (Cambridge University Press, The Edinburgh Building, Cambridge CB2 2RU, UK, 1967).

[367] J. Happel and H. Brenner, *Low Reynolds Number Hydrodynamics* (Prentice-Hall, Inc., Englewood Cliffs, N.J., 1965).
[368] *Igor Pro Version 5.0 Programming Manuals, Vol. I-III* (Wavemetrics, Inc. Lake Oswego, OR, 97035, USA, 2003).